ISSN 1811-1165 (Print)
ISSN 2413-2179 (Online)

EURASIAN PHYSICAL TECHNICAL JOURNAL

VOLUME 20, NO. 3(45), 2023

phtj.buketov.edu.kz

EURASIAN PHYSICAL TECHNICAL JOURNAL

p - ISSN 1811-1165
e - ISSN 2413-2179

Volume 20, No. 3(45), 2023

1st issue – March, 2004

Journal Founder:

E.A. BUKETOV KARAGANDA UNIVERSITY

Е.А.БӨКЕТОВ АТЫНДАҒЫ ҚАРАҒАНДЫ УНИВЕРСИТЕТІ

КАРАГАНДИНСКИЙ УНИВЕРСИТЕТ имени Е.А.БУКЕТОВА

https://phtj.buketov.edu.kz

Contact information:
Editorial board of EAPhTJ (Build. 2, room 216)
E.A. Buketov Karaganda University
Universitetskaya Str.28, Karaganda,
Kazakhstan, 100024
Subscription index: 75240

Tel: +7(7212) 77-04-03
Fax: +7(7212) 35-63-98
E-mail: ephtj@mail.ru

Signed to print on 21.09.2023
Format 60x84 1/8. Offset paper.
Volume 12.25 p.sh. Circulation 300 copies.
Agreed price. Order No. 95.

Басуға 21.09.2023 ж. қол қойылды.
Пішімі 60×84 1/8. Офсеттік қағазы.
Көлемі 12,25 ес.-б.т. Таралымы 300 дана.
Бағасы келісім бойынша. Тапсырыс № 95.

Подписано к печати 21.09.2023 г.
Формат 60×84 1/8. Офсетная бумага.
Объем 12,25 печ.л. Тираж 300 экз.
Цена договорная. Заказ № 95.

Printed in the Publishing House
of the E.A.Buketov KarU

Е.А. Бөкетов атындағы ҚарУ баспасының
баспаханасында басылып шықты

Отпечатано в Издательстве
КарУ имени Е.А.Букетова

Registration Certificate No.4382-Zh, November 7, 2003.
Re-registration Certificate No.KZ50VPY00027647, October 6, 2020 issued by Information Committee of the Ministry of Information and Public Development of the Republic of Kazakhstan

Eurasian Physical Technical Journal, 2023, Vol. 20, No. 3(45)

CONTENTS

Dear authors and readers!

Dear colleagues!

Traditionally, we inform our authors and readers about the most important results. In July 2023, an expert assessment was carried out by a special commission, the results of which established that the “Eurasian phys. tech. j." is included in the updated List of publications recommended by the Committee for Quality Assurance in Science and Higher Education of the Science and Higher Education Ministry of the Kazakhstan Republic for publication of scientific activities main results in the scientific fields: Physics, Energy, Materials Science (Addendum 1, July 25, 2023 to Order No. 52).

In this issue, in the “Materials Science” section, new results on the study of the properties of various materials are presented. For example, in an article of Orenburg scientists, a study was conducted of “a model of the quasi-equilibrium conformational structure of the units of a Gaussian chain of a polyelectrolyte adsorbed on a nanosphere with a relatively low electrical conductivity” (i.e., an undoped semiconductor), polarized in an external harmonically varying quasi-static electric field with a frequency significantly lower plasma frequency of the nanoparticle material. The next article shows that corrosion of aluminum products in seawater occurs due to “incomplete oxidation of aluminum cells on the surface of products due to insufficient energy for chemical interaction with aluminum atoms of the orthorhombic subsystem of the cubic face-centered cell of aluminum.” The work of Astana scientists determined the spectral properties of carbon-containing nanocomposite polymer films based on polystyrene with C60 fullerene nanoadditives. It has been shown that “with an increase in the concentration of the carbon additive, the optical density of the samples increases, the absorption coefficient increases, and the band gap decreases.” Joint studies scientists from of Uzbekistan, Russia, Bulgaria and Vietnam on the processes of defect formation in diffusely doped and proton-irradiated silicon using the impedance spectroscopy method showed that their relatively high resistance to radiation exposure is due to a higher concentration of ion impurities (platinum) in the volume.

The article in the “Energy” section examines the effect of the injection rate of liquid fuel into the combustion chamber. As a result of a numerical experiment using KIVA-II software, the optimal range of heptane injection speed was determined, which ensures increased efficiency of the combustion chamber and reduced negative impact on the environment.

The authors of the articles in the “Engineering” section offer solutions to current problems of modern production and electronic communication systems. For example, in the work of an international team of authors from Egypt, China and the Russian Federation, it was proposed to use the thermoelectric control method to determine the thermophysical parameters of the thermal interface. It is shown that this method allows you to clearly see the heat transfer process with the introduction of thermal resistance, temperature fluctuations and the resulting thermos-EMF. In the work of the Almaty scientists, the viability of prepregs based on epoxy resin with an aromatic hardener, which is of great practical importance in the industrial production of carbon fiber plastic products, was studied. In an article of the E.A.Buketov Karaganda University researches, a microcontroller device has been developed for reproducing audio information in the presence of a person. 17 operational devices for reproducing audio information have been installed and are successfully operating on the territory of the university complex.

The article in the “Physics and Astronomy” section presents the results of an analysis of changes in the fractal, statistical and kinetic parameters of particles. It is shown that a decrease in fractal dimension during heteroannihilation of particles is accompanied by a decrease in asymmetry and an increase in kurtosis, which characterize the shape and degree of symmetry of the distribution of interacting particles.

We hope that the presented research results will be of interest and will be useful for scientists, teachers, researchers, doctoral students and undergraduates. We will be glad to see you among our readers and authors of the next issues, where it is planned to publish custom-made review articles by leading scientists on topical and priority areas of modern physics and technology.

Exactly 20 years have passed since the day when, in accordance with the decision of the Academic Council of E.A. Buketov Karaganda University, the Rector's Order No. 165 of September 15, 2003 was signed on the founding of the scientific journal "Eurasian Physical Technical Journal". The first journal issue in English was prepared in 2004. Until now, it is published as a peer-reviewed international scientific journal of open access, publishing original research results on topical problems of technical physics.

To work on the editorial board, the first chief editor, doctor of technical sciences, academics, professor Akylbaev Zh.S. invited leading scientists in the field of technical physics from Kazakhstan scientific centers, as well as Russia, Uzbekistan, Kyrgyzstan, etc. Unfortunately, some of them, like the first editor-in-chief of the journal, have died suddenly, but their contribution to the formation and development of the journal has been is very valuable and important until now. We try write about important biographical facts and anniversaries of wonderful scientists - our respected editors in issues of the Eurasian Physical Technical Journal, will certainly continue this tradition in the future.

In this issue we welcome Corresponding Member of the Russian Academy of Sciences, Doctor of Physical and Mathematical Sciences, Professor of the Institute of Thermophysics named after S.S. Kutateladze SB RAS Nikolai Alekseevich Pribaturin, who has been working on the editorial board since its founding.

It is impossible to list all the scientific achievements of the hero of the day, let note the highlights of his biography and the most important scientific achievements.

Professor Nikolai Alekseevich Pribaturin is widely known as a highly qualified specialist in the field of thermophysical modeling of coolant dynamics in nuclear reactor plants. Since 2007, professor Pribaturin N.A. is the director of the Novosibirsk branch of the Institute of Nuclear Safety of the Russian Academy of Sciences (IBRAE RAS). With his direct participation, priority data on local hydrodynamics and heat transfer of coolants in modern reactor plants, including promising reactor plants with lead and water coolants, were obtained. The results obtained became the basis for design decisions that help reduce the risks of emergency events and contribute to filling the verification matrices of calculation codes. Comprehensive research has been carried out to develop the safety of nuclear reactors and design advanced energy complexes with heavy liquid metal coolant. For the first time in the world, with the participation of Professor Pribaturin N.A. detailed data were obtained establishing the efficiency of coolant mixing in the channels of reactor plants, on the interphase interaction of two-phase flows, determining the conditions and ways to improve the designs of fuel assemblies.

Professor Pribaturin N.A. constantly carries out work on training scientific and technical personnel on thermophysical problems of modern nuclear power plants, supervises the work of graduate students. He is a member of the Academic Council and Dissertation Council of the Institute of Thermophysics named after. S.S. Kutateladze SB RAS and the Institute for the Safe Development of Nuclear Energy of the Russian Academy of Sciences, the National Committee on Heat Transfer, the Russian Acoustic Society, member of the organizing committees of international conferences and editorial boards of journals. Despite his high position as a leader and the authority of a scientist, in life Nikolai Alekseevich is an open, simple and modest person and a reliable comrade. We are proud to cooperate with you. You can always advise us on many issues and give valuable recommendations.

Dear Nikolai Alekseevich, please accept heartfelt congratulations on your 70th anniversary and best wishes from the editorial board, authors and readers of the Eurasian Physical Technical Journal and from all Kazakhstani colleagues. We wish you Siberian health, inexhaustible perseverance and creative success in achieving your goals, happiness and prosperity to you and your family and friends!

We hope that cooperation with you will continue in the future, and we will see you, your colleagues and students among the article's authors of future issues.

With wishes of health and prosperity to all our authors, editors and readers,
Editor-in-chief,
Professor Sakipova S.E.
September, 2023

DOI 10.31489/2023No3/5-19

UDC 539.199, 544.723.2

CONFORMATIONAL STRUCTURE OF AN ADSORBED POLYELECTROLYTE ON A NANOPARTICLE WITH LOW CONDUCTIVITY IN AN ALTERNATING ELECTRIC FIELD

Kucherenko M.G., Kruchinin N.Yu.*

Center of Laser and Informational Biophysics, Orenburg State University, Orenburg, Russian Federation, kruchinin_56@mail.ru

An analytical form of the model of the quasi-equilibrium conformational structure of the units of the Gaussian chain of a polyelectrolyte adsorbed on a nanospheroid with a relatively low electrical conductivity (undoped semiconductor) polarized in an external harmonically varying quasi-static electric field with a frequency significantly lower than the plasma frequency of the nanoparticle material is proposed. Variants of the model are discussed that go beyond the scope of the quasi-static approximation, i.e., take into account the effects of delay, the manifestation of which will be noticeable in the case of sufficiently extended nanostructures. Electrically induced conformational changes of generally neutral polyampholytic polypeptides on the surface of a spherical germanium nanoparticle in a static or alternating external electric field have been studied by molecular dynamics. In a static electric field, in the case of a small distance between the charged units in the polyampholyte, a large number of macrochain loops were formed, elongated in the direction of the polarization axis of the nanoparticle. If the distance between the oppositely charged amino acid residues of the polypeptide exceeded the diameter of the nanoparticle, the charged units were mainly localized in the oppositely charged subpolar regions of the polarized germanium nanoparticle. In an alternating electric field, a girdle polyampholyte edge was formed in the equatorial region of the nanoparticle, the macrochain links of which were desorbed from the surface with an increase in the amplitude of the polarizing alternating electric field.

Keywords: semiconductor nanoparticle, macromolecule, conjugates, conformations, molecular dynamics.

1. Introduction

Conjugates of quantum dots with macromolecular chains are widely used as biological nanoprobes, as well as in the elements of various chemical sensors based on the use of the Förster energy transfer between nanoobjects connected by a macrochain [1–9]. In this aspect, of great interest is the control of the characteristics of such functional nanosystems by the action of an external electric field [10–13]. To this end, both generally neutral polyampholytic macromolecules and charged polyelectrolyte macrochains can be located on the surface of a nanoobject, the conformational structure of which can change under the influence of electric charges distributed over the surface of the nanoparticle.

Previously, in [14–21], conformational changes in polyampholytic polypeptides adsorbed on the surface of gold nanoparticles of various shapes (spherical, cylindrical, and spheroidal) were studied under the influence of both a static and an alternating microwave electric field. It was shown that the shape of a metal nanoobject significantly affects the conformations of adsorbed polyampholytes.

The nature of adsorption of macromolecules on the surface of a nanoobject is also greatly influenced by its chemical composition and structure, which is especially important when considering quantum dots of various chemical compositions. In addition, when semiconductor quantum dots are placed in an external electric field, the values of the surface density of induced charges will be lower than for metal nanoparticles [22]. This is especially important when considering complexes consisting of semiconductor and metal nanoparticles with polyelectrolyte macromolecules adsorbed on them.

It was previously noted in [21] that the frequency dependence of the dipole polarizability of metal nanoparticles located in a microwave (in the traditional technical classification, but at the same time, low-frequency compared to the infrared frequency range) electric field practically does not manifest itself. However, it becomes noticeable in the case of nanoparticles made from materials with a sufficiently low specific conductivity, for example, from pure or lightly doped semiconductors such as germanium.

.

Therefore, the purpose of this work is a more detailed study of changes in the conformations of polyampholytic macromolecules adsorbed on the surface of semiconductor spheroidal nanoparticles in an alternating microwave electric field. As well as the generalization of the mathematical model of the formation of a quasi-equilibrium macrochain layer [21] to the case of the dispersion dependence of the permittivity of the material of a conducting nanoparticle of a more general form, including the presence of a real part. In particular, the construction of a new version of the theoretical model with going beyond the quasi-static approximation, that is, taking into account the effects of delay, the manifestation of which will be the more noticeable, the more extended the considered structures are on the scale of electromagnetic wavelengths.

2. General mathematical model of the macrochain layer of a nanospheroid in an external low-frequency field

2.1 Formation of a quasi-equilibrium conformational structure of polyelectrolyte chain links adsorbed on a nanospheroid with low electrical conductivity polarized in an external harmonically variable electric field at a frequency significantly lower than the plasma frequency of the material (undoped semiconductor) of the nanoparticle.

A polyelectrolyte macrochain adsorbed on the surface of a spheroidal nanoparticle in the simplest approximation can be considered as an ideal Gaussian chain [19] interacting with an electrically neutral adsorbent particle through van der Waals forces, and in the case of a charged or polarized nanoparticle, Coulomb forces, or forces of the "charge- dipole" [19].

The conformational function $\psi(\mathbf{r})$, which depends on the radius vector **r** of a chain link and takes into account the entropy factor for the formation of the bulk structure of a macromolecule, can be calculated on the basis of a specialized differential equation [23], which was previously done in the case of a short-range adsorbing potential [17, 19]. When applying an external, harmonically changing electric field $E_0 \exp(-i\omega t)$, at a sufficiently small value of the frequency ω, it is possible to use the quasi-stationary approximation. It is obvious that the frequency ω, in this case, should be less than the frequency of the characteristic rose mode of the macrochain. Under such conditions, it is reasonable to consider quasi-equilibrium conformations of a polymer molecule adsorbed on a nanoparticle in an external field. In a simple approach, taking into account the interaction of macrochain links with the field of a charged and polarized nanoparticle reduces to introducing the Boltzmann factor *W* [19, 21].

When a spheroidal nanoparticle is placed in a quasi-stationary uniform electric field of strength $\mathbf{E}_0$, an additional field of a polarized particle arises. To describe the field of charged and/or polarized ellipsoids of revolution (half axes $a = b \neq c$), spheroidal coordinates $\xi = (r_1 + r_2)^2 / 4 - a^2$, $\eta = (r_1 - r_2)^2 / 4 - a^2$, φ [22] are usually used. If the vector $\mathbf{E}_0$ is oriented along the c-axis of the spheroid, the potential $\Phi(\xi, \eta)$ of the external field $\mathbf{E}_0\mathbf{r}$, together with the potentials $\varphi_Q(\xi)$ and $\varphi_P(\xi, \eta)$ fields of the charged and polarized spheroid, can be written as [21]

$$\Phi(\xi, \eta) = -\mathbf{E}_0\mathbf{r} + \varphi_Q(\xi) + \varphi_P(\xi, \eta). \quad (1)$$

With a harmonic change in the quasi-stationary field with a frequency ω, the semiconductor material of the nanoparticle is characterized by a complex-valued permittivity $\varepsilon(\omega)$. The potential $\varphi^{(e)}(\xi, \eta) = -\mathbf{E}_0\mathbf{r} + \varphi_P(\xi, \eta)$ of the resulting field in space outside a conducting uncharged spheroid polarized in an alternating external uniform field parallel to its symmetry axis *z* can be written in the following form (without the phase factor $\exp(-i\omega t)$) [21]

$$\varphi^{(e)}(\xi,\eta)=\varphi_0(\xi,\eta)\left\{1-\frac{[\varepsilon(\omega)-\varepsilon^{(e)}]a^2c}{\left\{\varepsilon^{(e)}+[\varepsilon(\omega)-\varepsilon^{(e)}]n^{(z)}\right\}}\int_{\xi}^{\infty}\frac{d\xi'}{\left(\xi'+c^2\right)^{3/2}\left(\xi'+a^2\right)}\right\}. \quad (2)$$

$$n^{(z)}=\frac{1+e^2}{e^3}\left(e-\operatorname{arctg} e\right),\quad \varphi_0(\xi,\eta)=-E_0z=-E_0\left[\frac{(\xi+c^2)(\eta+c^2)}{c^2-a^2}\right]^{1/2}. \quad (3)$$

The constant $\varepsilon^{(e)}$ in (2) is the permittivity of the solvent.

Far from the surface of an uncharged spheroid, the potential of the resulting field includes the characteristic field of an induced electric dipole with polarizability $\alpha^{(j)}(\omega)$

$$\varphi^{(e)}(\mathbf{r})=-\mathbf{E}_0\mathbf{r}+\alpha^{(j)}(\omega)\mathbf{E}_0\mathbf{r}/r^3. \quad (4)$$

The dipole dynamic polarizability $\alpha^{(j)}(\omega)$ of a spheroid is a tensor of the second rank, which in the system of its principal axes takes the form

$$\alpha^{(j)}(\omega)=\frac{a^2c}{3}\frac{\varepsilon(\omega)-\varepsilon^{(e)}}{\varepsilon^{(e)}+\left[\varepsilon(\omega)-\varepsilon^{(e)}\right]n^{(j)}},\quad j=x,y,z. \quad (5)$$

Here, in (5) $n^{(j)}$ are the depolarization coefficients of the spheroid, and $n^{(x)}=n^{(y)}=\frac{1}{2}\left[1-n^{(z)}\right]$. The frequency dependence of the permittivity $\varepsilon(\omega)$ of the semiconductor material of the nanoparticle is represented by the generalized Drude-Lorenz model [24]

$$\varepsilon(\omega)=\varepsilon_\infty-\frac{\omega_p^2}{\omega^2+i\omega\gamma}, \quad (6)$$

where ω_p, γ - plasma frequency and frequency of collisions of conduction electrons, respectively; ε_∞ - constant high-frequency part of the permittivity, introduced in connection with the need to take into account interband transitions in a semiconductor. As noted in [21], at frequencies ω_p much lower than the plasma frequency, the polarizability factor

$$\frac{[\varepsilon(\omega)-\varepsilon^{(e)}]a^2c}{\left\{\varepsilon^{(e)}+[\varepsilon(\omega)-\varepsilon^{(e)}]n^{(z)}\right\}}$$

standing in front of the integral on the right side of (2), weakly depends on the frequency. For a more detailed analysis of this dependence in the region of "conformational resonance" of the macrochain, i.e., for frequencies of the order of 10^9-10^{10} Hz, we use the formula for the limiting transition from the permittivity (6) to an expression containing the specific conductivity σ = const of the semiconductor ε = const without taking into account its frequency dispersion [22]

$$\underset{\omega<<\omega_p}{\varepsilon(\omega)\to}\varepsilon+i\frac{4\pi\sigma}{\omega}. \quad (8)$$

Note that this expression follows from the Maxwell equation in the absence of dispersion (σ = const, ε = const)

$$\operatorname{rot}\mathbf{H}=\frac{4\pi\sigma}{c}\mathbf{E}+\frac{\varepsilon}{c}\frac{\partial}{\partial t}\mathbf{E}, \quad (9)$$

with a harmonic change in the electric and magnetic fields

$$\mathbf{E}(t)=\mathbf{E}_0\exp(-i\omega t),\quad \mathbf{H}(t)=\mathbf{H}_0\exp(-i\omega t).$$

Then, taking into account (8), and if the frequencies are such that $\omega<<\gamma$, we obtain for the conductivity

.

$$\sigma = \frac{\omega_p^2}{4\pi\gamma}. \tag{10}$$

2.2 Spherical nanoparticle

The depolarization coefficients of a spherical nanoparticle $n^{(j)} = 1/3$ are the same for all three values of *j*, and then for the dipole dynamic electric polarizability $\alpha_S(\omega)$ of a conducting spherical particle of radius *R* for subplasma frequencies $\omega << \omega_p$ we obtain

$$\alpha_S(\omega) = \frac{\varepsilon(\omega) - \varepsilon^{(e)}}{\varepsilon(\omega) + 2\varepsilon^{(e)}} R^3 \to \frac{i4\pi\sigma - \omega\left(\varepsilon^{(e)} - \varepsilon\right)}{i4\pi\sigma + \omega\left(2\varepsilon^{(e)} + \varepsilon\right)} R^3. \tag{11}$$

In this case, the real and imaginary parts of the dipole polarizability can be written as

$$\alpha'_S(\omega) = \frac{(4\pi\sigma)^2 - \omega^2(\varepsilon^{(e)} - \varepsilon)(2\varepsilon^{(e)} + \varepsilon)}{(4\pi\sigma)^2 + \omega^2(2\varepsilon^{(e)} + \varepsilon)^2} R^3, \tag{12}$$

$$\alpha''_S(\omega) = \frac{12\pi\sigma\omega\,\varepsilon^{(e)}}{(4\pi\sigma)^2 + \omega^2(2\varepsilon^{(e)} + \varepsilon)^2} R^3. \tag{13}$$

It follows from (12) that the sign of the polarization of the nanoparticle switches at the frequency $\omega = \omega_0$, and then for the characteristic switching frequency ω_0 we obtain the expression

$$\omega_0 = \left(4\pi / \sqrt{(\varepsilon^{(e)} - \varepsilon)(2\varepsilon^{(e)} + \varepsilon)}\right)\sigma.$$

In the limit of very low frequencies $\omega \to 0$, from (12) and (13) the following expressions follow:

$$\lim_{\omega\to 0} \alpha'_S(\omega) = \left[1 - \frac{3\varepsilon^{(e)}(2\varepsilon^{(e)} + \varepsilon)}{(4\pi\sigma)^2}\omega^2\right] R^3, \tag{14}$$

$$\lim_{\omega\to 0} \alpha''_S(\omega) = \frac{3\varepsilon^{(e)}\omega}{4\pi\sigma} R^3. \tag{15}$$

It should also be noted that the parameter ε = const is not present at all in formula (15) for the imaginary part of the polarizability; therefore, the result (15) coincides with the corresponding expression obtained in [21] for metal nanoparticles.

From (12) it follows that all possible values $\alpha'_S(\omega)/R^3$ of the real part of the polarizability belong to the interval [-*b*, 1], where the constant b is determined by the expression

$$b = \frac{(\varepsilon^{(e)} - \varepsilon)}{(2\varepsilon^{(e)} + \varepsilon)}. \tag{16}$$

An imaginary part $\alpha''_S(\omega)$ of the polarizability determines not only the dissipation of the energy of the external electromagnetic field in the nanoparticle [21], but also the amplitude of oscillations of the cross part of the induced dipole moment $\alpha''_S(\omega)E_0\exp(-i\omega t + i\pi/2)$. In this case, the oscillations of the corresponding dipole component of the field themselves are shifted in phase by an amount $\pi/2$ relative to the oscillations of the external field $E_0\exp(-i\omega t)$. Oscillations of the real part of the polarizability $\alpha'_S(\omega)E_0\exp(-i\omega t)$ will be in-phase with the external seed field, as well as the oscillations of the secondary in-phase field corresponding to it, that is, the field of the in-phase oscillating induced dipole moment.

Note that expressions (11) and (12-13) can be obtained not only by using the limit transition (8), but also by solving the equations for the field inside and outside the conducting nanoparticle, followed by matching the obtained solutions on the boundary sphere of radius *R*.

2.3 Spheroidal nanoparticle

In the case of a spheroidal nanoparticle, for the components of the diagonalized polarizability tensor $\alpha^{(j)}(\omega)$, from (5) and (8) we obtain

$$\alpha^{(j)}(\omega) = \frac{abc}{3}\frac{i4\pi\sigma - \omega(\varepsilon^{(e)} - \varepsilon)}{\omega\varepsilon^{(e)} + \left[i4\pi\sigma - \omega(\varepsilon^{(e)} - \varepsilon)\right]n^{(j)}}, \quad j = x, y, z\ . \tag{17}$$

For the corresponding (17) real and imaginary parts of the spheroid polarizability tensor $\alpha^{(j)}(\omega)$, we can write

$$\alpha'^{(j)}(\omega) = \frac{abc}{3}\frac{(4\pi\sigma)^2 n^{(j)} - \omega^2(\varepsilon^{(e)} - \varepsilon)\left[\varepsilon^{(e)}(1-n^{(j)}) + \varepsilon n^{(j)}\right]}{\left[4\pi\sigma n^{(j)}\right]^2 + \omega^2\left[\varepsilon^{(e)}(1-n^{(j)}) + \varepsilon n^{(j)}\right]^2}\ . \tag{18}$$

$$\alpha''^{(j)}(\omega) = \frac{abc}{3}\frac{4\pi\sigma\omega\varepsilon^{(e)}}{\left[4\pi\sigma n^{(j)}\right]^2 + \omega^2\left[\varepsilon^{(e)}(1-n^{(j)}) + \varepsilon n^{(j)}\right]^2}\ . \tag{19}$$

Then the real part of the potential (2) of the resulting field outside the nanoparticle

$$\mathrm{Re}\,\varphi^{(e)}(\xi,\eta;t) = \varphi_0(\xi,\eta)\times\cos\omega t$$
$$\times\left\{1 - \frac{(4\pi\sigma)^2 n^{(j)} - \omega^2(\varepsilon^{(e)} - \varepsilon)\left[\varepsilon^{(e)}(1-n^{(j)}) + \varepsilon n^{(j)}\right]}{\left[4\pi\sigma n^{(j)}\right]^2 + \omega^2\left[\varepsilon^{(e)}(1-n^{(j)}) + \varepsilon n^{(j)}\right]^2}a^2c\int_{\xi}^{\infty}\frac{d\xi'}{\left(\xi'+c^2\right)^{3/2}\left(\xi'+a^2\right)}\right\}. \tag{2'}$$

The oscillations of the corresponding dipole component of the field, shifted in phase by an amount $\pi/2$ relative to the oscillations of the external field $E_0\exp(-i\omega t)$, are determined by the imaginary part of the potential (2) and, accordingly, the imaginary part of the polarizability $\alpha''(\omega)$

$$\mathrm{Im}\,\varphi^{(e)}(\xi,\eta;t) = \varphi_0(\xi,\eta)\cdot\sin\omega t\times$$
$$\times\frac{4\pi\sigma\omega\varepsilon^{(e)}a^2c}{\left[4\pi\sigma n^{(j)}\right]^2 + \omega^2\left[\varepsilon^{(e)}(1-n^{(j)}) + \varepsilon n^{(j)}\right]^2}\int_{\xi}^{\infty}\frac{d\xi'}{\left(\xi'+c^2\right)^{3/2}\left(\xi'+a^2\right)}\cdot \tag{2''}$$

For the frequency ω_0 of polarization sign switching in this case, it follows from (18) that

$$\omega_0 = 4\pi\sigma\sqrt{\frac{n^{(j)}}{(\varepsilon^{(e)} - \varepsilon)\left[\varepsilon^{(e)}(1-n^{(j)}) + \varepsilon n^{(j)}\right]}}, \tag{20}$$

whence at $n^{(j)} = 1/3$ follows the previously obtained value of the frequency ω_0 of switching the polarization sign for the ball $\omega_0 = 4\pi\sigma/\sqrt{(\varepsilon^{(e)} - \varepsilon)(2\varepsilon^{(e)} + \varepsilon)}$.

.

The numerical estimates of $\alpha'_S(\omega)/R^3$ and $\alpha'^{(z)}(\omega)/(a^2c)$ in the frequency range of "conformational resonance" carried out in [21], i.e., ~ 10^9-10^{10} Hz, performed at ε=0 for spherical or spheroidal nanoparticles of metals such as Ag or Au ($4\pi\sigma \sim 10^{16} \div 10^{17}$ Hz) showed that the specific polarizabilities are close to 1. The frequency dependences of the polarizabilities $\alpha_S(\omega)$ and $\alpha^{(j)}(\omega)$ pure or lightly doped semiconductors of the Ge type are more noticeable , since their conductivity is $4\pi\sigma \sim 10^9 \div 10^{10}$ Hz, i.e. of the same order as the frequencies ω of the external field.

In the case of an excess charge Q on the spheroid in the outer region outside it, an additional quasi-static field with a potential $\varphi_Q(\xi)$ arises [21, 22], and then the interaction energy of the resulting electric field with a group of polyelectrolyte units bearing a characteristic charge q' takes the form:

$$V_{tot}(\xi,\eta) = q'\varphi_Q(\xi) + q'\varphi^{(e)}(\xi,\eta)\,. \tag{21}$$

Then the probability of detecting a polymer link at a point with coordinates ξ,η above the nanoparticle surface in the equilibrium configuration of polyelectrolyte macrochains at temperature T is determined by the Boltzmann factor $W(\xi,\eta)$ based on the potential (21)

$$W(\xi,\eta) = \exp\left\{-\frac{q'}{kT}\left[\varphi_Q(\xi) + \varphi^{(e)}(\xi,\eta)\right]\right\}. \tag{22}$$

The Boltzmann factor (22) contains all the information about the interaction of a polymer with an electric field. Upon adsorption of a macrochain on an elongated or compressed spheroidal nanoparticle polarized in an external field, the formation of edge layer conformations within the model of unbound units was studied in [21]. In this case, the contribution of the quasi-stationary field (21) to the appearance of equilibrium conformations of the macromolecule is taken into account by means of the Boltzmann factor. The final spatial distribution of the density $n(\xi,\eta)$ of units of a polyelectrolyte macrochain adsorbed by a polarized nanospheroid takes the form

$$n(\xi,\eta) = \psi^2(\xi,\eta)\exp\left[-\frac{V_{tot}(\xi,\eta)}{kT}\right]. \tag{23}$$

Thus, the equilibrium density distribution of chain links (23) contains two factors: entropy $\psi^2(\xi,\eta)$, which contains the memory of the linear structure of the macrochain and details of the surface relief of the adsorbing nanoparticle [21], and Boltzmann $W(\xi,\eta)$. The conformational functions $\psi^2(\xi,\eta)$ for the entropy factor on the surface of an oblate spheroid were calculated earlier.

2.4 Accounting for the delay effect

Consideration of delay effects becomes necessary when the major semiaxis of the prolate spheroid becomes commensurate in magnitude with the wavelength of the alternating field, i.e. the spheroid becomes sufficiently extended. At the same time, going beyond the quasi-stationary approximation to determine the characteristics of an alternating electric field, that is, taking into account the delay effect due to the finiteness of the speed of light, is associated with the need to solve the Helmholtz equation instead of the Laplace equation. Obviously, even for the case of a spherical particle, the analytical solution of the problem is associated with significant difficulties. Such a problem for a ball has already been solved earlier in the theory of diffraction and is known as the Mie solution [24]. A harmonically changing electromagnetic field can be either a standing or traveling wave. Mi's solution is written for the latter.

If a plane linearly polarized electromagnetic wave propagates along the polar z-axis of a spherical coordinate system (SCS) r,θ,ϕ, the electric field is directed along the x-axis, and the magnetic field is directed along the y-axis, then the Cartesian components of the strengths of these fields

$$E_x^0 = H_y^0 = \exp(ikz) = \exp(ikr\cos\theta) = \sum_{n=0}^{\infty}(2n+1)i^n\sqrt{\frac{\pi}{2kr}}J_{n+1/2}(kr)$$

as well as the components in the SSC, written in terms of the *U, U'* Borgnies potentials

$$E_r = \frac{\partial^2 U}{\partial r^2} + k^2 U,\ E_\theta = \frac{1}{r}\frac{\partial^2 U}{\partial r \partial \theta},\ E_\phi = -\frac{i\omega\mu}{\varepsilon r}\frac{\partial U'}{\partial \theta}.$$
$$H_r = \frac{\partial^2 U'}{\partial r^2} + k^2 U',\ H_\theta = \frac{1}{r}\frac{\partial^2 U'}{\partial r \partial \theta},\ H_\phi = \frac{ik^2 c}{\omega\mu r}\frac{\partial U}{\partial \theta}.$$

The boundary conditions on the surface of the ball have the form

$$\left.\begin{aligned} \frac{\partial}{\partial r}(ru_2) = \frac{\partial}{\partial r}(ru_1),\ \frac{k_1^2 u_1}{\mu_1} = \frac{k_2^2 u_2}{\mu_2} \\ \frac{\partial}{\partial r}(rv_2) = \frac{\partial}{\partial r}(rv_1),\ \mu_1 v_1 = \mu_2 v_2 \end{aligned}\right\},\ r = R.$$
$$k_j^2 = \frac{\varepsilon_j \mu_j \omega^2}{c^2} + i\frac{4\pi\sigma_j \mu_j \omega}{c^2}.$$

The functions $u=U/r$, $v=U'/r$ of the Borgnis potentials U,U' are defined by the expressions [25]

$$u = \begin{cases} \sum_{n=0}^{\infty} a_n \left[\psi_n(k_1 r) + \alpha_n \varsigma_n^{(1)}(k_1 r)\right]\left[-\frac{d}{d\theta}P_n(\cos\theta)\right]\cos\phi, & r > R \\ \sum_{n=0}^{\infty} A_n \psi_n(k_2 r)\left[-\frac{d}{d\theta}P_n(\cos\theta)\right]\cos\phi, & r < R \end{cases}$$

Here the constant coefficients

$$a_n = \frac{2n+1}{n(n+1)}\frac{i^{n-1}}{k},\quad \alpha_n = \frac{(k_1^2/\mu_1)\psi_n(k_1R)\Psi_n(k_2R) - (k_2^2/\mu_2)\psi_n(k_2R)\Psi_n(k_1R)}{\Delta},$$
$$A_n = \frac{k_1^2\left[\Psi_n(k_1R)Z_n^{(1)}(k_1R) - \psi_n(k_1R)\varsigma_n^{(1)}(k_1R)\right]}{\mu_1\Delta}$$

are specified on the surface of a spherical nanoparticle, and the functions

$$\Psi_n(x) = \frac{d}{dx}\left[x\cdot\psi_n(x)\right],\ \psi_n(x) = \sqrt{\frac{\pi}{2x}}J_{n+1/2}(x),\quad \varsigma_n^{(1)}(x) = \sqrt{\frac{\pi}{2x}}H_{n+1/2}^{(1)}(x),$$
$$Z_n^{(1)}(x) = \frac{d}{dx}\left[x\cdot\varsigma_n^{(1)}(x)\right],\quad \Delta = \frac{k_2^2}{\mu_2}Z_n^{(1)}(k_1R)\psi_n(k_2R) - \frac{k_1^2}{\mu_1}\Psi_n(k_2R)\varsigma_n^{(1)}(k_1R).$$

are based on the well-known Bessel functions $J_{n+1/2}(x)$ and Hankel functions of the first kind $H_{n+1/2}^{(1)}(x)$ of a half-integer index. The expressions for the coefficients β_n and B_n that define the function $v=U'/r$ have a similar form [25]. The numerical implementation of the model even for spherical nanoparticles is very laborious, but it may become necessary if the field quasi-stationarity condition is violated.

To form a conformation map of the polyelectrolyte chain, information is required on the radial-angular dependences of the components of the electric field vector **E(r)**: $E_r(r,\theta,\phi),\ E_\theta(r,\theta,\phi),\ E_\phi(r,\theta,\phi)$. The azimuthal component of the field $E_\phi(\mathbf{r})$, which was absent in the quasi-stationary approximation and the corresponding axially symmetric field, appears due to the magnetic components $H_j(\mathbf{r})$ and reflects their inclusion in the general case of the electromagnetic field. The potential energy of interaction of polyelectrolyte units **E(r)** with the field instead of formula (21) will then be determined by the expression

$$V_{tot}(\mathbf{r}) = q'\varphi_Q(\mathbf{r}) - q'\int \mathbf{E}(\mathbf{r})\cdot d\mathbf{r}. \qquad (24)$$

.

In the case of polyampholyte, with an electric dipole moment **p** of the link, this energy takes the form $V_{tot}(\mathbf{r}) = \mathbf{p}\nabla\varphi_Q(\mathbf{r}) - \mathbf{pE}(\mathbf{r})$. The spatial distribution of the unit density $n(\xi,\eta)$ of a polyelectrolyte macrochain adsorbed by a polarized nanospheroid, taking into account the delay effects, will be given, as before, by formula (23), but with the interaction energy $V_{tot}(\mathbf{r})$ defined by formula (24).

3. Molecular dynamics simulation

Molecular dynamics (MD) simulation of polyampholytic polypeptides on the surface of a spherical germanium nanoparticle was performed using the NAMD 2.14 software package [26]. A model of a germanium nanoparticle was obtained by cutting a ball with a radius of 2.4 nm from a germanium crystal, and its atoms remained fixed during the simulation. Three generally neutral polyampholytic polypeptides have been considered:

1) **P1** polypeptide consisting of 400 amino acid residues with 320 Ala units with evenly distributed 40 Asp units (D, charge -1*e*) and 40 Arg units (R, charge +1*e*) – $(A_2DA_4RA_2)_{40}$;

2) **P2** polypeptide – $(A_4R_2A_8D_2A_4)_{20}$;

3) **P3** polypeptide – $A_8(A_8D_2A_{16}R_2A_8)_{11}A_8$.

For polypeptides, the CHARMM36 force field was used [27-28]. Non-covalent interactions with a germanium nanoparticle were described by the Lennard-Jones potential parameterized in the UFF force field [29]. This force field is widely used in the study of various molecular systems by the MD, including the study of the adsorption of molecules on various solid surfaces [30-31]. The van der Waals potential was cut off at a distance of 1.2 nm using a smoothing function between 1.0 and 1.2 nm. Electrostatic interactions were calculated directly at a distance of 1.2 nm, and at a larger distance, the Ewald particle-grid method (PME) [32] was used with a grid step of 0.11 nm. The entire nanosystem was placed in a cube with 22 nm edges filled with TIP3P water molecules [33].

First, modeling of polyampholytic polypeptides was carried out on the surface of a non-polarized germanium nanoparticle. The resulting conformational structures of polypeptides were used as starting points for modeling on the surface of a germanium nanoparticle polarized in an external static or alternating electric field. In total, three starting conformations were obtained for each considered polypeptide. In an external uniform electric field on the surface of a spherical semiconductor nanoparticle, charges are distributed with surface density σ_p proportional to the cosine of the angle θ between the direction of the electric field vector **E** and the normal to the nanoparticle surface [22, 34]:

$$\sigma_p = \frac{3p}{4\pi r}\cos\theta \ , \tag{25}$$

where p is the dipole moment of the ball and r is its radius.

Therefore, the polarization of a germanium nanoparticle was specified through a change in the partial charges of atoms on its surface according to the cosine law of the orientation angle of the normal [35]. The following peak values of the induced dipole moment of a spherical germanium nanoparticle were considered: $p_1 \approx 3.7$, $p_2 \approx 7.4$ и $p_3 \approx 14.8$ kD. In this case, at the positively charged pole of the nanoparticle, the atoms acquired partial charges induced by the electric field equal approximately to +0.1*e*, +0.2*e*, and +0.4*e*. In the case of static polarization of a germanium nanoparticle, MD simulation was performed at a constant temperature (Berendsen thermostat) at 900 K followed by a decrease to 300 K. This made it possible to reach deeper minima of the conformational energy of the macrochain, including in a shorter section of the trajectory [14, 17-18, 19-20]. At the same time, to control the obtaining of equilibrium conformations, the change in the mean square distance between polypeptide atoms in different conformations (RMSD) was monitored.

In addition, we considered the case when, in the course of MD simulation, the densities of induced charges on the surface of a germanium nanoparticle periodically changed in time according to the sine law with an oscillation period T = 2.4 ns during 4 oscillation periods. Each oscillation period was divided into 8 equal time segments of 0.3 ns each, during which the field did not change, and the value of the dipole moment of the nanoparticle in the selected segment was set by averaging it over the entire length of the segment. The dipole moment of the nanoparticle changed in the following sequence, starting from the starting conformation of the polypeptide: +0.69*p* (mean value in the range of oscillations from π/8 to 3π/8), +0.97*p* (from 3π/8 to 5π/8), +0.69*p* (from 5π/8 to 7π/8), 0 (from 7π/8 to 9π/8), -0.69*p* (from 9π/8 to 11π/8), -0.97*p* (from 11π/8 to 13π/8) , -0.69*p* (from 13π/8 to 15π/8), 0 (from 15π/8 to 17π/8). MD simulation with a

periodic change in the polarity of a germanium nanoparticle was performed at constant temperatures of 300 and 900 K [15-16, 20].

Based on the simulation results, the resulting conformations were used to calculate the radial distributions of the density of polypeptide atoms and the distributions of the linear density of polypeptide atoms along the polarization axis. The angular distributions of polypeptide atoms were also calculated.

4. Results of MD simulation

4.1 Rearrangement of the conformational structure of polyampholytic polypeptides upon static polarization of a germanium spherical nanoparticle

Figure 1a shows the conformation of the P1 polypeptide on the surface of a germanium spherical nanoparticle, obtained from the results of MD simulation on the surface of a non-polarized nanoparticle. Both the P1 polypeptide macromolecule (Fig. 1a) and the P2 and P3 polypeptides completely envelop the non-polarized germanium nanoparticle. These conformations of polypeptides were used as starting points in modeling on the surface of a polarized germanium nanoparticle, including with a periodic change in its polarity. Figure 2a shows the curves of radial distributions of the average density of atoms of the P1 polypeptide with differentiation according to the types of units. They have a peak at the surface of a nanoparticle, which is characteristic of the adsorption of macromolecules on the neutral surface of solid adsorbents of various shapes [14, 18]. Figure 3a shows the distributions of the average linear density of P1 polypeptide atoms on the surface of a non-polarized germanium nanoparticle. It can be seen that, on the whole, the atoms of the macrochain are distributed uniformly along the z axis (coinciding with the polarization axis of the nanoparticle upon further consideration).

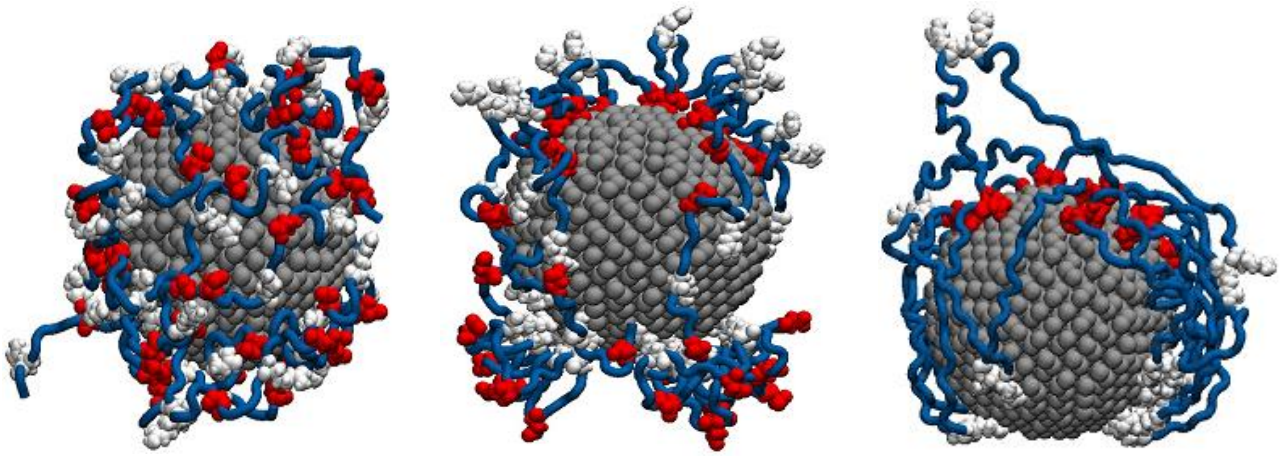

a b c

Fig.1 The conformational structure of polypeptides P1 (b) and P3 (c) at the end of MD simulation on the surface of a polarized germanium nanoparticle (the dipole moment is directed from bottom to top), as well as the starting conformation of the polypeptide P1 (a) on the surface of a non-polarized nanoparticle (blue tube - Ala units, Asp units are shown in red, Arg units are shown in white, germanium nanoparticles are shown in gray).

As the dipole moment of the germanium spherical nanoparticle increased, the conformational structure of the adsorbed polyampholyte changed due to the shift of charged amino acid residues to oppositely charged subpolar regions of the nanoparticle (Figs. 1b and 1c). For polypeptides P1 (Fig. 1b) and P2, in which the number of neutral units between the charged ones was less than that of the P3 polypeptide, the formation of a significant number of macrochain loops was observed on the surface of the polarized nanoparticle. They were stretched along the polarization axis of the nanoparticle, which led to the stretching of the macromolecular fringe. Such rearrangement began to occur from the value of the dipole moment equal to p_2 and higher. For the P3 polypeptide, the number of macrochain loops extended along the polarization axis from the surface of the nanoparticle was small. In this case, the charged amino acid residues Arg and Asp adsorbed at the poles of the polarized nanoparticle were linked by a fragment consisting of neutral Ala units located in the central region of the nanoparticle (Fig. 1c).

.

Previously, in [14], during MD simulation on the surface of a polarized spherical gold nanoparticle, a similar pattern of rearrangement of polyampholytic polypeptides with the same sequence of links was observed. However, in contrast to the germanium nanoparticle, such conformational changes began to occur at a surface charge density at the poles much higher than for the germanium nanoparticle: the charge of atoms at the pole on the gold nanoparticle was 0.5*e*, while on the germanium nanoparticle it was only 0.2*e*. This is due to the fact that the considered Lennard-Jones potential, which describes van der Waals interactions, was lower for germanium than for gold. In addition, the radius of the gold nanoparticle was smaller (1.5 nm), but the dipole moments of the nanoparticles were approximately the same: 5.5 kD for gold and 7.4 kD for germanium nanoparticles.

Such a rearrangement of the conformational structure of polyampholytic polypeptides on the surface of a polarized spherical germanium nanoparticle led to a change in the radial distributions of the average density of macrochain atoms (Fig. 2b). It can be seen that, compared with the distribution on a non-polarized nanoparticle (Fig. 2a), there was a decrease and broadening of the profile of the radial distribution over all atoms of the polypeptide. In this case, the charged units of Arg and Asp are mainly concentrated near the surface of the nanoparticle (Fig. 2b), which is associated with their adsorption at the poles of the germanium nanoparticle, while the neutral units of Ala are far from the surface. On the whole, the radial distributions of the mean atomic density of polyampholyte polypeptides on the surface of a polarized germanium nanoparticle turned out to be similar to the radial distributions of the atomic density of polyampholytes obtained for a polarized gold nanoparticle.

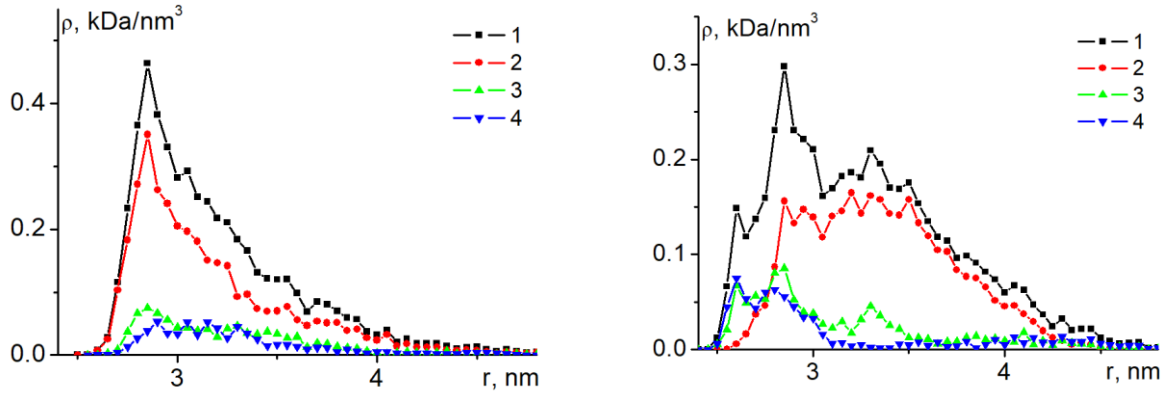

a b

Fig.2 Radial dependences of the average density of atoms of the P1 polypeptide with differentiation according to the types of links in the starting conformation on the surface of a non-polarized spherical nanoparticle (a), as well as at the end of MD simulation on the surface of a germanium nanoparticle polarized with a dipole moment p_3 (b) (1 - for all atoms of the polypeptide; 2, 3 and 4 - for Ala, Arg and Asp links, respectively).

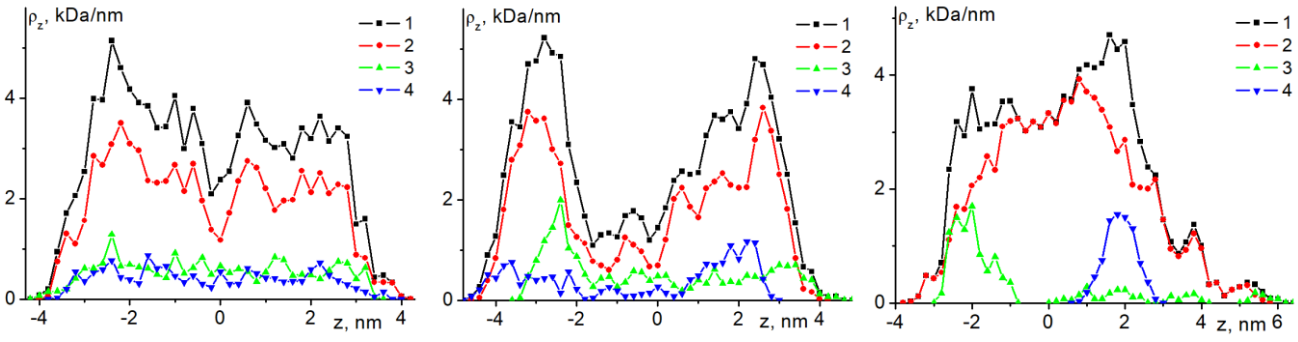

a b c

Fig.3 Distributions of the average linear density of atoms of the P1 polypeptide in the starting conformation (a), as well as of the polypeptides P1 (b) and P3 (c) at the end of the MD simulation on the surface of a spherical germanium nanoparticle polarized with a dipole moment p_3 (1 – over all atoms of the polypeptide; 2, 3 and 4 - for links Ala, Arg and Asp, respectively).

The distributions of the average linear density of polypeptide atoms along the nanoparticle polarization axis were also plotted (Fig. 3). On the surface of non-polarized spherical germanium nanoparticle, the links were generally distributed uniformly along the *z* axis of the nanoparticle directed along the polarization axis (Fig. 3a). On the surface of the polarized nanoparticle for polypeptides P1 (Fig. 3b) and P2, there was a significant change in the distribution profile of the average linear density of macrochain atoms with the appearance of peaks near the poles of the nanoparticle. This indicates a shift of the macrochain links to the subpolar regions of the nanoparticle. For the P3 polypeptide (Fig. 3c), mainly charged units were concentrated at the poles of the polarized germanium nanoparticle. At the same time, neutral amino acid residues Ala connected them, being located mainly in the central region of the nanoparticle (Fig. 1c).

4.2 Rearrangement of the conformational structure of polyampholytic polypeptides upon periodic change in the polarity of a germanium spherical nanoparticle

In the MD simulation of polyampholytic polypeptides on the surface of a germanium nanoparticle with a periodic change in its polarity over time at a temperature of 300 K and the peak value of the p_2 nanoparticle dipole moment, the macrochain units shifted to the equatorial region of the nanoparticle (Fig. 4). This is due to the fact that, upon polarization reversal of the nanoparticle, charged units of the polyampholyte are displaced from like-charged poles of the nanoparticle to the weakly charged equatorial region of the nanoparticle. They remain there due to the weak local electric field near the equator, held by the van der Waals attraction of the macrochain to the surface. Over time, after several periods of change in the polarity of the nanoparticle, all units of the polyampholyte shifted to its equatorial region.

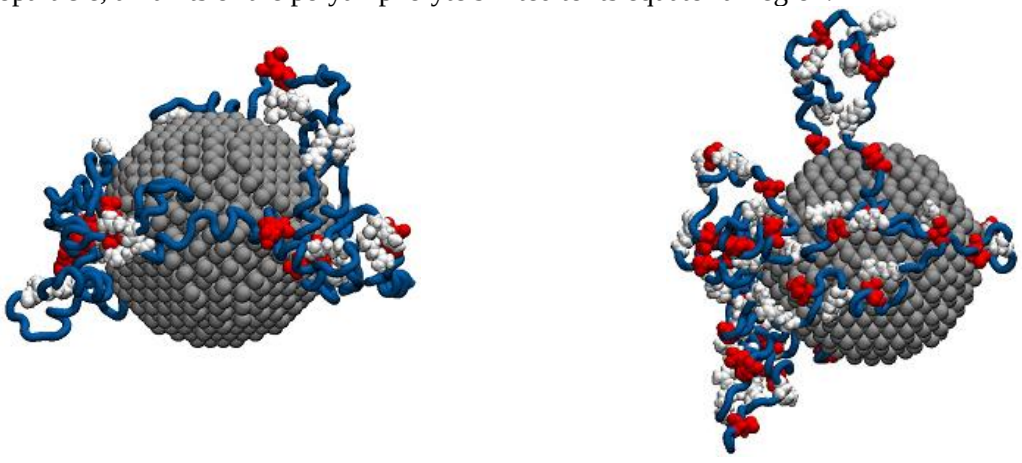

a b

Fig.4 Conformational structures of polypeptides P3 (a) and P1 (b) at the end of MD modeling at a temperature of 300 K with a periodic change in the polarity of the germanium nanoparticle at the peak value of the dipole moment of the nanoparticle equal to p_2 (blue tube - Ala units, Asp units are shown in red, and white – Arg).

Figure 5a shows the dependences of the angular distributions of atoms over all atoms of the P3 polypeptide and over its charged Arg units. The calculation of the angular distribution was carried out with a step of 10 degrees. The lower (Fig. 1 and Fig. 4) pole corresponds to an angle of 180 degrees, the equatorial region - an angle of 90 degrees, and the upper pole - an angle of 0 degrees. The dependences of the angular distributions of atoms of the adsorbed macrochain were normalized to the amplitude values of the concentration of atoms in the equatorial region, taking into account differences in the surface area of spherical belts bounded by circles of different radii: $N(\theta_1,\theta_2)=n(\theta_1,\theta_2)S(80,90)/S(\theta_1,\theta_2)$, where $S(80,90)$ - area of a spherical belt bounded by angles of 80 and 90 degrees, $N(\theta_1,\theta_2)$ - normalized number of macrochain atoms in a spherical belt, $n(\theta_1,\theta_2)$ - the number of macrochain atoms in the spherical belt, and $S(\theta_1,\theta_2)$ area of a spherical belt bounded by angles θ_1 and θ_2.

It can be seen that, compared with the initial conformational structure (Fig. 5a, curve 1) on the surface of an non-polarized nanoparticle, after modeling with a periodic change in the polarity of the nanoparticle, the angular distribution profile of the P3 polypeptide atoms narrowed and is located in the equatorial region (Fig. 5a, curve 2). It can also be seen that at the time when the dipole moment of the nanoparticle is maximum (Fig. 5a, curve 3), the dependence of the angular distribution of the P3 polypeptide atoms almost

.

did not change. This suggests that, upon repolarization of the nanoparticle, the macrochain remains near the equator.

Figure 5b shows that the profile of the radial distribution of the P2 polypeptide atomic density at the end of the MD simulation with a periodic change in polarity at 300 K and p_2 significantly decreased (curve 2) compared to the initial distribution (curve 1) and almost does not change during the last oscillation period (curve 3). This is due to the displacement of the polyampholyte to the equatorial region of the germanium nanoparticle. This character of the conformational rearrangement of polyampholyte polypeptides turned out to be similar to the conformational changes of polyampholytes on the surface of a gold nanoparticle in a microwave electric field [15].

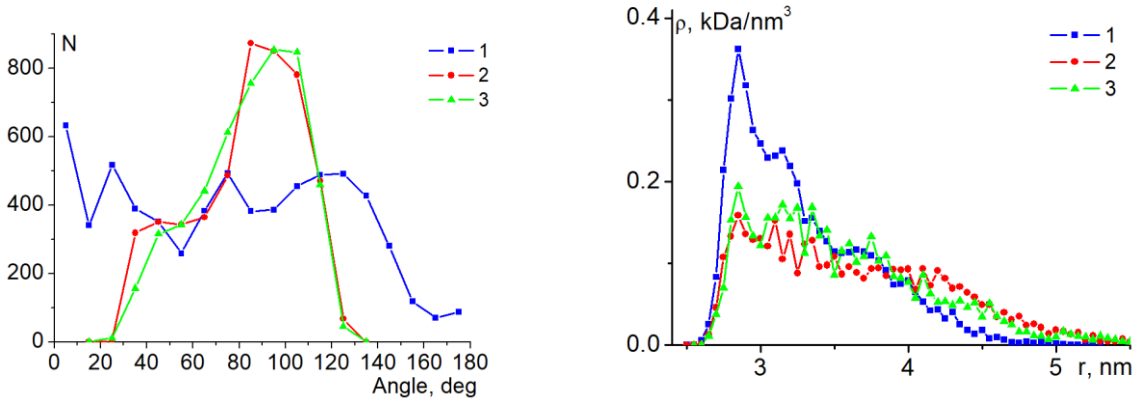

a b

Fig.5 Dependences of the angular distributions of atoms of the polypeptide P3 (a) and the radial distributions of the density of atoms of the polypeptide P2 (b) in the starting conformation (1), at the end of MD simulation (2) with a periodic change in the polarity of the germanium nanoparticle (peak dipole moment p_2) at a temperature of 300 K , as well as at the last simulation period at the time when the dipole moment of the nanoparticle is maximum (3).

In the case of MD simulation of all considered polypeptides on the surface of a germanium nanoparticle with a periodic change in time of its polarity at twice the peak value of the dipole moment of the nanoparticle p_3 and a temperature of 300 K, most of the polyampholyte units were desorbed during the considered time interval. In this case, a small part of the units of the macromolecule remained adsorbed in the equatorial region of the nanoparticle. This was due to the fact that at a higher peak value of the dipole moment of the nanoparticle, stronger changes in the local electric field occurred in its equatorial region, which led to an increase in the displacement amplitude of the charged units. In this case, the forces of attraction of the macrochain to the nanoparticle in the equatorial region were overcome, and most of the amino acid residues of the polyampholyte polypeptide were desorbed.

When modeling at a temperature of 900 K at the peak values of the dipole moment of the p_2 and p_3 nanoparticles, periodic changes in the conformational structure of the adsorbed polyampholytic polypeptide occurred following a change in the polarity of the germanium nanoparticle over time. In this case, potential barriers preventing changes in the conformation of the macrochain were easily overcome due to the high modeling temperature, and the conformational structure of the polyampholyte changed depending on the instantaneous value and direction of the dipole moment of the nanoparticle. Therefore, at the time moments when the dipole moment of the nanoparticle was maximum, the macromolecular fringe assumed an elongated shape, similar to the simulation for static polarization of the nanoparticle (Figs. 1b and 1c).

And at the end of the MD simulation sections, when the dipole moment of the nanoparticle was equal to zero, the polyampholyte shell acquired a shape enveloping the nanoparticle, similar to that shown in Figure 1a. At the same time, both radial and linear distributions of the density of polypeptide atoms at different time points were also similar to the distributions on the surface of a non-polarized (Figs. 2a and 3a) and polarized nanoparticles (Figs. 2b and 3b-c). And the profiles of distributions of the linear density of polypeptide atoms along the polarization axis along the charged amino acid residues Arg and Asp mirrored relative to the equator when the polarity of the nanoparticle was reversed (Figs. 3b and 3c).

4. Conclusion

Thus, a generalization was made of the mathematical model of the formation of a quasi-equilibrium macrochain layer for nanoparticles with low electrical conductivity, which are in an external harmonically varying electric field with a frequency significantly lower than the plasma frequency of the nanoparticle material. With this approach, the permittivity and electrical conductivity of the particle material are simultaneously introduced into consideration. The frequency dependences of the dipole polarizabilities of a sphere and a spheroid manifest themselves most noticeably in the case of semiconductor nanoparticles with an electrical conductivity σ of the order of 10^9-10^{10} Hz, i.e. of the same order of magnitude with the frequencies of the external field. Conductivity of this order is typical for pure or lightly doped semiconductors like Ge. Within the framework of the proposed model, the effect of switching the sign of the nanoparticle polarization upon reaching a certain characteristic frequency of the field, which depends on the conductivity σ of the nanoparticle material, its permittivity, and the depolarization coefficients of the spheroid, was found. It has been shown that adsorption of polymers on lightly doped semiconductor nanoparticles gives rise to the possibility of a more flexible control action on conformational transitions in the macrochain fringe by an alternating electric field of an arbitrarily varied frequency in the range of 10^9-10^{10} Hz. A new version of the theoretical model has been constructed with going beyond the quasi-static approximation, that is, taking into account the delay effects, the manifestation of which is more noticeable for extended nanostructures. The use of this version of the model leads to the appearance of an azimuthal component of the electric field strength, which was absent in the implementation of the quasi-static approximation. This complicates the structure of the resulting field for spheroids with a large long semiaxis.

The performed MD simulation showed that on the surface of a spherical germanium nanoparticle in an external static or alternating electric field of the microwave range, the nature of conformational changes in generally neutral polyampholyte polypeptides with different distribution laws of charged units turned out to be similar to the rearrangement of polyampholyte conformations on the surface of a spherical gold nanoparticle [14-15]. On the surface of a spherical germanium nanoparticle, with an increase in its dipole moment, such a rearrangement of the conformational structure of the polyampholyte occurred, in which part of its charged units shifted to strongly charged subpolar regions. If the distance between oppositely charged units was small compared to the diameter of the nanoparticle, then a large number of macrochain loops were formed, which were extended along the polarization axis of the nanoparticle. And when the distance between the oppositely charged units exceeded the diameter of the nanoparticle, then most of the charged units of the polypeptide were concentrated on the oppositely charged poles of the nanoparticle. In the case of MD simulation, on the surface of a germanium nanoparticle with a periodic change in its polarity in time at a small amplitude of the polarizing alternating electric field, an encircling annular polyampholytic fringe was formed in its equatorial region. With an increase in the amplitude of the polarizing alternating electric field, desorption of most of the polyampholyte units from the surface of the nanoparticle occurred.

Germanium nanoparticles with a macromolecular shell, the shape of which is sensitive to the action of an external electric field, can be used to create hybrid nanosystems with the possibility of field control of its plasmonic properties. Changes in the conformations of molecules of the surface layer of the polymer affect the effective value of the edge layer, and thus, the characteristics of the field outside the nanoparticle associated with its plasmonic properties. Such hybrid nanosystems with plasmon characteristics controlled by an electric field can find wide application in the creation of various chemical sensors, as well as nanoprobes in biomedicine.

Acknowledgments

This work was supported by the Ministry of Science and Higher Education of the Russian Federation within the framework of project no. FSGU-2023-0003.

REFERENCES

1 Lowe S.B., Dick J.A.G., Cohen B.E., et al. Multiplex sensing of protease and kinase enzyme activity via orthogonal coupling of quantum dot–peptide conjugates. *ACS Nano*, 2012, Vol. 6, pp. 851-857. doi:10.1021/nn204361s.

2 Yang L., Ahn D.J., Koo E. Ultrasensitive FRET-based DNA sensor using PNA/DNA hybridization. *Materials Science and Engineering: C*, 2016, Vol. 69, pp. 625-630. doi:10.1016/j.msec.2016.07.021.

.

3 Perng W., Palui G., Wang W., Mattoussi H. Elucidating the role of surface coating in the promotion or prevention of protein corona around quantum dots. *Bioconjugate Chem*., 2019, Vol. 30. pp. 2469-2480. doi:10.1021/acs.bioconjchem.9b00549.

4 Green C.M., Spangler J., Susumu K., et al. Quantum dot-based molecular beacons for quantitative detection of nucleic acids with CRISPR/Cas(N) nucleases. *ACS Nano*, 2022, Vol. 16. pp. 20693-20704. doi:10.1021/acsnano.2c07749.

5 Jin Z., Dridi N., Palui G. et al. Quantum dot–peptide conjugates as energy transfer probes for sensing the proteolytic activity of matrix metalloproteinase-14. *Anal. Chem*., 2023, Vol. 95, pp. 2713–2722. doi:10.1021/acs.analchem.2c034002713-2722.

6 Nejad Z.K., Khandar A.A., Khatamian M. Graphene quantum dots based MnFe2O4@SiO2 magnetic nanostructure as a pH-sensitive fluorescence resonance energy transfer (FRET) system to enhance the anticancer effect of the drug. *Intern. Journal of Pharmaceutics*, 2022, Vol. 628. pp. 122254. doi: 10.1016/j.ijpharm.2022.122254.

7 Tade R.S., Patil P.O. Fabrication of poly (aspartic) acid functionalized graphene quantum dots based FRET sensor for selective and sensitive detection of MAGE-A11 antigen. *Microchemical Journal*, 2022, Vol. 183, pp. 107971. doi:10.1016/j.microc.2022.107971.

8 Nevidimov. A.V., Razumov V.F. Nonradiative Energy Transfer in "Colloidal Quantum Dot Nanocluster–Dye" Hybrid Nanostructures: Computer Experiment. *High Energy Chemistry*, 2020, Vol. 54, pp. 28–35. https://doi.org/10.1134/S0018143920010105.

9 Nikolenko L.M., Pevtsov D.N., Brichkin S.B. Quantum-size effect for intraband electronic transition in colloidal silver selenide quantum dots. *High Energy Chemistry*, 2022, Vol. 56, pp. 380–382. doi:10.1134/S0018143922050125.

10 Cantini E., Wang X., Koelsch P., et al. Electrically Responsive Surfaces: Experimental and Theoretical Investigations. *Acc. Chem. Res.*, 2016, Vol. 49, pp. 1223–1231. doi:10.1021/acs.accounts.6b00132.

11 Zhao J., Wang X., Jiang N. et al. Polarization Effect and Electric Potential Changes in the Stimuli-Responsive Molecular Monolayers Under an External Electric Field. *J. Phys. Chem. C*, 2015, Vol. 119, pp. 22866–22881. doi:10.1021/acs.jpcc.5b04805.

12 Ghafari A.M., Domínguez S.E., Järvinen V. et al. In Situ Coupled Electrochemical-Goniometry as a Tool to Reveal Conformational Changes of Charged Peptides. *Advanced Materials Interfaces*, 2022, Vol. 9, pp. 2101480. doi:10.1002/admi.202101480.

13 Gomes B.S, Cantini E., Tommasone S. et al. On-Demand Electrical Switching of Antibody–Antigen Binding on Surfaces. *ACS Appl. Bio Mater.*, 2018, Vol. 1, pp. 738–747. doi:10.1021/acsabm.8b00201.

14 Kruchinin N.Y., Kucherenko M.G. Molecular-dynamics simulation of rearrangements in the conformational structure of polyampholytic macromolecules on the surface of a polarized metal nanoparticle. *Colloid Journal*, 2020, Vol. 82, pp. 136-143. doi:10.1134/S1061933X20020088.

15 Kruchinin N.Y., Kucherenko M.G. Conformational rearrangements of polyampholytic polypeptides on metal nanoparticle surface in microwave electric field: molecular-dynamics simulation. *Colloid Journal*, 2020, Vol. 82, pp. 392-402. doi:10.1134/S1061933X20040067.

16 Kruchinin N.Yu., Kucherenko M.G. Rearrangement of the conformational structure of polyampholytes on the surface of a metal nanowire in a transverse microwave electric field. *Eurasian phys. tech. j.* 2021, Vol.18, pp. 16-28. doi:10.31489/2021No1/16-28.

17 Kucherenko M.G., Kruchinin N.Yu., Neyasov P.P. Modeling of conformational changes of polyelectrolytes on the surface of a transversely polarized metal nanowire in an external electric field. *Eurasian phys. tech. j.* 2022, Vol. 19, pp. 19-29. doi:10.31489/2022No2/19-29.

18 Kruchinin N.Yu., Kucherenko M.G. Rearrangements in the conformational structure of polyampholytic polypeptides on the surface of a uniformly charged and polarized nanowire: Molecular dynamics simulation. *Surfaces and Interfaces*, 2021, Vol. 27, pp. 101517. doi:10.1016/j.surfin.2021.101517.

19 Kruchinin N.Yu., Kucherenko M.G. Molecular dynamics simulation of the conformational structure of uniform polypeptides on the surface of a polarized metal prolate nanospheroid with varying pH. *Russian Journal of Physical Chemistry A*, 2022, Vol. 96, pp. 624-632. doi:10.1134/S0036024422030141.

20 Kruchinin N.Yu., Kucherenko M.G. Modeling of electrical induced conformational changes of macromolecules on the surface of metallic nanospheroids. *Materials Today: Proceedings*, 2022, Vol. 71, Part 1, pp. 18-30. doi:10.1016/j.matpr.2022.07.139.

21 Kruchinin N.Yu., Kucherenko M.G. Rearrangements in the conformational structure of polyelectrolytes on the surface of a flattened metal nanospheroid in an alternating electric field. *Colloid Journal*, 2023, Vol. 85. pp. 44-58. doi:10.1134/S1061933X22600440.

22 Landau L.D., Pitaevskii L.P., Lifshitz E.M. Electrodynamics of Continuous Media, 2nd Edition, Elsevier Ltd., 1984, 460 p.

23 Grosberg A.Y., Khokhlov A.R. Statistical Physics of Macromolecules, 1994, AIP Press, New York. 347 p.

24 Klimov V.V. Nanoplasmonics, 2009, Moscow: Fizmatlit, 480 p. [in Russian]

25 Budak B.M., Samarskii A.A., Tikhonov A.N. Collection of problems in mathematical physics, 1979, M.: Science, 686 p. [in Russian]

26 Phillips J.C., Braun R., Wang W., et al. Scalable molecular dynamics with NAMD. *J Comput Chem*., 2005, Vol. 26, pp. 1781-1802. https://doi.org/10.1002/jcc.20289.

27 MacKerell A.D. Jr., Bashford D., Bellott M., et al. All-atom empirical potential for molecular modeling and dynamics studies of proteins *J. Phys. Chem. B*, 1998, Vol. 102, pp. 3586-3616. doi:10.1021/jp973084f.

28 Huang J., Rauscher S., Nawrocki G. et al. CHARMM36m: an improved force field for folded and intrinsically dis-ordered proteins. *Nature Methods*, 2016, Vol.14, pp. 71-73. doi:10.1038/nmeth.4067.

29 Rappe A.K., Casewit C.J., Colwell K.S., et al. UFF, a full periodic table force field for molecular mechanics and molecular dynamics simulations. *J. Am. Chem. Soc*., 1992, Vol. 114, pp. 10024–10035. doi:10.1021/ja00051a040.

30 Eidani M., Akbarzadeh H., Mehrjouei E., et al. Thermal stability and melting mechanism of diamond nanothreads: Insight from molecular dynamics simulation. *Colloids and Surfaces A: Physicochemical and Engineering Aspects*, 2022, Vol. 655, pp. 130248. doi:10.1016/j.colsurfa.2022.130248

31 Marashizadeh P., Abshirini M., Saha M., et al. Interfacial properties of ZnO nanowire-enhanced carbon fiber composites: a molecular dynamics simulation study. *Langmuir*, 2021, Vol. 37, pp. 7138–7146. doi:10.1021/acs.langmuir.1c00711.

32 Darden T., York D., Pedersen L. Particle mesh Ewald: An N·log(N) method for Ewald sums in large systems. *J. Chem. Phys.*, 1993, Vol. 98, pp. 10089-10092. doi:10.1063/1.464397.

33 Jorgensen W.L., Chandrasekhar J., Madura J.D., et al. Comparison of simple potential functions for simulating liquid water. *J. Chem. Phys.*, 1983, Vol. 79, pp. 926-935. doi:10.1063/1.445869.

34 Izmailov S.V. Electrodynamics course, 1962, M .: State educational and pedagogical publishing house of the Ministry of Education of the RSFSR, 439 p. [in Russian]

35 Shankla M., Aksimentiev A. Conformational transitions and stop-and-go nanopore transport of single-stranded DNA on charged grapheme. *Nat Commun*., 2014, Vol. 5, pp. 5171. doi:10.1038/ncomms6171.

Article accepted for publication 13.05.2023

.

DOI 10.31489/2023No3/20-26

UDC 620.193

REASON OF CORROSION OF ALUMINIUM PRODUCTS IN SEA WATER

Berdibekov A.T.[1], Khalenov O.S.[2]*, Zinoviev L.A.[2], Laurynas V.Ch.[2], Gruzin, V.V.[1], Dolya, A.V.[1]

[1] Research Institute of Arms and Military Equipment of the Military Research Center of the National Defense University named after the First President of the Republic of Kazakhstan – Elbasy, Astana, Kazakhstan

[2] E.A. Buketov Karaganda University, Karaganda, Kazakhstan, otangaliy@gmail.com

In this paper, the cause of corrosion of aluminium products in sea water is proposed. Corrosion is caused by incomplete oxidation of aluminum cells on the surface of products. Incomplete oxidation of aluminium cells occurs due to lack of energy in oxygen molecules. It is necessary to significantly increase the energy of oxygen molecules for oxidation the rhombic subsystem of a cubic face-centered aluminum cell. It is shown a significant decrease in the rate of the chemical reaction for the treated aluminium foil interacted with iodine in alcohol solution. The foil was in contact with oxygen heated to 450 °C and subjected to ultraviolet irradiation at the same time. It was pretreated for 12 hours. It is assumed that 12 hours of contact the foil with reactive oxygen species, most of the aluminium cells on the surface of the foil samples have been completely oxidised. This foil doesn't react chemically with halogens.

Keywords: Quantum-chemical calculations, aluminium, alumina, cubic subsystem, oxidation, halogens.

1. Introduction

Due to the fact that the development of new alloys with given properties is a time-consuming and expensive process, the use of techniques that allow to exclude obviously inefficient areas of research is a very relevant task [1-6]. One of the most promising methods for such a choice is quantum-chemical calculation methods. However, when using these methods, the question of confidence in them very often arises. In order to find out the degree of such trust, it is possible to carry out verification calculations of known objects and to determine the degree of correspondence of the results of such calculations to reality. If the results of the calculations coincide with experimental data, these types of calculations can already be used to predict the properties of newly developed alloys [2, 5].

On the other hand, to conduct quantum chemical calculations require large computing power, while the amount of time used depends on the number of electrons in the electron shell of the atoms of the investigated metals. The number of electrons in the electron shell increases too with increasing order number of metal in the periodic table. It dramatically increases the complexity and time of quantum-chemical calculations. In this regard, it was decided to test possibility to calculate the crystal structure of metals. The calculation is carried out on the example of light metal atoms, located in the first 3 rows of the periodic system of Mendeleev. For such calculations semi-empirical parametric method 3 can be used which allows calculating parameters of atoms having electrons on s- and p- electron shells in atoms [7].

In addition, this parametric method 3 was originally designed to calculate compounds containing elements such as aluminium, oxygen and all halogens [8].

Therefore, the metal aluminium, which is widely used in production and whose properties are fairly well known, is the most suitable object for the verification calculations.

2. Materials and experimental details

The structure of aluminium and its oxidised forms was calculated using the parametric method 3, which was specially developed for calculations of compounds containing aluminium and halogen atoms [8]. In the aluminium unit cell model 14 atoms were present for the calculations. When modeling the oxidation process of the cubic subsystem of the face-centered cubic lattice of aluminium, 12 atoms of oxygen were added. To determine the effect of oxygen simultaneously on the cubic and rhombic subsystems of the aluminium

lattice, 13 to 21 oxygen atoms were used. Models in which there was a gradual increase in the number of oxygen atoms in the rhombic subsystem of the aluminium lattice with a fully oxidised cubic subsystem were used. The presence of even one oxygen atom in the rhombic subsystem completely stops the chemical interaction of the oxidised aluminium cell with halogen ions and a further increase in the number of oxygen atoms in the rhombic subsystem also blocks the chemical interaction with halogens.

Up to 4 halogen ions were used to evaluate the nature of the interaction of negative halogen ions with the lattice models of oxidised aluminium. Four different halogens (chlorine, bromine, iodine, fluorine) were used.

Experiments with different samples of untreated and treated aluminium were performed to verify the results of the calculations. Untreated aluminium foil samples, corundum (aluminium oxide, with a share of aluminium oxide more than 99 % wt.) and treated aluminium foil samples were used. All these samples were placed in an alcohol solution containing 5 % wt. of iodine. The mass of the samples before and after placing them in the solution was measured on a RADWAG AS 60/220.R2 electronic scale. The measurements were carried out with an accuracy of up to ten thousandths of a gram.

Untreated aluminium foil samples with a share of aluminium not less than 99,5 % were used for the experiment. Treated samples were obtained by heat treatment and treatment under an ultraviolet lamp of the air entering the surface of the samples. The aluminium foil samples and the air entering these samples were heated to a temperature of 450 °C with simultaneous irradiation of the incoming heated air by the ultraviolet radiation of the DRT-400 lamp. The DRT-400 lamp produces broadband ultraviolet radiation in the range from 220 nm to 340 nm.

3. Results and discussion

First of all, the parametric method 3 was used to calculate the structure of a single aluminium cell which can be represented as a rhombus within a cube, i.e. as a face-centered cubic lattice [9]. In such lattices each side of the cube has an aluminium atom in its centre - 8 aluminium atoms are in the nodes of the cubic subsystem (atoms 7-10 and 11-14) and 6 aluminium atoms are in the rhombic subsystem of the face-centered cubic lattice (the aluminium atoms of the rhombic subsystem are in the centre of the cube sides (atoms 1, 2, 3, 4, 5, 6), Figure 1. There are no atoms in the centre of the aluminium lattice, which makes aluminium well malleable. The numbering of aluminium atoms is the same in all the presented figures, Figures 1-5.

Calculation shows that on aluminium atoms of cubic subsystem of the cell positive charges are localised (from +0.1 the value of the electron charge (electron) to +0.2 electron), and on aluminium atoms of rhombic structure negative charges are localised (from -0.2 electron to -0.25 electron). This type of charge configuration gives more stability to the aluminium cell (each of the positively charged aluminium atoms in any of the faces is attracted to a negatively charged aluminium atom located in the centre of the face). At the same time localisation of enough big negative charges in the centre of aluminium cell faces stabilises geometry of aluminium cell (aluminium cell cannot collapse) because of electrostatic repulsion of negative charges located in the centre of every face from each other. The cell of pure aluminium can also be represented as a system consisting of three planes: the central negatively charged plane (atoms 3, 4, 5, 6) is attracted to the two positively charged outer planes, the upper (atoms 7, 8, 9, 10) and the lower (11, 12, 13, 14). Atoms 1, 2 have negative charges localised on them, Figure 1.

Further calculations were carried out for a partially oxidised aluminum cell. It is known that when interacting with oxygen, the surface of aluminium is covered with a strong, chemically inactive aluminium oxide film 30 Å or thicker [10]. This film protects pure aluminium from the aggressive effects of the external environment. The oxidation of the aluminium cell was calculated. Variants of the interaction of the aluminium cell with a varying number of oxygen atoms from one atom to twelve atoms were calculated (the variant in which complete oxidation of the face-centered cubic aluminium cell structure), Figure 2.

Calculations have shown that the oxygen atoms form covalent bonds with the aluminium atoms in the cubic lattice of the aluminium unit cell.

The general symmetry of the aluminium cell at full oxidation of the cubic subsystem practically does not change. Preservation of symmetry to a certain extent proves the correctness of the calculation, because under severe strain in the cells of oxidised aluminium a film of aluminium oxide, poorly adhering to the surface of pure aluminium and poorly protecting the surface of pure aluminium from chemical interactions, should arise. An example of this type of oxide film weakly adhering to the metal surface is the rust that forms on the surface of iron products during iron oxidation [11]. However, it is known that the oxide film on

.

the surface of aluminium is very strongly bonded to the mass of pure aluminium underneath the film. During oxidation of cubic subsystem of aluminium cell the distribution of charges in the cell changes - on all oxidised aluminium atoms of cubic subsystem positive charges (+0.18 electron, +0.22 electron) are localised: on aluminium atoms number 1, 2, 4, 6 of rhombic subsystem very significant positive charges +0.7 electron are localised.

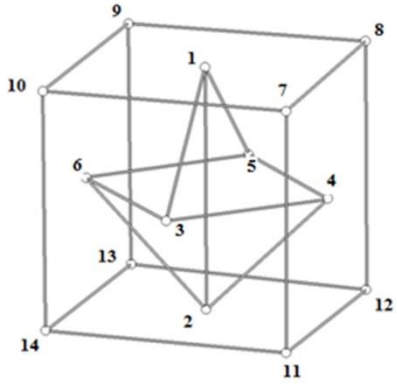

Fig.1. Schematic diagram of the pure aluminum crystal lattice.

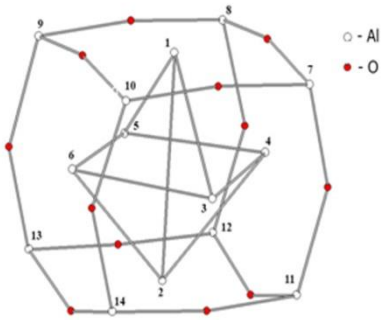

Fig.2. Face-centered cubic lattice of an oxidised aluminum cell. Only the cubic subsystem of the face-centered lattice is oxidised. Oxygen atoms are red circles.

Negative charges are localised on all oxygen atoms and aluminium atoms number 3, 5, Figure 2. Thus, around an aluminium cell with oxidised cubic subsystem an electrostatic field is established which allows chemical interaction of negative ions with an aluminium cell only if the negative ions are in close proximity to aluminium atom 1, Figure 2.

Nevertheless, some atoms can pass through the oxide aluminium film as it is known. For example, that the thickness of oxide layer on the surface of aluminium can be significantly increased when aluminium is heated up to 450 °C. The increase in thickness of oxide layer on aluminium surface indicates that this oxide layer is permeable to oxygen molecules or atoms. It is also known that seawater degrades aluminium products over time [12]. The degradation of the mass of pure aluminium under the aluminium oxide film can occur either from the destruction of the oxide film (unlikely as aluminium oxide is a chemically strong compound) or from the penetration of chemically active elements (such as halogen ions) under the oxide film [12].

In order to clarify the mechanism of aluminium surface destruction in seawater, calculations have been made for the interaction of aluminium cells with fully oxidised cubic lattice subsystems with halogen ions (chlorine, bromine, iodine, fluorine) present in large quantities in seawater [13]. Calculations have shown that there is no chemical interaction of negatively charged halogen ions with aluminium atoms located in oxidised cubic sublattices of aluminium cells. Any one of the aluminium atoms in the cubic sublattice is chemically bonded to the three nearest oxygen atoms, together forming an oxidised aluminium film, Figure 3. Thus, the negatively charged halogen ions present in seawater cannot destroy the structure consisting of oxidised aluminium atoms (the halogen ions are in physical interaction with the cubic lattice subsystem of aluminium, forming an ion- halogen shell around the aluminium surface).

However, it is known from experience that products made of aluminium in seawater corrode and cause damage to these products. Taking into account abovementioned facts we can draw conclusion that corrosion of aluminium ware in sea water occurs because of destruction of rhombic sublattice of aluminium cells (fully oxidised cubic sublattice of aluminium is chemically inert): halogen ions can cooperate only with aluminium atom located in the centre of outer surface of aluminium cell (in this atom is designated as atom number 1, this atom is a part of rhombic sublattice), Figure 1. Calculations showed a very strong interaction of negatively charged halogen ions with aluminium atom number 1 in the aluminium cell. In fact, the halogen ions tore this aluminium atom out of the cell structure aluminium, Figure 4.

Calculations showed that bromine and fluorine ions interact most strongly with the central atom of the aluminium surface. It was shown that bromine or fluorine ion interacts with the central aluminium atom number 1 of the outer plane of the oxidised aluminium cell, the bond length between the aluminium atoms

number 1 and number 2 increases considerably and the aluminium atom number 1 extends beyond the aluminium cell, Figure 4. The bond length between aluminium atom number 1 and number 2 increases by 0.9 Å when interacting with the bromine ion (and by 1.3 Å when interacting with the fluorine ion), Figure 4. Actually, it corresponds to the tearing out of the structure of the non-oxidised cubic subsystem of the aluminium cell by aluminium atom number 1. When interacting with iodine and chlorine ions, the bond length increases by no more than 0.6 Å, i.e. the ions of these halogens also produce the destruction of the aluminium surface, but at a slower rate than the fluorine and bromine ions.

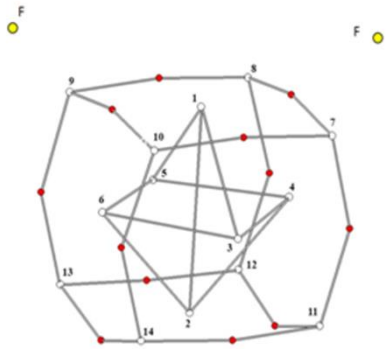

Fig.3. Scheme of the interaction of halogen ions with the oxidised cubic sublattice of aluminum cells.

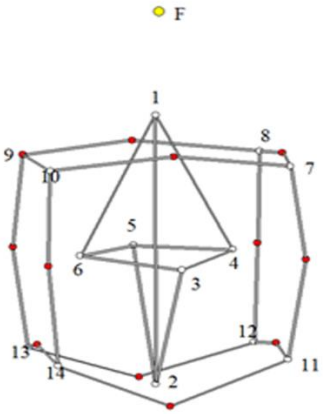

Fig.4. Interaction of the fluorine ion with the central atom of the aluminum cell.

In order to determine whether under normal conditions the oxidation of aluminium atoms in a rhombic subsystem was possible, we calculated the possible interaction of halogen ions with the oxidised aluminium cell taking into account that the oxygen atom localised in the centre of the aluminium cell with the formation of a covalent bond with the aluminium atom number 1 (this aluminium atom is in the centre of the aluminium cell outer plane) and aluminium atom number 2 (this aluminium atom is in the centre of the aluminium cell lower plane), Figure 4. It was assumed that the rhombic subsystem was a covalent bond with the aluminium atom number 1. All aluminium atoms (7, 8, 9, 10, 11, 12, 13, 14) of the cubic subsystem of the face-centered structure of the aluminium cell are covalently connected with oxygen atoms, Figure 5. That is, the whole cubic subsystem of the aluminium cell is oxidised, and in the rhombic subsystem aluminium atoms number 1 and number 2 are partially oxidised.

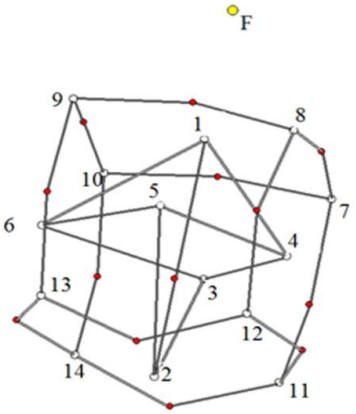

Fig.5. The interaction of the fluorine ion with the aluminum atom number 1. This aluminum atom is in a chemical bond with an oxygen atom that has penetrated into the center of the cell.

Calculations have shown that in the oxidised aluminium cell during the interaction of the aluminium atom number 1 with a negative fluorine ion (iodine, chlorine, bromine) the distance increased by 0.3 Å between the oxygen atom in centre of the cell and aluminium atom number 1, i.e. the distance is practically unchanged, Figure 5. This means that there is no tearing of aluminium atom number 1 from aluminium cell (no chemical reaction between negative halogen ion and aluminium atom number 1), Figure 5. There is no

.

damage to the structure of aluminium cell. The variants of calculation of interaction of halogen ions with an aluminium cell with various degrees of oxidation of rhombic subsystem up to full oxidation of rhombic subsystem (with fully oxidised cubic subsystem) also revealed complete absence of chemical interaction of negative halogen ions with the central atom of the upper plane of the aluminium cell (aluminium atom number 1). If aluminium cells under normal conditions is fully oxidised both subsystems - cubic and rhombic (such system is known as corundum), it is known from practice that in seawater containing halogen ions (chlorine, iodine, bromine, fluorine) the destruction of aluminium products still occurs.

Further comparison of calculation results with known facts about corrosion of aluminium surface in sea water was made [12]. Thus, in normal conditions (medium temperature 20 °C, pressure 10^5 Pa., oxygen 21 vol. % in atmosphere oxidation of aluminium atoms (numbers 1, 3, 4, 5, 6, 2,) of rhombic subsystem of face-centered cubic lattice of aluminium cell does not occur Figure 2, 4 [14, 15].

It is due to the fact that under normal conditions the rhombic cell structure of aluminium products is not oxidised and corrosion of aluminium products in sea water occurs. This allows us to conclude that the destruction of the surface of oxidised aluminium in seawater begins at the central aluminium atom (atom 1 of aluminium) of the face (this square consists of atoms numbers 7, 8, 9, 10, 1) of the face-centered cubic lattice bordering sea water, Figure 4. All other aluminium atoms (numbers 7, 8, 9, 10) at the surface bordering seawater are in an oxidised state (chemically inert), Figure 3.

To verify the results of the calculations, experiments were carried out with different aluminium samples:

1) Untreated aluminium foil was placed for 24 hours in 5 % wt. of iodine in alcohol solution at 20 °C. The given aluminium foil sample has almost completely dissolved in iodine solution, which corresponds to the literature data [16]. It does not contradict results of the calculations according to which aluminium film in which cubic subsystem is completely oxidised, but rhombic subsystem is not, is destroyed through interaction of negative halogen ions with the central atom of the outer side of the oxidised aluminium cell.

2) A fully oxidised aluminium (corundum) grade plate was also placed at the alcohol solution of iodine. The mass of the corundum plate did not change during this period of time. The measurements were taken with an accuracy of ten thousandth of a gram on electronic brand scales. Corundum was used in the experiment as a fully oxidised form of aluminium in which both the cubic and rhombic subsystems were completely oxidised in all cells. The absence of change in the mass of the corundum plate is consistent with the calculation results that there is no chemical interaction with halogen ions in the aluminium cell with fully oxidised cubic and rhombic subsystems, Figure 5. That is, the experimental results showed a very strong interaction of the halogens with the aluminium surface where there are no fully oxidised aluminium cells. It also showed a complete lack of chemical interaction with the surface where all the aluminium cells are fully oxidised.

It was assumed, that the time of dissolution of common aluminium foil in iodine solution would increase, if a certain number of cells on the surface of the aluminium foil were completely oxidised: It was supposed that the more aluminium cells were completely oxidised, the longer would be the dissolution time of the aluminium foil. In order to develop a technique to create conditions for the complete oxidation of aluminium cells on the aluminium surface it was assumed that under normal conditions for the oxidation of the rhombic subsystem of the aluminium cell oxygen molecules do not have enough energy (vibrational and electronic energy of oxygen molecules) to overcome the potential barriers around the aluminium atoms of the rhombic subsystem. If the energy of oxygen molecules increases more than some value, aluminium atoms of rhombic subsystem will start to oxidise in aluminium cells bordering with the atmosphere containing oxygen.

In order to increase vibrational and electronic energy of oxygen molecules the samples of aluminium foil and incoming air were heated up to 450 °C with the simultaneous irradiation of incoming heated air by ultraviolet radiation (DRT-400 lamp). Heating the air to 450 °C increased the vibrational energy of oxygen molecules. Broad-band ultraviolet radiation (220 nm – 340 nm) generates ozone O_3 formation and transfers oxygen molecules from the basic chemically inactive triplet state $^3O_2$, to the excited singlet state $^1O_2$ (the singlet state energy $^1O_2$ is 0.98 electron volt higher than the basic triplet state $^3O_2$) [17]. Ozone O_3 and singlet oxygen $^1O_3$ have a significantly higher chemical activity than oxygen molecules in the ground triplet state [18]. Samples of aluminium foil were exposed to reactive oxygen species at 4 and 12 hours. The treated aluminium samples were then placed for 24 hours in containers with the alcohol solution of iodine. As a result, it was found that the aluminium sample placed under ultraviolet radiation at 450 °C for 4 hours lost during 24 hours in the alcohol solution of iodine ~ 70 % of its weight (the weight of the aluminium sample

before placing it into the iodine solution was 0.0287 grams, after 24 hours the sample weight was 0.0088 grams, but it remained intact, unlike the sample of the same aluminium foil which has not undergone any treatment.

The aluminium foil sample that was placed under ultraviolet radiation at 450 °C for 12 hours lost only ~ 5 % of its weight in a 5 % wt. alcohol solution of iodine during one day (the weight of the foil sample before placing it into the iodine solution was 0.0367 grams, while after one day, the sample weighed 0.0350 grams). A protective layer has formed on the surface of the aluminium foil sample subjected to the 12-hour treatment. This protective layer doesn't react chemically with halogen ions. The fact that the sample of aluminium subjected to the 4-hour treatment isn't completely dissolved in a solution of iodine. It indicates that in this sample such a protective layer was also formed, but this protective layer didn't cover the entire surface of the sample. That is not in all cells of the aluminium on the surface of the aluminium foil occurred complete oxidation (Table 1).

Table 1. Weight loss of aluminium samples after being in an alcoholic solution of iodine, the surface of which was or wasn't subjected to surface treatment with reactive oxygen species.

	Untreated aluminium sample	Aluminium sample after 4 hours processing	Aluminium sample after 12 hours of processing	Corundum (100 % oxidized aluminium)
Weight loss of aluminium samples %	100 %	70 %	5,5 %	0 %

Thus, experimentally, a dependence of the magnitude of the protective effect of exposure to halogens on the time of exposure to ultraviolet radiation on the surface of aluminium products at 450 °C was found. The protective effect is due to the complete oxidation of a large number of aluminium cells on the surface of the products - the longer the time of exposure to oxygen active forms on the aluminium samples, the more completely oxidised aluminium cells are formed on the surface of the products, the lower the corrosion rate of the aluminium products. If all cells on the surface of aluminium products are completely oxidised (this condition is called corundum), corrosion of the aluminium product in halogen solution stops completely.

4. Conclusions

Thus, it is advisable to create a layer of fully oxidised aluminium cells on the surface of these products for increasing the wear-life of aluminium products in seawater.

1) It has been shown that parametric method 3 of the quantum-chemical calculation can be used to calculate the metals belonging to the first three periods of the Mendeleev table.

2) It has been shown by calculation and experiment that the failure of aluminium products is caused by incomplete oxidation of the surface aluminium cell structure (under normal conditions the rhombic subsystem of the aluminium cells is not oxidised, under fully oxidised cubic sub-system). Insufficient oxidation of aluminum cells leads to destruction of the rhombic subsystem of the cells by negative halogen ions, which are contained in large quantities in seawater. Destruction of rhombic subsystem of aluminium cells occurs because of chemical interaction of negatively charged halogen ions with aluminium atoms of rhombic subsystem: aluminium atoms of fully oxidised cubic subsystem do not enter into chemical interaction with halogen ions. The incomplete oxidation of aluminium cells is due to the lack of energy of oxygen molecules under normal conditions.

3) In order to increase the life span of aluminium products in seawater, it is recommended to create a monolithic corundum layer on the surface of these products (a layer in which all aluminium cells have a fully oxidised rhombic and cubic subsystem): the surface of aluminium products treated with ultraviolet irradiation and heated to 450 °C should be treated for at least 12 hours. It is necessary to create a monolithic layer of fully oxidised aluminium cells at least 1 cell thick on the surface of an aluminium product for achievement a protective effect.

.

Acknowledgments

This scientific article was published as part of the implementation of the scientific program of program-targeted funding for 2021-2023 IRN № BR1090150221 «Development of technology for protective coatings of surfaces of weapons and military equipment to protect against aggressive environmental factors and operating conditions»
(Study is funded by the Science Committee of the Ministry of Education and science of the Republic of Kazakhstan).

REFERENCES

1 Fotovvati B., Namdari N., Dehghanghadikolaei A. On Coating Techniques for Surface Protection: A Review. *J. Manufac. Mat. Proc,* 2019. Vol.3, No.1, pp.28 (1-22). doi:10.3390/jmmp3010028

2 Zolotorevskiy V.S. Experience of develiping and introduction in industry new primary and secondary Al-alloys with given properties for shape casting. *Proceeding of the 13-th Intern.Cnference on aluminum alloys*. Canada, 2013, pp. 343-348. doi: 10.1007/978-3-319-48761-8_53

3 Miracle D.B., Senkov O.N. A critical review of high entropy alloys and related concepts. *Acta Mat*., 2017. Vol.122, pp.448-511. doi: 10.1016/j.actamat.2016.08.081

4 Aboulkhair N.T., Simonelli M., Parry L., et al. 3D printing of Aluminium alloys: Additive Manufacturing of Aluminium alloys using selective laser melting. *Prog. Mat. Sci.,* 2019, Vol. 103, pp. 100578(1-45). doi:10.1016/j.pmatsci.2019.100578

5 Kulagin I., Li M., Laitinen V., et al. Review of MSM Actuators: Applications, Challenges, and Potential. *IEEE Access*, 2022. Vol.10, pp. 83841-83850. doi: 10.1109/ACCESS.2022.3197278

6 George E.P., Curtin W.A., Tasan C.C. High entropy alloys: A focused review of mechanical properties and deformation mechanisms. *Acta Mat.*, 2020. Vol.188, pp. 100578(1-45). doi:10.1016/j.actamat.2019.12.015

7 Tubert-Brohman I., Guimaraes C.R.W., Repasky M.P., et al. Extension of the PDDG/PM3 and PDDG/MNDO semiempirical molecular orbital methods to the halogens. *J. Comp. Chem*., 2004, Vol.25. No.1, pp.138-150. doi: 10.1002/jcc.10356

8 Stewaet J.P. Optimization of parameters for semiempirical methods 2. Applications. *J. Comp. Chem*., 1989. Vol.10, No.2, pp.221-264. doi:10.1002/jcc.540100209

9 Bokiya G.B. *Crystallochemistry.* USSR Academy of Sciences, Institute of Radio Engineering and Electronics. Moscow, 1971, 400 p. [in Russian]

10 Tikhonov V.N. *Analytical Chemistry of Aluminium. Series Analytical Chemistry of Elements*. Moscow, 1971, 266 p. [in Russian]

11 Holleman A.F., Wiberg E. *Inorganic Chemistry*. Academic Press, San Diego, 2001, 1884 p.

12 Gerasimov V.V. *Corrosion of aluminium and its alloys*. Metallurgy, Moscow, 1967, 115 p. [in Russian]

13 Parker K.M., Mitch W.A. Halogen radicals contribute to photooxidation in coastal and estuarine waters. *Proc. Nat. Acad. Scien*., 2016, Vol.113, No.21, pp.5868. doi: 10.1073/pnas.1602595113

14 Encrenaz T., Bibring J.-P., Blanc M., Barucci M.-A., Roques F., Zarka P. *The Solar System*. Springer Science & Business Media, Berlin, 2004, 514 p.

15 Saha K. *The Earth's Atmosphere: Its Physics and Dynamics*. Springer Science & Business Media, Berlin, 2008, 374 p.

16 Watt G.W., Hall J.L., Taylor W.L., Kleinberg J. *Aluminum Iodide*. Synth., 1953. Vol.4. pp. 117–119.

17 Pyzhyanova E.A., Zamyslovsky V.A., Remennikova M.V. Study of singlet oxygen formation in distilled water under the influence of laser radiation with a wavelength of 1.24 μ. *J. Comp. Chem.,* 2018. Vol.5, No.4, pp.297-309. [in Russian]

18 Kotelnikov S.N. Main mechanisms of interaction of ozone with living systems and peculiarities of the surface layer problem for Russia. *Proceedings of the Institute of General Physics named after A.M. Prokhorov.* Russian Academy of Sciences. 2015. Vol.71, No.4, pp.10-41. [in Russian]

Article accepted for publication 25.05.2023

DOI 10.31489/2023No3/27-34

UDC 535.341; 535. 343

OPTICAL PROPERTIES OF CARBON CONTAINING NANOCOMPOSITE FILMS BASED ON THE POLYSTYRENE-FULLERENE C_{60} SYSTEM

Satayeva G.E., Baratova A.A.*, Sakipov K.E., Abdigapar A.A., Sharifov D.M.

L.N. Gumilyov Eurasian National University, Astana, Kazakhstan, aa.baratova@yandex.kz

Carbon-based nanocomposites have attracted significant attention due to their unique properties and potential for use in various technological applications. In this study, experimental investigations were conducted to determine the spectral properties of carbon-containing nanocomposite polymer films based on polystyrene (PS) with fullerene C_{60} nanoadditives. The results indicate that the incorporation of fullerene nanoparticles into the PS matrix enhances the optical properties of the material. Specifically, the optical density of the samples increases, the absorption coefficient increases, and the width of the bandgap decreases with an increase in carbon additive concentration. These findings suggest that fullerene-based nanocomposites are promising materials for optoelectronic and nanotechnological applications. The results of this work contribute to the growing body of research on carbon-based nanocomposites and their potential for use in a range of fields, including electronics, energy storage, and sensing applications. The enhanced optical properties of fullerene-based nanocomposites suggest that they may be particularly useful for developing novel optoelectronic devices and sensors. Overall, this study highlights the potential of fullerene-based nanocomposites as a versatile and promising material platform for various technological applications.

Keywords: nanocomposite polymer films, carbon nanoparticles, fullerene, polystyrene.

1. Introduction

Fullerene-based materials have recently garnered significant attention from researchers due to their extraordinary properties, which make them an intriguing subject for both fundamental research and practical applications [1-10]. These materials have a broad range of potential applications, including hydrogen storage based on fullerenes in the field of energy [11-13]. Furthermore, fullerene-containing materials have the potential to be utilized for converting solar energy, as well as in drug delivery for medicine [14-17]. Fullerenes' distinctive optical and electrical properties may also make them suitable for creating a foundational basis for microelectronics [18-21].

The considerable interest in carbon nanoparticle-modified polymers stems from the fact that such modifications significantly enhance their physical-chemical properties, including optical, mechanical, and catalytic, while also enabling the acquisition of novel properties such as biological activity [22-24]. These novel nanocomposite polymeric materials with improved physicochemical and operational properties are often adopted to complement or replace conventional materials. Of the various high molecular weight compounds, PS exhibits significant non-covalent binding capacity for fullerene [25-28]. Furthermore, styrene and divinylbenzene copolymers serve as raw materials for producing cationites industrially. Consequently, sorption-active carbon nanoparticle-modified composites based on polystyrene can substantially expand the scope of sorbents while also offering new carbon-containing nanocomposite polymeric materials (films) [29-32]. The objective of this research is to investigate how the inclusion of carbon fullerene C_{60} nanoadditives affects the optical characteristics of the PS-C_{60} matrix.

2. Experimental part. Materials and Research Methods

As is known atactic PS is a stiff amorphous polymer with high optical transparency, low mechanical strength, and low density (1060 kg/m^3). It exhibits dielectric characteristics and is a thermoplastic substance that does not crystallize under external factors [33-35]. However, by introducing various foreign impurities of different activity levels, the structure and physical characteristics can be regulated over a wide range. At present, nanocarbon materials, such as fullerenes and their derivatives, are utilized as modifying additives. The research utilized PS grade 143 E (GOST 20282-743) powder and fullerene C_{60} carbon additives, made in Russia, as the study materials. PS and C_{60} were dissolved in toluene at 20°C, after which a C_{60} solution was

.

added to the PS solution at a specific volume fraction to create a polymer solution blend with fullerene concentrations of C=0, 1, 3, 5, and 10% by weight.

The optical properties of the samples were measured on Cary 60 UV-Vis spectrophotometer (Agilent Technologies), scanning in the wavelength range of 190-1100 nm. An impulse xenon lamp with a dual-beam optical scheme and a Cherni-Turner monochromator is used as the source. Two silicon photodiodes serve as detectors for simultaneous measurement of the light beam of the sample and the reference [36,37].

3. Results and discussion

In this work, the experimental investigation results of the optical properties of the PS-C_{60} system are presented. The absorption spectra *A* of polymer nanocomposites with fullerene carbon additives at different concentrations of C_{60} were measured and analyzed (Fig.1). The absorption spectra *A* of the investigated samples were characterized by significant absorption in the short-wavelength region, which decreased rapidly with increasing wavelength at first and then much more slowly for all samples. The presence of fullerene additives C_{60} in PS led to a significant increase in absorption (curves 2-5, Fig.1), and the absorption further increased with increasing C_{60} concentration up to 10%. The transmittance *T* of PS was found to be 50-62% (curve 1, Fig. 2) and decreased with increasing fullerene concentration from 1 to 10% (Fig. 2).

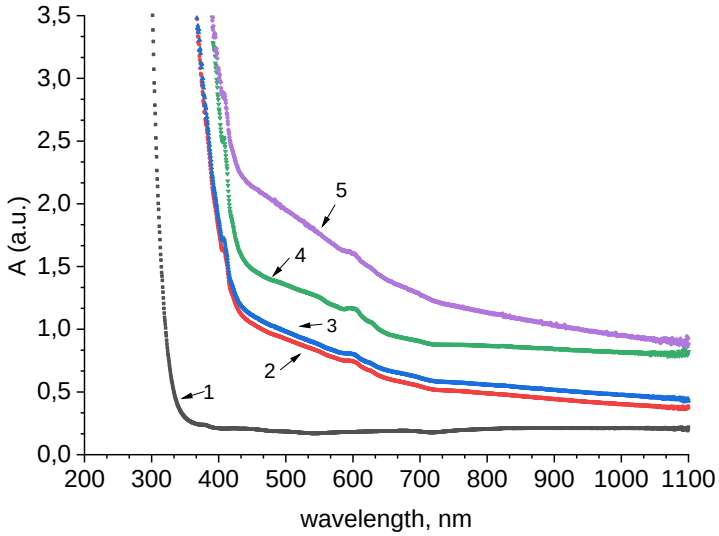

Fig.1. Absorption spectra of PS-C_{60} samples: 1) PS; 2) PS+1% C_{60}; 3) PS+3% C_{60}; 4) PS+5% C_{60}; 5) PS+10% C_{60}.

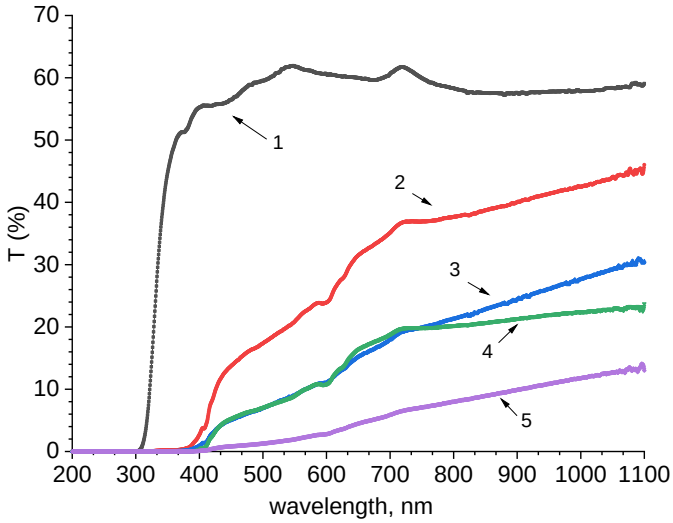

Fig.2. Transmission spectra of PS-C_{60} samples:
1) PS; 2) PS+1% C_{60}; 3) PS+3% C_{60}; 4) PS+5% C_{60}; 5) PS+10% C_{60}.

The dependencies of the reflection spectra R on the wavelength λ for the PS-C_{60} system, presented in Fig. 3, show similar trends to the transmittance spectra T of these samples (Fig. 2), which corresponds to the correlation between the transmittance and reflection of the samples. The value of R for the pure sample is 65-66%, and decreases with increasing concentration of fullerene C_{60}.

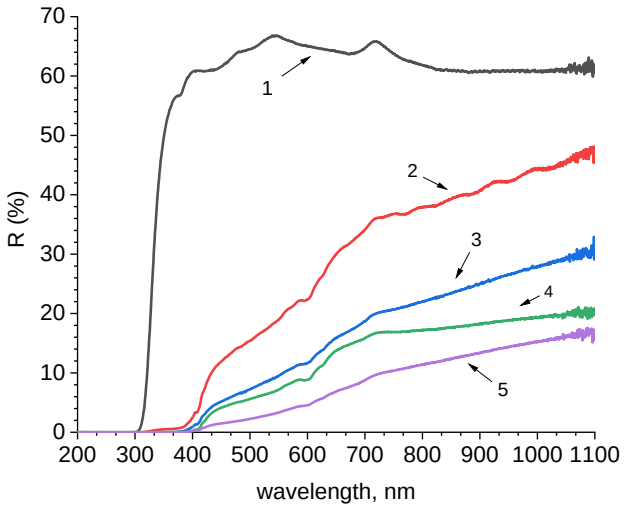

Fig.3. Reflection spectra of PS-C_{60}: 1) PS; 2) PS+1% C_{60}; 3) PS+3% C_{60}; 4) PS+5% C_{60}; 5) PS+10% C_{60}.

Absorption is characterized by the absorption coefficient α, which was calculated using formula:

$$\alpha = 2.303 \cdot \frac{A}{l} \quad (1)$$

where A – absorbtion, l – thickness of the film.

The dependencies of α on the photon energy $h\nu$ at different concentrations are presented in Fig. 4. The value of α gradually increases with increasing photon energy for the pure sample up to energies of 3.56 eV, and then sharply increases. With the addition of C_{60} fullerene to PS, an increase in the absorption coefficient is observed already at energies of approximately 1.13 eV, followed by a region of slight increase in α at energies from 2.02 to 2.11 eV, and at energies of 3.03 eV, a small peak is observed for all C_{60} concentrations (curves 2-5, Fig. 4).

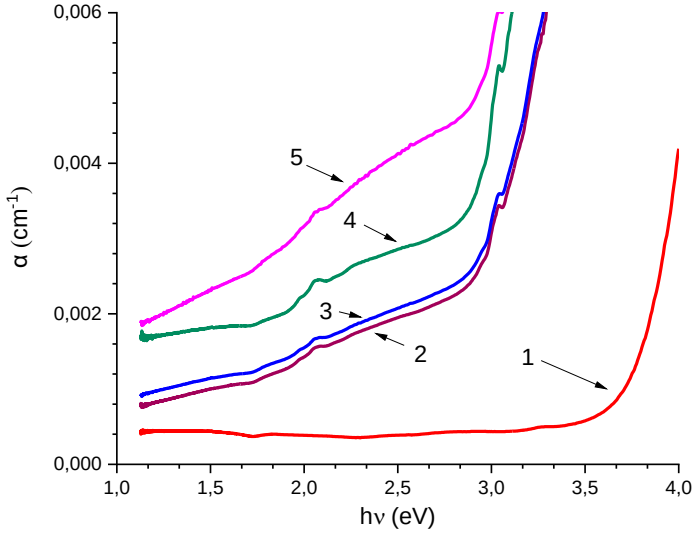

Fig.4. Dependence of the absorption coefficient α on the photon energy $h\nu$ for the PS-C_{60} system at different concentrations of C_{60}: 1) PS; 2) PS+1% C_{60}; 3) PS+3% C_{60}; 4) PS+5% C_{60}; 5) PS+10% C_{60}.

This indicates a change in the optical properties of the investigated samples with increasing photon energy $h\nu$ and depending on the concentration of fullerene C_{60}. The optical conductivity σ_{opt} of the PS-C_{60} system was also calculated:

$$\sigma_{opt} = \frac{\alpha n c}{4\pi} \tag{2}$$

where c is the speed of light, n – refractive index.

The graphs of the dependencies of σ_{opt} are shown in Fig. 5. For the PS (curve 1, Fig. 5), the optical conductivity σ_{opt} hardly changes with the increase in $h\nu$ energy. However, the addition of fullerene nanoadditives leads to an increase in σ_{opt} with the increase in photon energy even at low concentrations of C_{60} from (0.524 - 6.696) × 10^9 s^{-1}. A sharp increase in optical conductivity is observed with an increase in the fraction of fullerene (10%) in the PS matrix (curve 5, Fig. 5). This indicates that the addition of fullerene to the PS matrix promotes the enhancement of the optical properties of the PS matrix, namely the optical conductivity.

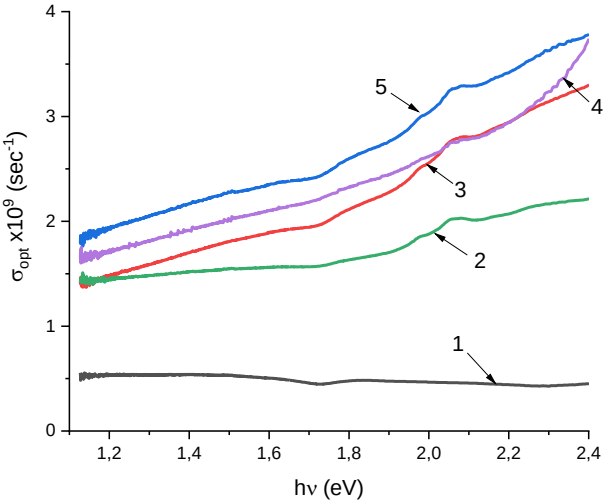

Fig.5. Dependencies of optical conductivity σ_{opt} on the photon energy $h\nu$ for the PS-C_{60} system at different concentrations of C_{60}: 1) PS; 2) PS+1% C_{60}; 3) PS+3% C_{60}; 4) PS+5% C_{60}; 5) PS+10% C_{60}.

To assess the influence of fullerene C_{60} additives on changes in the optical properties of the PS matrix, the absorption edges were determined by extrapolating the steep portions of the curves for the absorption coefficient α (Fig. 6) to the intersection with the x-axis at a certain point. The position of the intersection point gives the value of the optical band edge.

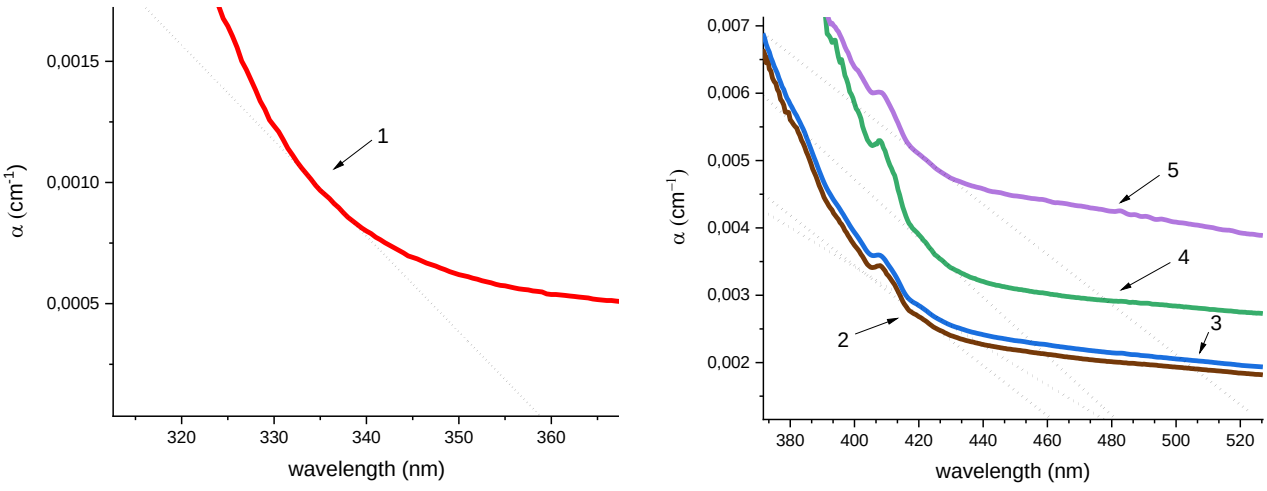

a) b)

Fig.6. Extrapolation of the dependencies of the absorption coefficient α on the photon energy $h\nu$: a): 1) PS; b): 2) PS+1% C_{60}; 3) PS+3% C_{60}; 4) PS+5% C_{60}; 5) PS+10% C_{60}.

The addition of C_{60} fullerene nanoparticles to the PS matrix causes a redshift in the absorption edge, which means that the absorption of light shifts towards longer wavelengths. The intersection points of the curves with the x-axis (as shown in Fig. 6) indicate the position of the absorption edge, which was found to shift towards longer wavelengths with increasing concentration of C_{60} in the PS matrix. The shift in the absorption edge was found to increase from 358 nm for the pure PS sample to 526 nm for the PS+10% C_{60} sample. Material's optical energy band gap E_g is related to its absorption coefficient α and the energy of the incident photon $h\nu$ according to the following equation:

$$(\alpha h\nu)^m = B(h\nu - E_g) \tag{3}$$

where h is the Planck constant, ν is the frequency of the incident radiation, and B and m are constants. The value of m depends on the type of transition between the valence band and the conduction band of the material. The constant m takes on values of 2, 3, 1/2, or 3/2 for allowed direct, forbidden direct, allowed indirect, or forbidden indirect transitions, respectively. Analysis of the absorption spectra of the investigated samples showed that the PS-C_{60} system allows for allowed direct transitions, so the value of m=2 was used in formula (3) to determine the width of the optical band gap E_g. The values of E_g for pure PS and PS with C_{60} fullerene additives at concentrations of 1%, 3%, 5%, and 10% were obtained by extrapolating the linear portions of the $(\alpha h\nu)^2$ curves to the $h\nu$ axis until they intersect with the x-axis. The point of intersection of the curve with the x-axis allows for the determination of E_g (Fig. 7).

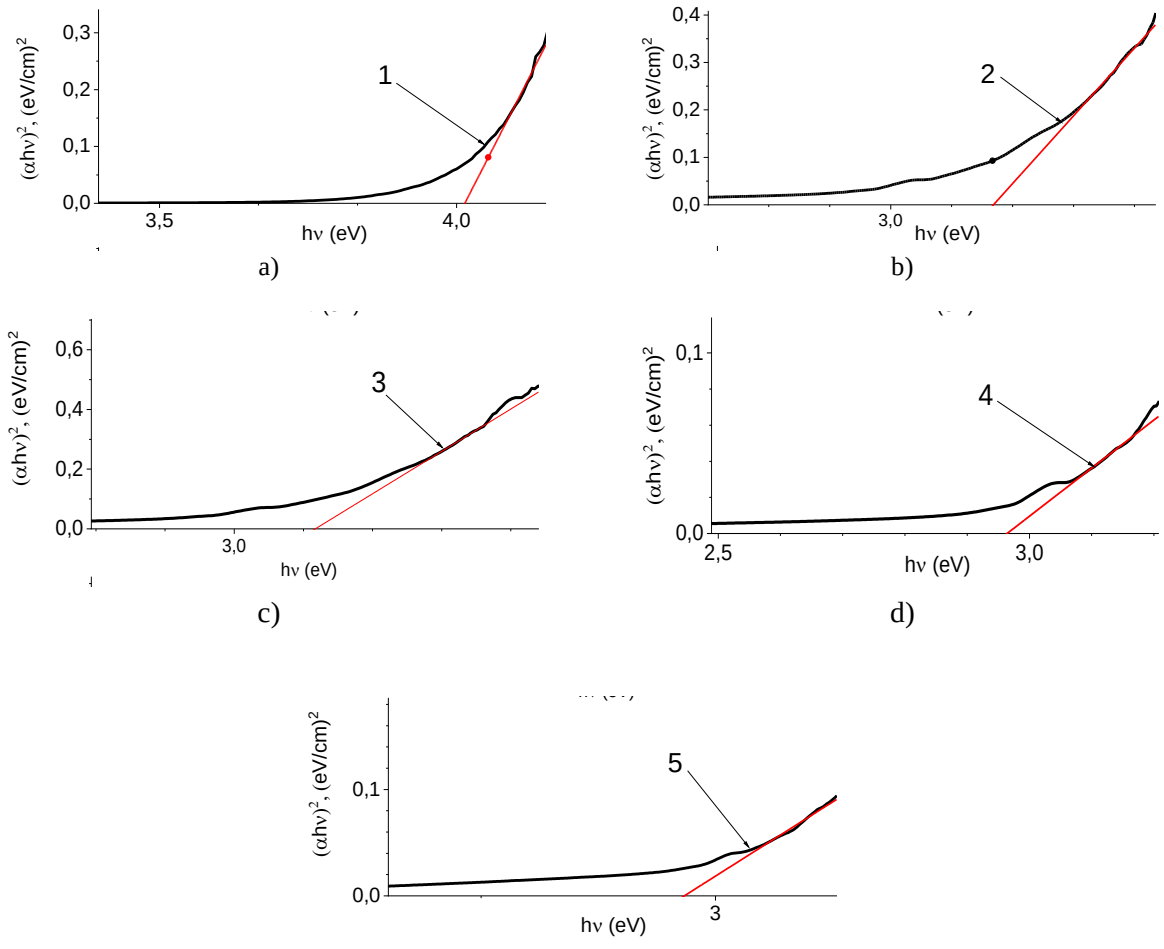

Fig.7. Dependence of $(\alpha h\nu)^2$ on $h\nu$ for the studied samples:
1) PS; 2) PS+1% C_{60}; 3) PS+3% C_{60}; 4) PS+5% C_{60}; 5) PS+10% C_{60}.

For clarity, all graphs for pure PS and PS with different concentrations of C_{60} fullerene are presented separately in Fig. 7. The trend of decreasing E_g with increasing percentage of C_{60} fullerene in the PS-C_{60} matrix is clearly visible in Fig. 8, and the addition of just 1% C_{60} leads to a sharp decrease in E_g from 3.972 eV to 1.854 eV (Fig. 8). In other words, increasing the concentration of C_{60} fullerene in the PS matrix leads to a decrease in the width of the optical band gap, which is consistent with the values for the absorption edge wavelength presented in Table 2, where an increase in wavelength is observed with increasing concentration of C_{60} in PS.

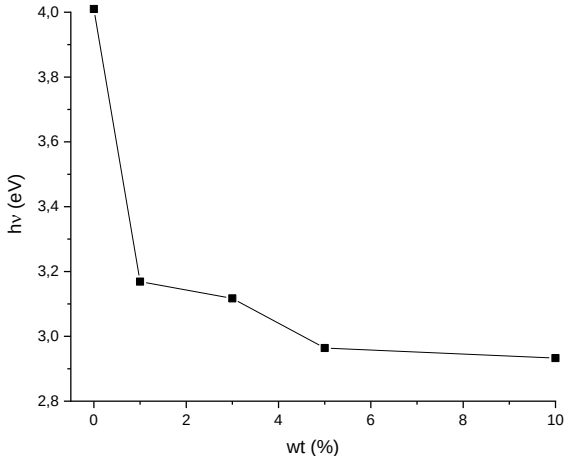

Fig. 8. Dependence of the width of band gap energy E_g on the concentration of fullerene C_{60} in the PS matrix.

Table 2. Values of the optical band gap energy (E_g) for different PS-C_{60} samples, determined from the wavelength of the absorption edge.

Sample	Wavelength of the absorption edge, nm	E_g, eV
PS	358	3.972
PS+1% C_{60}	461	2.092
PS+3% C_{60}	477	2.039
PS+5% C_{60}	481	3.028
PS+10% C_{60}	526	1.854

The decrease in E_g value in PS indicates that the incorporation of C_{60} nanoparticles in PS leads to a weakening of its dielectric properties and acquisition of semiconductor properties by the matrix. This phenomenon may also be related to the formation of defects in the polymer matrix, which can lead to the creation of localized sub-levels in the optical band gap and, as a result, to a decrease in the energy width of the band gap.

4. Conclusion

The work has shown that the incorporation of carbon-containing nanocomposite additives of fullerene C_{60} at different concentrations into the polystyrene matrix leads to changes in the optical properties of the matrix. The main optical parameters of the PS polymer films doped with fullerene C_{60} were determined. The values of the optical energy band gap (E_g) of the prepared PS-C_{60} polymer films demonstrate a tendency to decrease with increasing fullerene concentration.

The obtained research results allow suggesting that fullerene C_{60} nanoaditives, as promising modifying additives improving the physical and mechanical properties of composite materials, when introduced into polymer materials, allow giving them unique properties and making it possible to create new demanded materials. Such materials can be used in the field of improving the operational characteristics of various materials based on them, in solar elements, as well as for the development of components of new electronic devices.

References

1. Etman M., Bedewy M.K., Khalil H.A., Azzam B.S. Carbon nanotubes reinforced polymer matrix nanocomposites. *International Journal of Nanoparticles,* 2009, Vol.2, No. 1/2/3/4/5/6, pp. 339 – 353. doi:10.1504/IJNP.2009.028768
2. Annu A., Singh A., Singh P.K., Bhattacharya B. Effect of carbon nanotubes as dispersoid in polymer electrolyte matrix. *Journal of Material Science: Materials in Electronics,* 2018, Vol. 2, No. 11. doi:10.1007/s10854-018-9008-1
3. Liu C.X., Choi J.W. Improved Dispersion of Carbon Nanotubes in Polymer at High Concentrations. *Nanomaterials,* 2012, Vol 2, No. 4, pp. 329 – 347. doi:10.3390/nano2040329
4. Akter T., Barile C., Ahammad A.J.S. Introduction, and overview of carbon nanomaterial-based sensors for sustainable response. *Carbon Nanomaterials-Based Sensors,* 2022, Vol. 2, No. 23, pp. 395 – 416. doi:10.1016/B978-0-323-91174-0.00018-4
5. Nassrollahzadeh M., Sajadi S.M., Sajjadi M., Issaabadi Z. Nanomaterails and nanotechnology-associated innovations against viral infections with a focus on coronaviruses. *Interface Science and Technology, 2019, Vol.* 28, pp. 1-27. doi:10.1016/B978-0-12-813586-0.00001-8
6. Yellampalli S. *Carbon Nanotubes-Polymer, Nanosomposites*. Rijeka, Croatia, 2011, 410 p.
7. El-Nahass M. M., Ali H. A. M., Gadallah A. S., Atta Khedr M., Afify H. A. Analysis of structural and optical properties of annealed fullerene thin films. *The European Physical Journal D,* 2015, Vol. 69:200. doi:10.1140/epjd/e2015-60174-8
8. Aziz S.B., Ahmed H.M., Hussein A.M., Fathulla A.B., Wsw R.M., Hussein R.T. Tunning the absorption of ultraviolet spectra and optical parameters of aluminum doped PVA based solid polymer composites. *J. Mater. Sci. Mater. Electron,* 2015, Vol. 26, pp. 8022-8028. doi:10.12691/pmc-3-2-1
9. Grazulevicius J.V., Strohriegl P., Pielichowski J., Pielichowski K. Carbazole-containing polymers: synthesis, properties, and applications. *Progress in Polymer Science,* 2003, Vol. 28, No 9, pp. 1297 – 1353. doi:10.1016/s0079-6700(03)00036-4
10. Hassanien A.M., Atta A.A., Ward A.A., Ahmed E.M. Investigation of structural, electrical and optical properties of chitosan/fullerene composites. *Materials Research Express,* 2019, Vol. 6, No 12. doi: 10.1088/2053-1591/ab5295
11. Gao Y., Wu X., Zeng X.C. Designs of fullerene-based frameworks for hydrogen storage. *J. Mater. Chem. A.* 2014, Vol. 2, pp. 5910-5914. doi:10.1039/C3TA13426A
12. Züttel A. First principles investigation of energetics and electronic structures of Ni and Sc Co-Doped MgH_2. *Materials for Hydrogen Storage. Mater. Today*, 2003, Vol. 6, No. 9, pp. 24-33. doi:10.1016/S1369-7021(03)00922-2
13. Vasil'ev Y.V., Hirsch A., Taylor R., Drewello T. Hydrogen on fullerenes: hydrogenation of $C_{59}N$. using C60H36 as the source of hydrogen. *Chem. Communications*, 2004, Vol. 15, pp. 1752-1753. doi:10.1039/b405353m
14. Lo S. C., Burn P.L. Development of dendrimers: macromolecules for use in organic light emitting diode and solar cells. *Chemical. Reviews,* 2007, Vol. 107, pp. 1097 - 1116. doi:10.1021/cr050136l,
15. Taylor R., Drewello T. Hydrogen on fullerenes: hydrogenation of $C_{59}N$. using $C_{60}H_{36}$ as the source of hydrogen. *Chem. Communications*, 2004, Vol. 15, pp. 1752-1753. doi:10.1039/b405353m
16. Katz E.U. Potential of fullerene-based materials for the utilization of solar energy. *Physics of the Solid State,* 2002, Vol. 44, No. 4, pp. 647-651. doi: 10.1134/1.1470549
17. Yang X., Ebrahimi A., Li J., Cui Q. Fullerene-biomolecule conjugates and their biomedicinal applications. *International Journal Nanomedicine,* 2014,Vol. 9, No 1, pp. 77 - 92. doi:10.2147/IJN.S52829
18. Tanzi L., Terrenzi M., Zhang Y. Sythesis and biological application of glycol- and peptide derivatives of fullerene C_{60}. *European Journal of Medicinal Chemistry,* 2022, Vol. 230. doi:10.1016/j.ejmech.2022.114104
19. Sun H.T, Sakka Y. Luminescent metal nanoclusters: controlled synthesis and functional applications. *Sci Technol Adv Mater*., 2013, Vol. 15, No.1. doi:10.1088/1468-6996/15/1/014205
20. Kanel S.R., Nadagouda M.N., Nakarmi A., Malakar A., Ray C., Pokhrel L.R. Assessment of health, afety, and economics of surface modified nanomaterials for catalyc applications. *Surface Modified Nanomaterials for Applications in Catalysis*, 2022, Vol. 22, pp. 289-317. doi:10.1016/B978-0-12-823386-3.00009-X

.

21. Ramazani A., Moghaddasi M.A., Malekzhadeh A. M, Rezayati S., Hanifehpour Y., Joo S.W. Industrial oriented approach on fullerene preparation methods. *Inorganic Chemistry Communications*, 2021, Vol. 125, p.108442. doi:/10.1016/j.inoche.2021.108442

22. Ghavanloo E., Rafii-Tabar H., Kausar A., Giannopoulos G.I., Fazelzadeh S.A. Experimental and computational physics of fulerenes and their nanocomosites: synthesis, thermo-mechanical characteristics and nanomedicine applications. *Physics Reports,* 2023, Vol. 996, pp. 1 - 116. doi:10.1016/j.physrep.2022.10.003

23. Nieto-Márquez A., Romero R., Romero A., Valverde J. L. Carbon nanospheres: synthesis, physicochemical properties and applications. *Journal of Materials Chemistry*, 2011, Vol. 21, pp. 1664 - 1672. doi: 10.1039/C0JM01350A

24. Mugadza K., Stark A., Ndungu P.G., Nyamori V.O. Synthesis of carbon nanomaterials from biomass utilizing ionic liquids for potential application in solar energy conversion and storage. *Materials,* 2020, Vol. 13, No. 18. doi:10.3390/ma13183945

25. Zaytseva O., Neumann G. Carbon nanomaterials: production, impact on plant development, agricultural and environmental applications. *Chemical and Biological Technologies in Agriculture*, 2016, Vol. 3, No. 17. doi:10.1186/s40538-016-0070-8

26. Biglova Y.N., Mustafin A.G. Nucleophilic cyclopropanation of [60] fullerene by the addition-elimination mechanism. *RSC Advances*, 2019, Vol. 9, pp. 22428-22498. doi:10.1039/C9RA04036F

27. Torres F. J., Civalleri B., Pisani C., Musto P., Albunia A.R., Guerra G. Normal vibrational analysis of a trans-planar syndiotactic polysterene-chain. *Journal Phys. Chem. B,* 2007, Vol. 111, pp. 6327 - 6335. doi:10.1021/jp072257q

28. Basiuk V.A., Kolokoltsev Y., Amelines-Sarria O. Noncovalent interaction of meso-tetraphenylprophine with C_{60} fullerene as studied by several DFT methods. *Journal of Nanoscience and Nanotechnology*, 2011, Vol. 11, No.6, pp. 5519 - 5525. doi:10.1166/jnn.2011.3442

29. Kausar A., Taheran R. Electrical conductivity behavior of polymer nanocomposite with carbon nanofillers. *Electrical Conductivity in Polymer-Based Composites*, 2019, Vol. 3, pp. 41-72. doi:10.1016/B978-0-12-812541-0.00003-3

30. Zemtsova E.G., Arbenin A.Yu., Sidorov Y.V., Morozov N.F., Korusenko P.M., Semenov B.N., Smirnov V.M. The use of crbon-containing compounds to prepare functional and structural composite materials. *Applied Sciences*, 2022, Vol. 12(19). doi:10.3390/APP12199945

31. Sanz A., Wong H.C., Nedoma A. J., Douglas J. F., Cabral J. T. Influence of C60 fullerenes on the glass formation of polystyrene. *Polymer,* 2015, Vol. 68, pp. 47-56. doi: 10.1016/j.polymer.2015.05.001

32. Krishnamoorti R., Vaia R.A. Polymer nanocomposites. *Journal of Polymer Science Part B: Polymer Physics*, 2007, Vo.45, No. 24, pp. 3252 - 3256. doi:10.1002/polb.21319

33. Wong H.C., Cabral J. T. Domain orientation and grain coarsening in cylinder-forming polysterene-b-methyl methalcrylate films. *Macromolecules,* 2011, Vol. 44, No. 11, pp. 4530-4537. doi:10.1021/ma2004458

34. Blazejczyk A., Jastrzebski C., Wierzbicki M. Change in conductive-radiative heat transfer mechanism forced by graphite microfiller in expanded polysterene thermal insulation-experimental and simulated investigations. *Materials*, 2020, Vol. 13, No. 11. doi:10.3390/ma13112626

35. Kajiyama T., Tanaka K., Satomi N., Takahara A. Surface glass transition temperatures of monodisperse polysterene films by scanning force microscopy. *Science and Technology of Advanced Materials*, 2000, Vol.1, No.1. pp. 31-35. doi:10.1016/S1468-6996(99)00005-4

36. Harris P.J.F. Fullerene Polymers: a brief review. Carbon-Rich Compounds: From Molecules to Materials, 2020, Vol. 6, No.4. doi:10.3390/c6040071

37. Satayeva G.E., Bekmukhanbetova D.B., Amangeldy N., Yergaliuly G. *Research of Nanomaterials by the Spectroscopy Methods.* Astana, L.N. Gumilyov Eurasian National University, 2022, 108 p.

Article accepted for publication 12.06.2023

DOI 10.31489/2023No3/35-42

UDC 539.3/.6; 621.315.592

PROCESSES OF DEFECT FORMATION IN SILICON DIFFUSIONALLY DOPED WITH PLATINUM AND IRRADIATED WITH PROTONS

Utamuradova Sh.B. [1], Daliev Sh.Kh.[1], Rakhmanov D.A.[1*], Doroshkevich A.S.[2], Genov I.G.[2,3], Tuan P.L.[2,4], Kirillov A.K.[2]

[1] Institute of Semiconductor Physics and Microelectronics, National University of Uzbekistan named after Mirzo Ulugbek, Tashkent, Uzbekistan, dilmurod-1991@bk.ru

[2] Joint Institute for Nuclear Research, Dubna, Russia

[3] Institute of Electrochemistry and Energy Systems "Acad. Evgeni Budevski"- Bulgarian Academy of Sciences, Sofia, Bulgaria

[4] Hanoi Irradiation Center, Vietnam Atomic Energy Institute, Hanoi, Vietnam

In this work, we studied the effect of technological regimes and proton implantation on the processes of defect formation in single-crystal n-type silicon (n-Si) doped with platinum using the method of impedance spectroscopy. It has been established that radiation-induced changes in the electrical conductivity of silicon depend significantly on the technological regimes of doping with impurities in silicon. Hodographs show that doping with platinum leads to a decrease in the electrical resistance of silicon samples. Irradiation with 2 MeV protons at a dose of 5.1 × 10^{14} particles / cm^2 leads to a significant (2-3 times) increase in the electrical resistance of the silicon samples under study. It is concluded that the relatively high resistance to radiation exposure (resistance change of no more than 16%: from 55 kΩ to 65 kΩ as a result of ion implantation) of samples doped at 1200°C is presumably due to a higher concentration of impurity ions (platinum) in the samples volume compared to 1100°C.

Keywords: silicon, platinum, doping, high-temperature diffusion, proton irradiation.

1. Introduction

Modeling, synthesis and research of new functional materials are among the most urgent scientific problems of our time. The microstructure and isovalent impurities determine the functional properties of materials of this class. That is why the study of the electrical properties of semiconductors and semiconductor structures, taking into account their real microstructure, is an important and urgent task [1-4]. New materials based on silicon, in particular, those containing platinum (n-Si<Pt>) as a dopant (n-type conductivity), have not been studied enough and are of interest for fundamental science and practical applications.

Modification of the properties of semiconductor materials by beams of light ions, in particular, protons, is one of the most promising and actively developing physical and technological methods in recent years [5,6]. Interest in the implantation of protons in silicon crystals is due to a wide and controllable range of processed depths (from 0.1 μm to 1 mm) and the absence of complex radiation complexes with a high annealing temperature after irradiation. The main three factors affecting the change in the properties of semiconductors after proton irradiation are: a change in the electrical properties of semiconductors, radiation defect formation, and the accumulation of hydrogen atoms [7,8].

The purpose of this work is to study the effect of technological regimes and proton implantation on the processes of defect formation in single-crystal n-Si<Pt> using impedance spectroscopy.

Electrochemical impedance spectroscopy (EIS) is one of the most informative methods for the electrochemical study of materials due to its unique ability to separate the kinetics of various stages occurring in electrochemical processes. Impedance measurements are performed over a wide frequency range (about nine decades), which makes it possible to observe processes with a large difference in time constants. EIS can be used to isolate and evaluate electronic and ionic conductivities, fast electrochemical kinetics, diffusion and other transport restrictions, as well as the formation and development of new phases [9].

.

2. Materials and methods

The objects under study were n-type silicon wafers 1.5 x 6 x 13 mm in size with a resistivity of 40 Ω cm (KEF-40 grade). The wafers were cut from silicon ingots grown by the Czochralski method. Diffusion doping of silicon with platinum was carried out from a layer of metallic Pt deposited on the silicon surface in evacuated quartz ampoules at temperatures of 1100 and 1200 °C for 2 hours. Subsequent cooling of the samples was carried out using the thermal regimes given in [10–12]. The phosphorus dopant concentration in the initial n-Si samples was 4.2×10^{14} at/cm^3.

After thorough cleaning of the surface, the doped samples were irradiated with protons with an energy of 2 MeV, at a current of 0.5 μA to obtain a dose of 5.1×10^{14} particles / cm^2 using an electrostatic accelerator "EG-5" in the Laboratory of Neutron Physics of the Joint Institute for Nuclear Research (FLNP JINR).

The study of the EIS of silicon samples was carried out at room temperature (300°K) on an impedancemeter "Sp-200 BioLogic" in the frequency range of 1 Hz ÷ 1 MHz at an excitation signal voltage of 10 mV. Overhead electrodes were made of copper foil, the clamping was carried out using a foam sponge. In our representation of a contour with distributed parameters, these parameters were calculated according to the expression:

$$\tau_f = R_1 P_1,\ \tau_d = (R_1)^2/(2W_{sr1}{}^2) \quad (1)$$

The optical properties of the surface of the samples were studied using an ELLIPS-1991 spectroscopic ellipsometer at room temperature. The measurements were carried out in the wavelength range 350 ÷ 1000 nm with a step of 2 nm, the angle of incidence of the light beam was 70°. The elemental composition of silicon samples was determined by X-ray spectral microanalysis using a scanning electron microscope (SEM).

3. Results and discussion

On figure 1 shows the impedance hodographs of an undoped n-Si sample before and after irradiation (hereinafter referred to as “initial”).

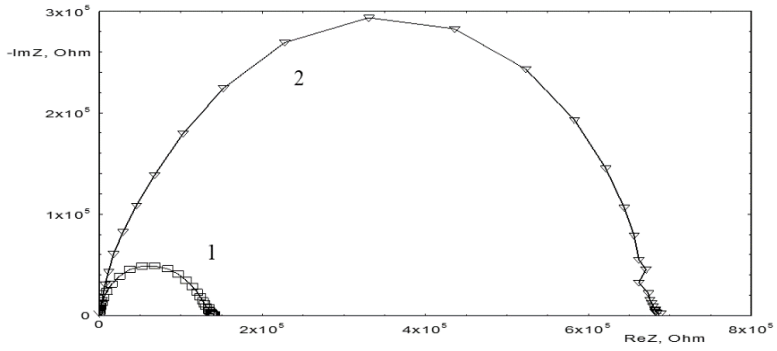

Fig.1. Hodographs of the original n-Si sample. before (1) and after (2) irradiation.

The impedance spectrum (Fig. 1, 1-curve) is in the resistance range 93Ω÷ 128.7 kΩ and has the shape of an arc of a circle, which is typical for the electrode reaction. The section of the diagram in the range from 0 ÷ 93 Ω along the X axis corresponds to the resistance of the electrolyte [13,14].

The impedance spectrum of the irradiated sample (Fig. 1, curve 2) has a similar shape and is in the range 248 Ω ÷ 673 kΩ. It can be seen that irradiation in this case led to an increase (by almost a factor of 5) in the resistance of the sample, presumably due to the formation of defects in the crystal lattice [15,16].

On figure 2 shows the impedance curves of the n-Si samples doped with Pt at a temperature of 1100°C for 2 hours before and after irradiation. A curve in the form of an arc of a circle is observed in the range of ohmic resistance values up to 99.42 kΩ. Irradiation leads to an increase in ohmic resistance at least 4 times (up to 422 kΩ, Fig. 2. 2-curve).

The hodograph of fig.2, as in the case of fig.1, can be described by one equivalent electrical circuit (fig.3). It should be noted that the scatter of points in the low-frequency region is relatively small, compared

to the unirradiated sample, which indicates a relatively high homogeneity of the conduction channels after irradiation, which is in good agreement with the literature data [17]. The most significant factor of radiation exposure is radiation defect formation, in particular, the formation of vacancies. Among such defects, one should first of all include oxygen vacancies Oi - vacancy V (A-center), divacancies (V-V) and the boron complex P_S (at the site) - vacancy V (E-center).

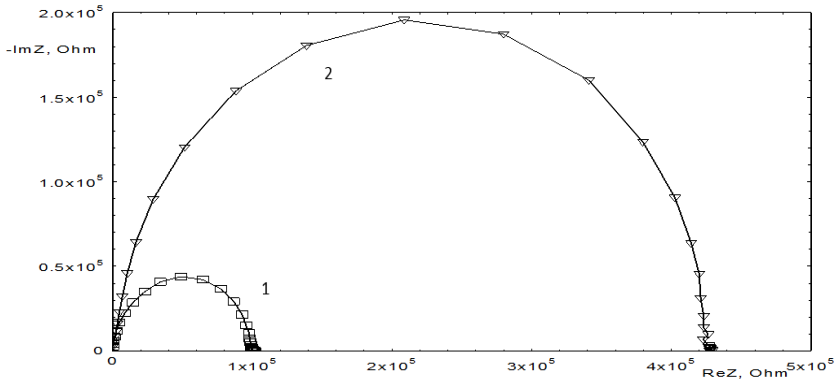

Fig. 2. Hodographs of the I-batch of n-Si samples doped with Pt before (1) and after (2) irradiation. T_{diff}=1100 ºC, t_{diff} =2 hours.

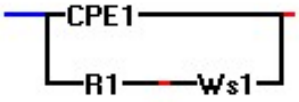

Fig.3. Equivalent electrical circuit, where R_1 is active resistance; CPE - constant phase element; Ws_1 is the "final" Warburg element characterizing the diffusion properties of the sample.

On figure 4 shows the impedance hodographs of the n-Si sample doped with platinum (t_{diff} = 2 h, T_{diff} = 1200°C) before and after irradiation. On fig. 4 (curve 1) there is a semicircle with a limiting ohmic resistance of 55 kΩ. Consequently, doping led to a decrease in the ohmic resistance of the sample by almost 2 times. It can be seen (Fig. 4, curve 2) that irradiation with protons leads to an increase in the resistance value from 55 kΩ to 65 kΩ.

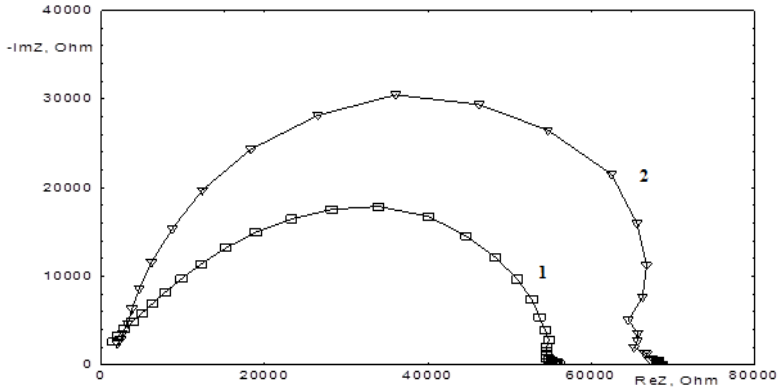

Fig. 4. Hodographs II - batch of samples of n-Si doped with Pt before (1) and after (2) irradiation. T_{diff}=1200ºC, $t_{diff.}$ =2 hours.

Analysis of the obtained results showed that the slope of the hodograph (Fig. 4, curve 1) of the unirradiated sample at high frequencies is 39°, i.e. a linear diffusion process occurs in a homogeneous layer with a slight deviation from Fick's second law [18]. After irradiation of the samples (Fig. 4, 2-line), the slope increases to 65.45°, i.e. diffusion limitations appear, which are probably associated with a violation of the homogeneity of the material. The obtained results showed that irradiation of n-Si<Pt> samples by protons with an energy of 2 MeV with a dose of 5.1×10^{14} particles / cm^2 leads to a significant increase (2-3 times) in the electrical resistance of the silicon samples under study. Moreover, the observed effect largely depends on the doping temperature (Table 1).

.

Table 1. Limiting values of ohmic resistance of Si samples doped with Pt at 1100°C and 1200°C before and after proton irradiation.

	Sample resistance [kΩ]		
	n-Si	n-Si<Pt> 1100 °C	n-Si<Pt> 1200 °C
Before irradiation	129	99	55
After irradiation	673	422	65

The results of measurements of the impedance of the studied samples showed that there is a linear decrease in electrical resistance, starting from a frequency of 1000 Hz. Up to a frequency of 1000 Hz, the electrical resistance remains almost unchanged. Table 2 below shows the values of the active resistance of the equivalent circuit described by the Rendlis circuit [19]. These values also undergo changes after doping and irradiation, in particular, after doping - decreases, after irradiation - increases (Table 2).

The frequency dependence of the Randlis contour can be expressed in terms of two time constants for the Faraday (τ_f) and diffusion (τ_d) processes [19]:

$$\tau_f = R_{ct}C_{dl}\,,\ \tau_d = (R_{ct})^2/(2W_{sr}^2) \qquad (2)$$

The relatively high resistance to radiation exposure (resistance change of no more than 16%: from 55 kΩ to 65 kΩ as a result of ion implantation) of samples doped at 1200°C is presumably due to a higher concentration of impurity ions (platinum) in the sample volume compared to 1100°C (the coefficient of diffusion of platinum at 1200°C is almost 3 times higher than at 1100°C) [20,21].

Table 2. Summary table for the variant of EEC approximation by the Randlis contour with distributed parameters.

Options	n-Si	n-Si (irradiated)	n-Si<Pt> (1100 ^{0}C)	n-Si<Pt> (1100 ^{0}C, irradiated)	n-Si<Pt> (1200 ^{0}C)	n-Si<Pt> (1200 ^{0}C, irradiated)
R_1	1.0414×10^{5}	4.6704×10^{5}	98320	4.3122×10^{5}	22513	25789
P_1	2.8859×10^{-10}	4.6399×10^{-10}	1.4253×10^{-10}	1.9715×10^{-10}	4.143×10^{-09}	3.7722×10^{-10}
n_1	0.9345	0.88054	0.94156	0.91684	0.71875	0.90322
Wsr1	1.3446×10^{6}	1.8216×10^{7}	5.7689×10^{6}	9.8787×10^{6}	4.5293×10^{6}	9.5534×10^{6}
Wsc1	0.016903	0.0084157	0.00015914	1.2457×10^{-10}	0.0051843	0.0030387
$\tau_F = R_1\cdot P_1$, c	3.0×10^{-5}	2.2×10^{-4}	1.4×10^{-5}	8.5×10^{-5}	9.3×10^{-5}	9.7×10^{-6}
τ_D, c	3.0×10^{-3}	3.3×10^{-4}	1.4×10^{-4}	9.5×10^{-4}	1.2×10^{-5}	3.6×10^{-6}

The presence of platinum in single crystals is confirmed by X-ray spectral analysis (Fig. 5), and is 3.04 at. % or 8.74 wt.%. for samples doped at 1100°C (Fig. 5a) and 7.38 at. % or 15.48 wt.%. for samples doped at 1200°C (Fig. 5b).

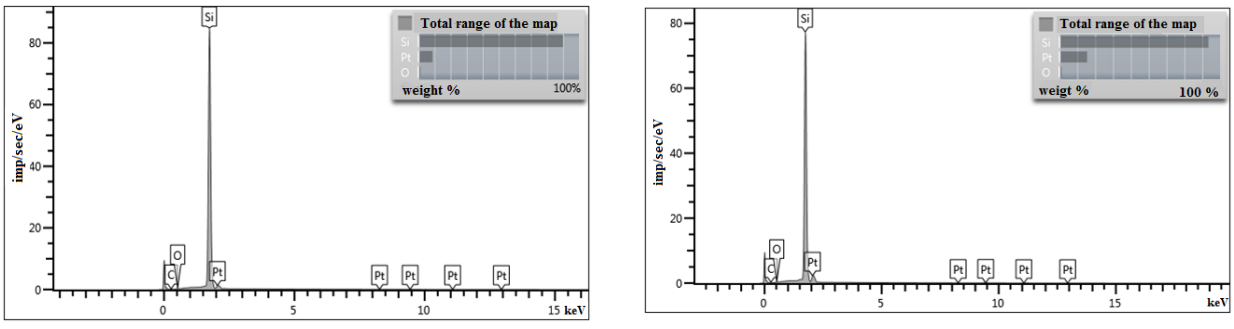

a) b)

Fig. 5. Energy-dispersive spectra of silicon samples doped with platinum at 1100 °C (a) and 1200 °C (b).

The energy-dispersive spectra presented in Figure 5 indicate the presence in the composition of the studied samples, in addition to platinum, oxygen and carbon atoms in a small percentage concentration. Additional experiments were carried out using ellipsometric spectroscopy and the optical parameters of various layers formed on the surface of doped samples were determined. Ellipsometry measures the change in polarization when light is reflected or transmitted from a material structure. The change in polarization is represented as the ratio of the amplitudes Ψ and the phase difference Δ. The measured response depends on the optical properties and thickness of the individual materials. Figure 6 shows the Ψ- and Δ-spectra of the initial, doped and irradiated samples.

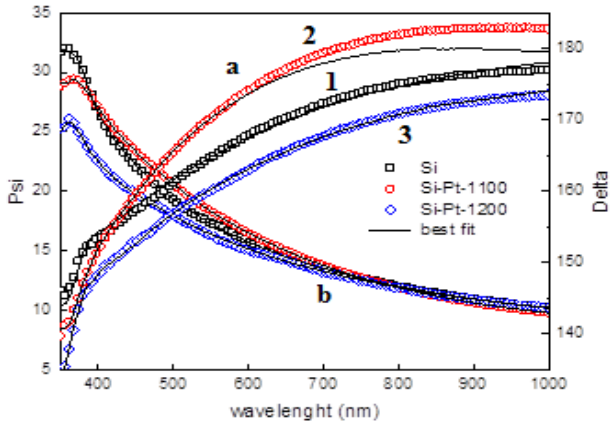

Fig.6. Ψ-spectra (a) and Δ-spectra (b) of samples: 1 - original, 2 - doped with platinum at 1100 °C and 3 - doped with platinum at 1200 °C. the black line is the best fit curve.

It was found that only an oxide layer with a thickness of 5.37 nm was observed in the initial samples (Table 3). After doping with platinum atoms at 1100°C, in addition to the oxide layer, a diffusion layer 21 nm thick appears on the surface of the samples, and the thickness of the oxide layer increased to 10.86 nm. Doping with platinum at a temperature of 1200°C leads to the appearance of a diffusion layer 30.4 nm thick and a decrease in the oxide layer by 8.98 nm (Table 3).

Table. 3. Parameters of oxide and diffusion layers on the surface of silicon samples.

No	Samples	Thickness (nm)	
		Native oxide layer	Diffusion layer
1	Si	5.3772	0
2	Si-Pt-1100°	10.86	21
3	Si-Pt-1200°	8.9791	30.4

It is known that a natural oxide layer is formed on the surface of semiconductor materials in an oxygen atmosphere [22]. Therefore, in the three-layer model used to explain the results of ellipsometric spectroscopy measurements, the natural oxide layer is always taken into account. A three-layer model was used in the calculations, including a natural oxide layer, a diffusion layer, and a crystalline silicon substrate [23]. For the natural oxide layer, the dispersion model of Cauchy and Urbach was used (Fig. 7), and for the diffusion layer of the samples, the parametric Si model was used (Fig. 8).

The dispersion models of Cauchy and Urbach give the following dependence of the refractive index n(λ) and the extinction coefficient k(λ) on the light wavelength λ(nm), respectively [24]:

$$n(\lambda) = A + \frac{B}{\lambda^2} + \frac{C}{\lambda^4} + \cdots \quad (3)$$

$$k(\lambda) = \alpha e^{\beta\left(1240\left(\frac{1}{\lambda} - \frac{1}{\gamma}\right)\right)} \quad (4)$$

where A, B, C are the Cauchy coefficients, α is the amplitude of the extinction coefficient, β is the exponential factor, and γ is the band edge.

.

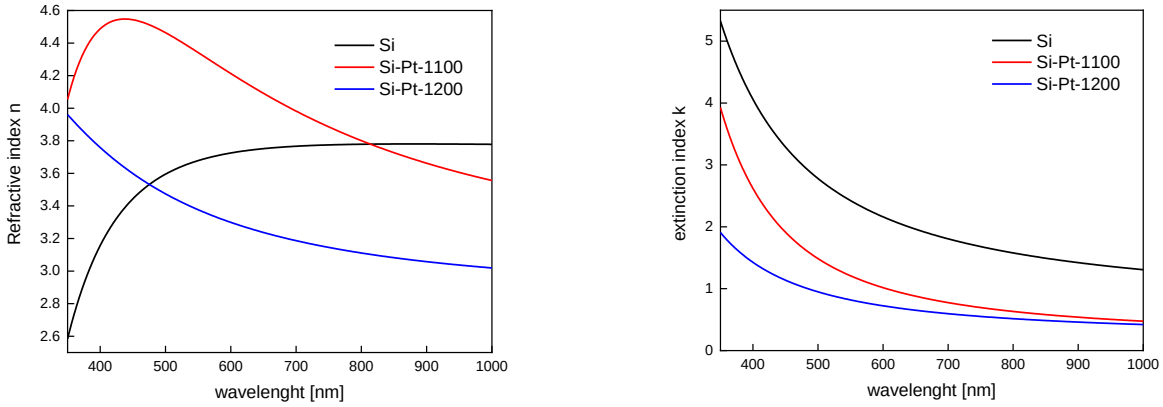

a) b)

Fig.7. Optical constant spectra of Cauchy and Urbach: a - refractive index n(λ); b - extinction coefficient k(λ).

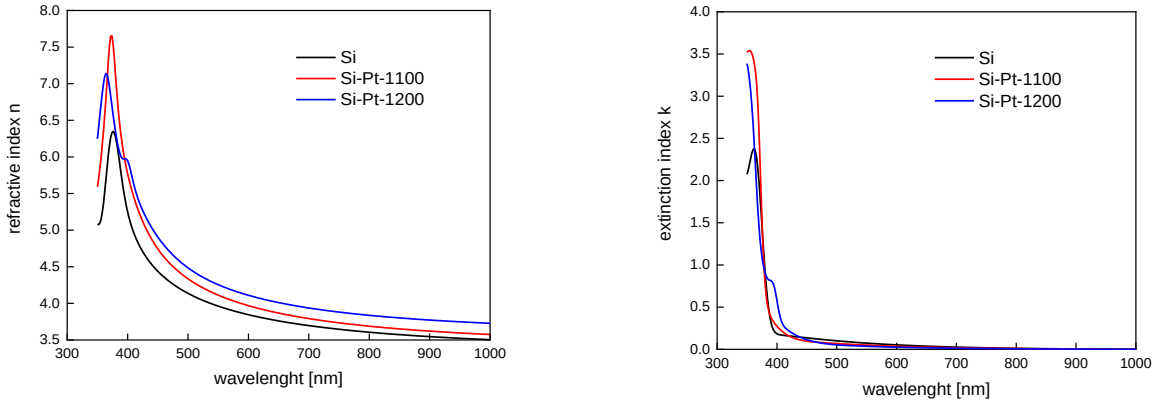

a) b)

Fig.8. Optical constant spectra for the diffusion layer of Si samples.
a is the refractive index n(λ); b - extinction coefficient k(λ).

4. Conclusion

Thus, by the method of electrochemical impedance spectroscopy, it was established that doping of n-Si samples with Pt impurity at different temperature conditions contributes to a significant (2-3 times) increase in their electrical conductivity (Table 1). It is shown that the higher the concentration of electroactive platinum atoms, the lower the concentration of radiation defects, and this, in turn, leads to a decrease in the electrical resistance of silicon samples.

It has been found that doping samples at 1200°C increases the radiation resistance of silicon samples. Increasing the doping temperature to 1200°C leads to the appearance of a linear diffusion process in the sample in a homogeneous layer with a slight deviation from Fick's second law.

The mechanism of radiation defect formation is presumably associated with the formation of complexes of radiation defects in the crystal lattice, which change the geometry of the electrical conductivity channels and create reactivity.

Using ellipsometric spectroscopy, the presence of diffusion and oxide layers on the surface of the original and doped samples was established. It has been established that, in the initial samples, implantation leads to the appearance of only an oxide layer 5.37 nm thick. After doping, in addition to the oxide layer, diffusion layers also appear. The thickness of diffusion layers in silicon doped at 1200°C is 1.5 times greater than in silicon samples doped at 1100°C.

Acknowledgment

The authors express their gratitude to the staff of the EG-5 group, the Laboratory of Neutron Physics named after I.M. Frank (JINR) for the practical help of irradiation with protons in this study.

References

1 Utamuradova Sh. B., Rakhmanov D.A. Effect of holmium impurity on the processes of radiation defect formation in n-Si<Pt>. *Physics AUC*, 2022, Vol. 32, pp.132 - 136. https://cis01.central.ucv.ro/pauc/vol/2022_32/15_PAUC_2022_132_136.pdf

2 Sapaev I., Sapaev B., Abdullaev D., Abdullayev J., Umarov A., Siddikov R., Mamasoliev A., Daliev K. Influence of the parameters to transition capacitance at NCDS-PSI heterostructure. *E3S Web of Conferences*, 2023, 383, pp.04022(1-7). doi:10.1051/e3sconf/202338304022

3 Yunusov M.S., Karimov M., Alikulov M.N., Begmatov K.A. The radiation-induced defects production in p-type silicon doped by impurities of transitional elements. *Radiation Effects and Defects in Solids*, 2000, 152(3), pp.171 – 180. doi:10.1080/10420150008211821

4 Utamuradova Sh.B., Stanchik A.V., Rakhmanov D.A. X-ray structural investigations of n-Si<Pt> irradiated with protons. *East Eur. J. Phys*., 2023, 2, pp.201. doi:10.26565/2312-4334-2023-2-21

5 Yunusov M.S., Karimov M., Khalikov P.A. Mechanisms for thermal stability of the electrophysical properties of overcompensated n-Si 〈B,S. *Technical Physics Letters*, 1999, 25(12), pp.969 – 970. doi: 10.1134/1.1262697

6 Yunusov M.S., Akhmadaliev A., Begmatov K.A. Semiconductor detector as ionising radiation dosimeter. *Radiation Physics and Chemistry*, 1995, 46(4-6), Part 2, pp.1287 – 1290. doi: 10.1016/0969-806X(95)00371-4.

7 Utamuradova Sh. B., Stanchik A.V., Rakhmanov D.A., Doroshkevich A.S., Fayzullaev K.M. X-ray structural analysis of n-Si<Cr>, irradiated with alpha particles. *New materials, compounds and applications*, 2022, Vol.6, No. 3, pp. 214 – 219. http://jomardpublishing.com/UploadFiles/Files/journals/NMCA/V6N3/Utamuradova_et_al.pdf

8 Kozlov V.A., Kozlovskiy V.V. Doping of semiconductors with radiation defects upon irradiation with protons and alpha particles. *Semiconductors*, 2001, Vol. 35, Is.7, pp.769-795. https://journals.ioffe.ru/articles/viewPDF/38565 [in Russian]

9 Galeeva A.V. Issledovanie provodimosti poluprovodnikovix struktur metodom impedansnoy spektroskopii. // Avtoreferat. 2010, Moskva. [in Russian]

10 Utamuradova Sh.B., Rakhmanov D.A., Doroshkevich A.S., Kinev V.A., Ponamareva O.Yu., Mirzayev M.N., Isayev R.Sh. IR - spectroscopy of n-Si<Pt> irradiated with protons. *Advanced Physical research*, 2023, Vol.5, No 2, pp.72. http://jomardpublishing.com/UploadFiles/Files/journals/APR/V5N2/Utamuradova_et_al.pdf

11 Turgunov N.A., Berkinov E.H., Mamazhonova D.X. The influence of thermal processing on the electrical properties of silicon, alloyed nickel. *Applied Physics*, 2020, 3, 40. PF-20-3-40.pdf (orion-ir.ru) [in Russian]

12 Shehata M.M., Truong T.N., Basnet R., Nguyen H.T., Macdonald D.H., Black L.E. *Solar Energy Materials and Solar Cells*, 2023, Volume 251, Pp.112167.

13 Vladikova D., Stoynov Z., Raikova G., Thorel A., Chesnaud A., Abreu J., Viviani M., Barbucci A., Presto S., Carpanese P. Impedance spectroscopy studies of dual membrane fuel cell. *Electrochimica Acta*, 56, 2011, pp.7955-7962. doi:10.1016/j.electacta.2011.02.007

14 Nijen D.A., Muttillo A, Dyck R.V., Poortmans J, Zeman M., Isabella O., Manganiello P. Revealing capacitive and inductive effects in modern industrial c-Si photovoltaic cells through impedance spectroscopy. *Solar Energy Materials and Solar Cells*, 2023, 260, 112486. doi:10.1016/j.solmat.2023.112486

15 Srivastava A., Sharma D., Srivastava S.K. Impedance spectroscopy analysis to probe the role of interface properties of surface micro-engineered PEDOT:PSS/n-Si solar cells. *Organic Electronics*, 2023, Volume 119, 106817. doi:10.1016/j.orgel.2023.106817

16 Utamuradova Sh.B., Rakhmanov D.A., Doroshkevich A.S., Genov I.G., Slavkova Z., Ilyina M.N. Impedance spectroscopy of p-Si<Pt>, p-Si<Cr> irradiated with protons. *Advanced Physical research*, 2023, Vol.5, No 1, pp.5-11. http://jomardpublishing.com/UploadFiles/Files/journals/APR/V5N1/Utamuradova_et_al.pdf

17 Turgunov N.A., Berkinov E.Kh., Mamajonova D.X. Decay of impurity clusters of nickel and cobalt atoms in silicon under the influence of pressure. *Journal of Nano- and Electronic Physics*, 2021, 13(5), 05006. doi:10.21272/jnep.13(5).05006

18 Raikova G., Vladikova D., Stoynov Z. Differential impedance analysis of the cathode compartment in dual membrane fuel cell. *Bulgarian Chemical Communications*, 2011, Vol.43, Is.1, pp.133 – 137.

19 Stoynov Z.B., Vladikova D.E., Abrashev B.I., Slavova M.P., Burdin B.G., Mihaylova-Dimitrova E.S., Colmenares L.C., Mainar A.R., Blázquez J.A. Screening impedance analysis of Zn-air cells. *Bulgarian Chemical Communications*, 2018, Vol.50. pp.189 – 194.

20 Daliev K.S., Ahmedov M.M., Onarkulov M.K. Influence of the Temperature and Cyclic Deformations of $(Bi_xSb_{1-x})_2Te_3$ Films on Their Resistance. *Journal of Engineering Physics and Thermophysics*, 2021, 94(5). pp.1369–1373. doi: 10.1007/s10891-021-02419-1

.

21 Turgunov N.A., Berkinov E.Kh., Turmanova R.M. Accumalations of impurity Ni atoms and their effect on the electrophysical properties of Si. *E3S Web of Conferences*, 2023, Vol. 402, pp.14018(1-8). doi:10.1051/e3sconf/202340214018

22 Utamuradova Sh.B., Daliev Sh.Kh., Stanchik A.V., Rakhmanov D.A. Raman spectroscopy of silicon, doped with platinum and irradiated by protons. *E3S Web of conferences*, 2023, Vol. 402. pp.14014(1-9) Vol.10.1051/e3sconf/202340214014

23 Turgunov N.A., Berkinov E.Kh., Turmanova R.M. The effect of thermal annealing on the electrophysical properties of samples n-Si<Ni,Cu>. *East European Journal of Physics*, 2023, 3, pp.287-290. doi:10.26565/2312-4334-2023-3-26

24 Tuan P.L., Kulik M., Nowicka-Scheibe J., Żuk J., Horodek P., Khiem L.H., Phuc T.V., Anh, Nguyen Ngoc., Turek M. Investigations of chemical and atomic composition of native oxide layers covering SI GaAs implanted with Xe ions. *Surface and Coatings Technology*, 2020, Vol 394. doi: 10.1016/j.surfcoat.2020.125871

Article accepted for publication 17.06.2023

DOI 10.31489/2023No3/43-51

UDC: 621.43.056; 004.942; 547.218.1

INVESTIGATION OF THE INFLUENCE OF LIQUID FUEL INJECTION RATE ON THE COMBUSTION PROCESS USING KIVA–II SOFTWARE

Berezovskaya I.E., Tasmukhanova A.A.*, Ryspaeva M.Zh., Ospanova Sh.S.

Al-Farabi Kazakh National University, Department of Thermophysics and Technical Physics,
Almaty, Kazakhstan, akhmetovaa2108@mail.ru

In this work, the ignition of liquid fuel was studied at various rates of fuel injection into the combustion chamber. The studied processes are described by the following equations: continuity, momentum, energy, k-ε turbulence model and others. The computational experiment was carried out using the KIVA-II software. The numerical method is efficient and takes into account various factors such as multistage chemical chain reactions, transfer of momentum, heat and mass by convection, radiation, turbulence, etc. In order to select the optimal parameters of the organization of these processes influence of the heptane injection rate into the combustion chamber on the process of combustion and self-ignition of heptane was studied. The injection rate of heptane varied from 160 m/s to 400 m/s an interval of 30 m/s. The size and temperature distributions of heptane droplets before evaporation, the concentration fields of carbon dioxide, and the temperature fields in the combustion chamber depending on the rate of fuel injection through the injector into the combustion chamber were obtained. The optimal range of heptane injection speed was determined, which is 250 m/s - 280 m/s, in order to increase the efficiency of the combustion chamber and reduce the negative impact on the environment.

Keywords: numerical methods, computer simulation, chemical kinetics, liquid fuel combustion, heptane, turbulent heat and mass transfer, injection, combustion chamber

1. Introduction

Combustion processes have been present throughout the history of mankind and surround our daily lives, from heavy industry to the simplest domestic use, passing through all modes of transport, sea, land, air and even spatial. Currently, obtaining energy by burning fuel is essential. Consequently, both in the current geopolitical framework and in the coming years, when fossil fuels become an increasingly scarce resource, its optimal use becomes more and more important every time. But that's not the only thing that matters. Harmful emissions of chemical compounds released during fuel combustion and polluting the environment are the main cause of global environmental problems, especially with the current climate change, as well as the source of many health problems for people living in polluted areas, such as densely populated cities. This means that there is a clear need to optimize fuel combustion processes in order to produce more energy for less, as well as an interest in reducing pollutant emissions resulting from combustion.

These goals can be achieved by studying and improving modern combustion processes present in both domestic and industrial applications such as internal combustion engines or gas turbines. For this, CFD (Computational Fluid Dynamics) modeling can be a very powerful and useful tool. The complexity of numerical modeling lies in the mathematical description of multi-stage processes and physical phenomena such as the evaporation of fuel droplets, the turbulence of the droplet flow.

2. Analysis of the process of turbulent combustion of liquid fuels

Combustion is a complex physical process in which various chemical compounds react exothermically, creating new compounds and heat. The conditions under which combustion occurs (flow rate, turbulence, mixture composition, temperature, etc.) determine the amount of energy and products released during combustion. Let us consider the features of the process of combustion of liquid fuels.

The method of combustion of liquid fuel in the atomized state has the greatest practical application. The process of burning liquid fuels can be divided into the following stages: atomization of fuels using nozzles; evaporation and thermal decomposition of fuel; mixing the resulting products with air; ignition of the

mixture; and combustion itself. Atomization of liquid fuel significantly accelerates its combustion and makes it possible to obtain high thermal stresses in the volumes of combustion chambers by increasing the area of the transition boundary between phases. After entering the heated volume of air, a drop of liquid partially evaporates, while the temperature of the heated air is higher than the self-ignition temperature. Due to the strong radiation of the burning torch, the droplets evaporate very quickly and undergo thermal decomposition. When fuel vapors are mixed with air, a vapor-air mixture is formed. Combustion of liquid fuel occurs in the gas phase. It is the vapors, and not the liquid of liquid fuels, that are flammable, so the liquid only ignites at a certain temperature. Combustion is then maintained spontaneously due to the heat received by the drop from the combustion of the combustible mixture. [1].

Favorable conditions for the rapid heating of fuel droplets are created due to the suspended state in which they are located. Droplet sizes depend on the time of their evaporation and become smaller with time. Also, as a result of assuming a small relative motion due to the viscosity of the gas, the shape of the small droplets becomes close to a sphere. The self-ignition temperature of liquid fuels is always higher than their boiling point, because of this, the combustion of liquid fuels is possible only in the vapor state in the presence of an oxidizing agent [2]. The burning rate depends on the nature of the movement of gases. With turbulent combustion, the mixing of the components occurs more intensively, which significantly increases the combustion rate [3].

3. Basic equations of the mathematical model of the problem of atomization and combustion of liquid fuel

The following are the main equations of the mathematical model of the problem of atomization and combustion of liquid fuel, which includes the equations of continuity, motion, internal energy and k-ε turbulence models.

The unit vectors x, y и z in the directions are denoted as $\vec{\imath}, \vec{\jmath}$ и $\vec{k}$ respectively. The radius vector is defined as $\vec{x} = x\vec{\imath} + y\vec{\jmath} + z\vec{k}$. The vector gradient operator is expressed as follows:

$$\vec{\nabla} = \vec{\imath}\frac{\partial}{\partial x} + \vec{\jmath}\frac{\partial}{\partial y} + \vec{k}\frac{\partial}{\partial z},$$

while the fluid velocity vector has the form: $\vec{u} = u(x,y,z,t)\vec{\imath} + v(x,y,z,t)\vec{\jmath} + w(x,y,z,t)\vec{k}$.

1) The fluid continuity equation is presented in general form, taking into account the chemical term and injection:

$$\frac{\partial \rho_m}{\partial t} + \vec{\nabla}(\rho_m \vec{u}) = \vec{\nabla}\left[\rho D \vec{\nabla}\left(\frac{\rho_m}{\rho}\right)\right] + \dot{\rho_m^c} + \dot{\rho^s}\delta_{m1}, \quad (1)$$

where ρ - the density of the mixture, ρ_m - the partial density of the m-th component, $\vec{u} = (u, v, w)$ - the fluid velocity components, D - the diffusion coefficient, $\dot{\rho_m^c}$- the chemical source term, $\dot{\rho^s}$- source term due to injection, δ_{m1}- Kronecker symbol for the m -th component.

2) The equation of motion for the liquid phase, taking into account droplet evaporation:

$$\frac{\partial(\rho\vec{u})}{\partial t} + \vec{\nabla}(\rho\vec{u}\vec{u}) = -\frac{1}{\alpha^2}\vec{\nabla}p - A_0\vec{\nabla}\left(\frac{2}{3}\rho k\right) + \vec{\nabla}\vec{\sigma} + \overrightarrow{F^s} + \rho\vec{g}, \quad (2)$$

where p – fluid pressure, α – a dimensionless quantity used in the PGS method, which improves efficiency at low Mach number flows where the pressure is uniform; A_0- intermittency coefficient (equal to 0 for laminar flow and 1 for turbulent), k- kinetic energy of turbulence, F^s- speed of impulse return per unit volume due to injection, g – free fall acceleration.

In this case, the viscous stress tensor is found by the formula:

$$\sigma = \mu\left[\vec{\nabla}\vec{u} + \left(\vec{\nabla}\vec{u}\right)^T\right] + \lambda\vec{\nabla}\vec{u}\vec{I}, \quad (3)$$

where μ – the dynamic viscosity of the fluid, λ - the viscosity coefficient, I - the specific internal energy.

3) Internal energy equation:

$$\frac{\partial(\rho\vec{I})}{\partial t} + \vec{\nabla}(\rho\vec{u}\vec{I}) = -p\vec{\nabla}\vec{u} + (1 - A_0)\vec{\sigma}\vec{\nabla}\vec{u} - \vec{\nabla}\vec{J} + A_0\rho\varepsilon + \dot{Q}^s + \dot{Q}^C, \quad (4)$$

where $\vec{J} = -k\nabla T - \rho D\sum_m h_m \nabla\left(\frac{\rho_m}{\rho}\right)$ – the heat flux, T - the liquid temperature, h_m- the enthalpy of the m component, ε- the turbulence energy dissipation, $\dot{Q}^s$- the source term due to interaction taking into account the release of heat per unit of time due to spraying, $\dot{Q}^C$- the source term due to chemical reactions.

4) The standard k-ε turbulence model equation consists of 2 equations:

a) the equation for the kinetic energy of turbulence:

$$\frac{\partial\rho k}{\partial t} + \vec{\nabla}\cdot(\rho\vec{u}k) = -\frac{2}{3}\rho k\vec{\nabla}\cdot\vec{u} + \vec{\sigma}:\vec{\nabla}\vec{u} + \vec{\nabla}\cdot\left[\left(\left(\frac{\mu}{Pr_k}\right)\vec{\nabla}k\right)\right] - \rho\varepsilon + \dot{W}^s; \quad (5)$$

b) equation for the dissipation rate of turbulence energy:

$$\frac{\partial\rho\varepsilon}{\partial t} + \vec{\nabla}\cdot(\rho\vec{u}\varepsilon) = -\left(\frac{2}{3}c_{\varepsilon_1} - c_{\varepsilon_2}\right)\rho\varepsilon\vec{\nabla}\cdot\vec{u} + \vec{\nabla}\cdot\left[\left(\left(\frac{\mu}{Pr_\varepsilon}\right)\vec{\nabla}\varepsilon\right)\right]\frac{\varepsilon}{k}\left[c_{\varepsilon_1}\vec{\sigma}:\overrightarrow{\nabla}\vec{u} - c_{\varepsilon_2}\rho\varepsilon + c_s\dot{W}^s\right], \quad (6)$$

The expression $\left(\frac{2}{3}c_{\varepsilon_1} - c_{\varepsilon_2}\right)\rho\varepsilon\vec{\nabla}\cdot\vec{u}$ takes into account the length of scale changes when there is velocity propagation, and the value $\dot{W}^s$ arises due to interaction with the atomizer. Table 1 shows the standard values of the constants $c_{\varepsilon_1}, c_{\varepsilon_2}, c_s, Pr_\varepsilon, Pr_k$ for the k-ε turbulence model.

Table 1. Values of constants k-ε of the turbulence model.

Constants	Numerical value
c_{ε_1}	1.44
c_{ε_2}	1.92
c_s	1.5
Pr_ε	1.0
Pr_k	1.3

In equations (5) – (6) is:

$$\vec{\sigma}:\overrightarrow{\nabla}\vec{u} = \sigma_{ij}e_{ij}, \text{ where } \sigma_{ij} = 2\mu e - \frac{2}{3}\mu e_{kk}\delta_{ij}. \quad (7)$$

The transfer coefficients can be written as follows:

$$\mu = (1{,}0 - A_0)\rho V_0 + \mu_{air} + A_0\rho c_\mu\frac{k^2}{\varepsilon};\ \mu_{air} = \frac{A_1 T^{\frac{3}{2}}}{(T + A_2)};\ \lambda = A_3\mu;\ K = \frac{\mu c_p}{P_r};\ D = \frac{\mu}{pS_c}. \quad (8)$$

Additional terms in equations (1) – (6), which appear due to interfacial exchange and due to chemical reaction, are given in [4].

4. Geometric and physical models of energy fuel combustion

For the computational experiment, a model of a cylindrical combustion chamber with a height h = 15 cm and a base radius r = 2 cm was used. The computational grid consists of 600 cells. The injector was located at the bottom of the chamber in the center, and heptane was injected through it into a preheated oxidizer. The injection occurs unto a stationary medium. The combustion chamber is filled with air. For practical calculations, it is assumed that air consists of 21% oxygen and 79% nitrogen. The injection time of fuel droplets is 1,4 ms. After injection, the fuel rapidly evaporates, and its combustion is carried out in the gas phase. The initial radius of the injected drops is 3 μm. Droplet injection angle is 10º. The pressure in the combustion chamber is $4 \cdot 10^6$ Pa. The area of the injector is $2 \cdot 10^{-4}\text{cm}^2$.

The general view of the model under consideration is shown in Figure 1. The initial temperature inside the combustion chamber was set to 900 K, the temperature of the chamber walls was 353 K. For the study, heptane was taken as a liquid fuel (chemical formulaC_7H_{16}), since it is a mobile and flammable liquid and is used as a reagent and reference fuel in determining the octane numbers of automobile and aviation gasolines.

Mass of injected heptane m = 7 mg. The chemical kinetics of heptane is: $C_7H_{16}+11O_2 \rightarrow 7CO_2 + 8H_2O$. A numerical experiment was carried out using the KIVA-II software with k-ε turbulence model. The injection speed was varied from 160 m/s to 400 m/s with an interval of 30 m/s. Combustion occurs during the transition from the liquid phase to the gas phase and takes approximately 4 ms in time, while the evaporation of fuel droplets takes approximately the first 2 ms [5].

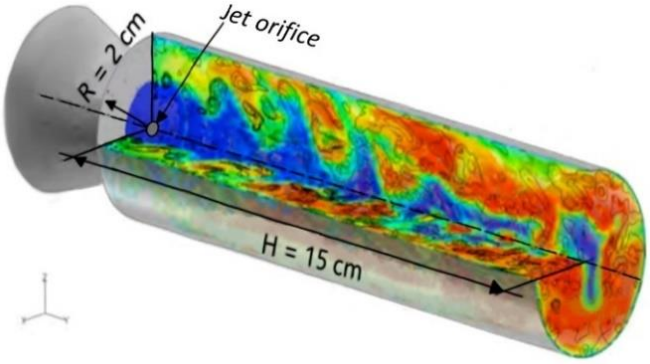

Fig.1. General view of the combustion chamber.

Solving the problem of liquid drops and their interaction with gas phase is an extremely difficult problem. In order to calculate the mass, angular momentum and heat exchange between the evaporating droplet and the gas, it is necessary take into account the distribution of droplets by size, velocity and temperature. In many flows, when calculating sprayed liquids, it is necessary take into account drop vibrations, distortions and discontinuities. For engine calculation, it is also very important to take into account the collisions of drops between themselves and their association into larger drops.

A mathematical model that can explain these complex physical processes, is reduces to the formulation of the evaporation equation. From this the equation is the distribution of the probability density function *f*, having ten independent variables in addiction to time: three *x* positions of the droplet, three components of velocity *v*, radius *r*, temperature T_d (assumed to be the same within the drop), the deviation from the sphere *y* and the change in co deflection time $dy/dt = \dot{y}$. The dimensionless quantity *y* is proportional to the displacement of the surface drop from its equilibrium position to the drop radius *r*.

Physical meaning function f is defined in such a way$f(x, v, r, T_d, y, \dot{y}, t)dvdrdT_d dyd\dot{y}$- probable number of drops per unit volume with coordinate *x* and time *t*, velocities in the interval (*v*, *v* + *dv*), radius in the interval (*r*, *r* + *dr*), temperatures in the interval (T_d, T_d + dT_d) and displacement parameters in the intervals *(y, y + dy)* and ($\dot{y}$, $\dot{y}$ + $d\dot{y}$).

5. Results of a computer experiment of heptane combustion

Below are the results of numerical simulation of the process of burning liquid fuel in the combustion chamber using a stochastic mathematical model, which makes it possible to simulate the effect of the collision of evaporating liquid droplets with aerodynamic discontinuities.

Figure 2 shows plots of fuel droplet size distribution for some injection rates at 2 ms. A qualitative analysis of the graphs revealed that at initial velocities in the range between 160 m/s and 190 m/s, the maximum droplet distribution height of 2.2 cm was recorded, and with a quantitative analysis, at a speed of 250 m/s and above, the droplets spread to a larger volume. Upon reaching 220 m/s and with a subsequent increase in speed to 280 m/s, a sharp drop in height is observed to 1.1 cm, while the number of drops decreases significantly. This is followed by a smooth growth in height up to 1.4 cm. The maximum droplet size was noted at a speed of 220 m/s (fig.2).

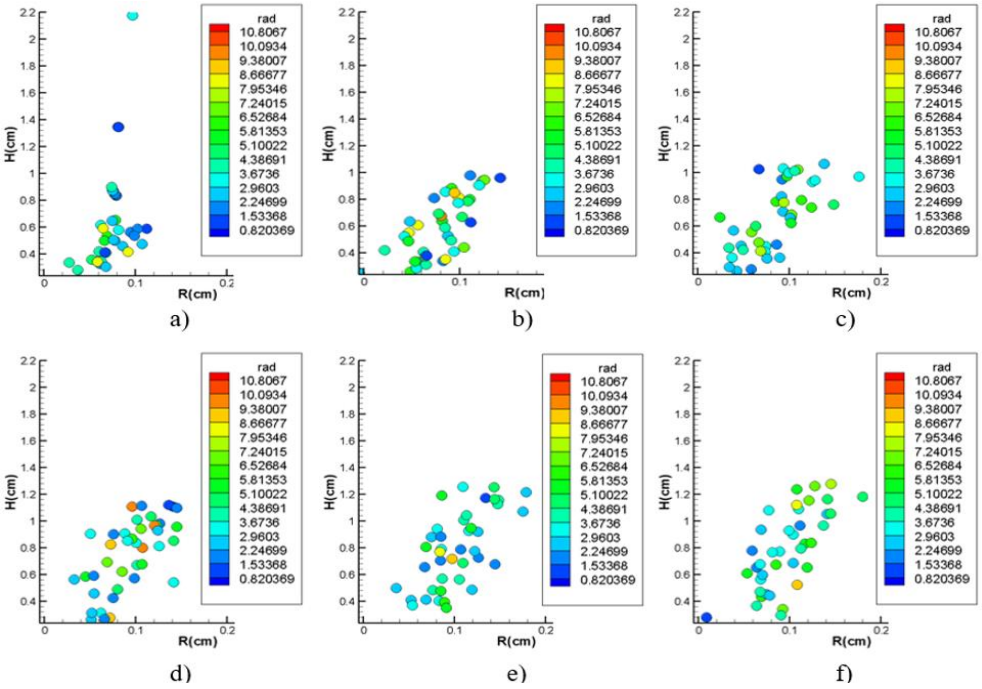

Fig. 2. Droplet size distribution (rad, μm) in the space of the combustion chamber at time t = 2 ms, at injection speed: a) 190 m/s; b) 220 m/s; c) 250 m/s; d) 280 m/s; e) 310 m/s; f) 340 m/s.

Changes in droplet temperature at a time of 0.4 ms with an increase in injection rate are shown in Fig. 3. After 0.4 ms, the temperature of the drops decreases to the boiling point of heptane - 371 K. Quantitative analysis revealed that at the lowest velocities of 160-190 m/s, a huge number of drops are observed with a temperature of approximately 450 K to 485 K. At velocities above 220 m/s droplets have a temperature of 490 K and above. After that, the temperature decreases at 340 m/s to 465 K and below. The highest droplet temperatures were found in the velocity range from 220 m/s to 340 m/s. This means that in this speed range the fuel droplets warm up much faster.

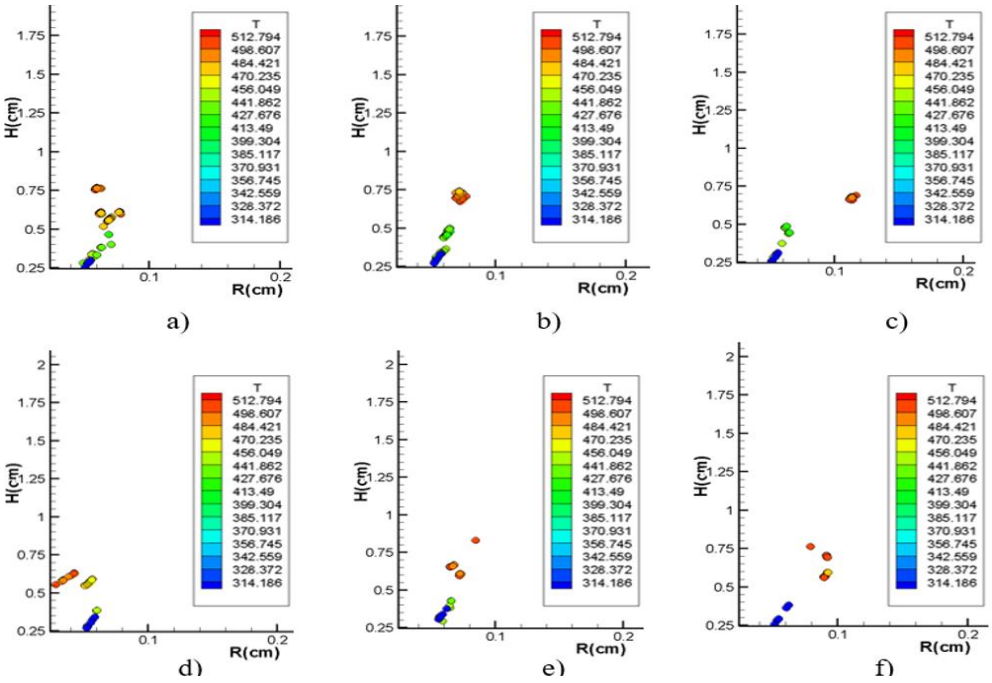

Fig. 3. Graph of droplet temperature change (T, K) at time $t = 4 \cdot 10^{-4}$c, at injection speed: a) 190 m/s; b) 220 m/s; c) 250 m/s; d) 280 m/s; e) 310 m/s; f) 340 m/s.

All obtained maximum values of droplet sizes and temperatures at different injection rates are listed in Table 2. Using these data, illustrative line graphs are compiled to track changes in droplet sizes and temperatures at different injection rates of liquid fuel into the combustion chamber, presented in Figure 4.

Table 2. Maximum values of the radius and temperature of heptane droplets at different injection speeds

No.	$V_{injection}$, m/s	R max, μm	T max, K
1.	160	9.57	508.23
2.	190	9.42	506.69
3.	220	10.81	499.11
4.	250	9.98	512.79
5.	280	10.45	505.87
6.	310	9.85	496.26
7.	340	9.91	497.46
8.	370	8.44	464.09

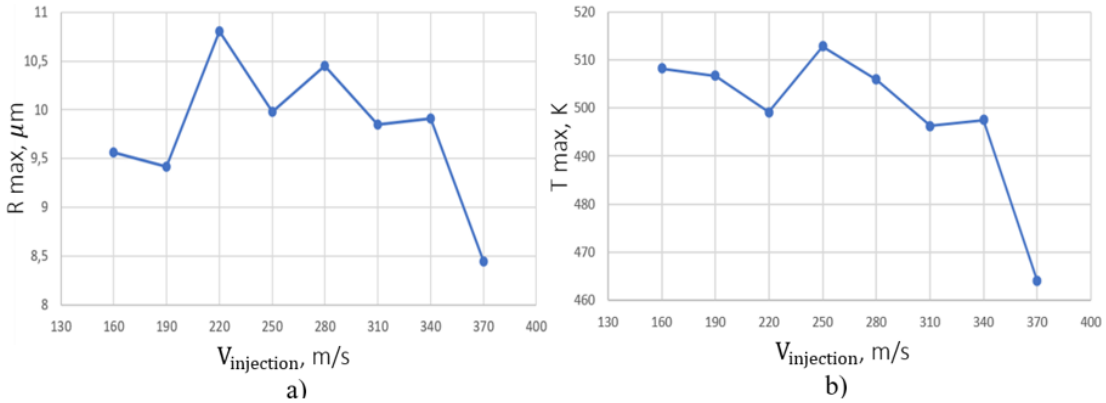

Fig. 4. Line plot of injection speed (V, m/s):
a) on the size distribution of heptane droplets (R, μm) in the space of the combustion chamber;
b) on the temperature distribution of heptane droplets (T, K) in the space of the combustion chamber.

It can be concluded that in the range from 220 m/s to 280 m/s, the droplet sizes increase during mixing, while the number of droplets is much smaller. And, also the distribution of droplets along the height is much lower, in contrast to the data at the initial and final values of the injection speed. The highest droplet temperatures were found in the velocity range from 160 m/s to 280 m/s. This means that in this range of speeds, fuel droplets warm up much faster, respectively, evaporate and ignite faster.

The value stands out strongly on the graph at a speed of 370 m / s, which indicates the need to check these calculations for a miss. The misses were calculated by the Dixon test with a small number of measurements (n<10): $\frac{x_n - x_{n-1}}{x_n - x_1} > Z_q$, where Z_q =0,47, at a significance level q =0.05 for n=8. The known values are listed in Table 3. And below, calculations are made according to the Dixon criterion.

Table 3. Values used for calculations according to the Dixon criterion.

	$V_{injection}$, m/s	T_{max}, K	R_{max}, μm	T'_{max}, K
X_1	355	500.484	10.5786	2187.75
X_{n-1}	365	500.953	9.80386	2194.84
X_n	370	464.091	8.44117	2190.81

a) Checking the value of the maximum temperature of heptane droplets at a speed of 370 m/s:

$$\frac{T_5 - T_4}{T_5 - T_1} = \frac{464.091 - 500.953}{464.091 - 500.484} = \frac{-36.862}{-36.393} = 1.0129 > 0.47.$$

b) Checking the value of the maximum radius of heptane droplets at a speed of 370 m/s:

$$\frac{R_5 - R_4}{R_5 - R_1} = \frac{8.44117 - 9.80386}{8.44117 - 10.5786} = \frac{-1.36269}{-2.13743} = 0.6375 > 0.47$$

c) Checking the value of the maximum radius of heptane droplets at a speed of 370 m/s:

$$\frac{T'_5 - T'_4}{T'_5 - T'_1} = \frac{2190.81 - 2192.94}{2190.81 - 2191.75} = \frac{-2.13}{-0.94} = 2.2659 > 0.47.$$

Since the resulting values are greater than the Z_q value, the results for 370 m/s in this case are a gross error and are not taken into account in the analysis.

The maximum values of the temperature in the chamber and the concentration of combustion product carbon dioxide at various speeds are listed in Table 4. It can be noted that the maximum concentrations of reactants and combustion products released during heptane self-ignition have not practically changed, since the concentration of reactants and combustion products depends on the mass of the injected fuel and the chemical properties of this fuel. In this study, the mass of heptane remained constant for all experiments. The maximum concentrations of nitrogen, oxygen and hydrogen hydroxide at all studied speeds are the same and respectively equal n(N_2) = 0.75 g/g, n(O_2) = 0.1875 g/g, n(H_2O) = 0.06 g/g.

Table 4. Maximum chamber temperatures and concentrations of carbon dioxide for various heptane injection rates.

No.	$V_{injection}$, m/s mm/m/s	T'(max), K	n(CO_2), g/g
1.	160	2166.63	0.1273
2.	190	2163.34	0.1280
3.	220	2167.47	0.1279
4.	250	2181.91	0.1284
5.	280	2181.16	0.1284
6.	310	2180.59	0.1279
7.	340	2188.19	0.1279
8.	370	2190.81	0.1282

The temperature field distributions for each investigated speed are shown in Figure 5 at 4 ms, when the mixture of heptane droplets with air ignites spontaneously.

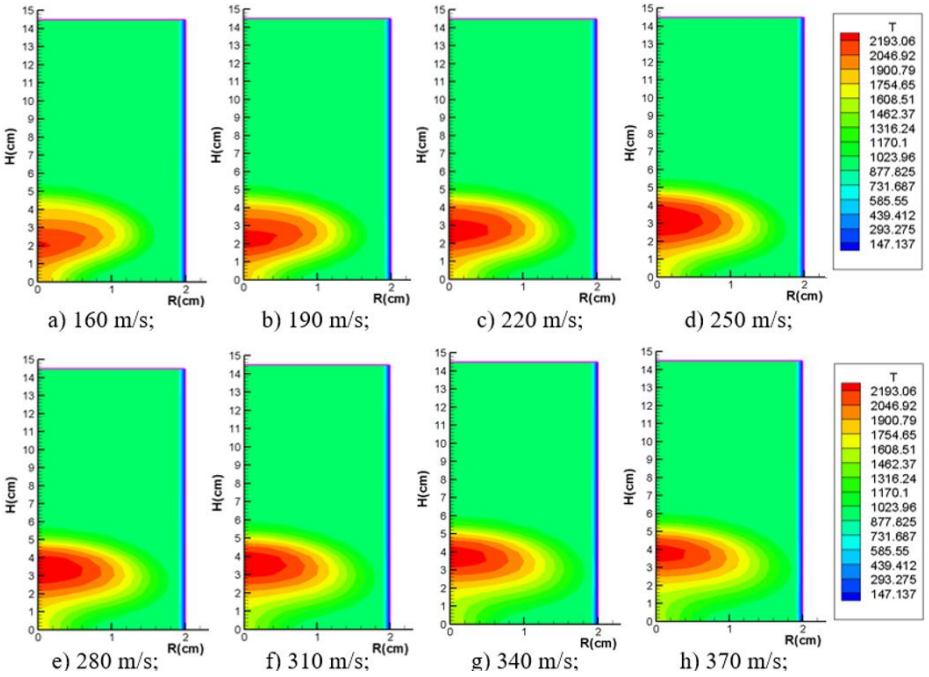

Fig.5. Temperature fields in the space of the combustion chamber at time t = 4 ms, at different speeds.

It can be noted that in the speed range from 250 m/s to 280 m/s, the ignition zone is the largest in area and has the highest temperature. This means that the heptane combustion process is faster and more intense. At lower velocities up to 250 m/s and higher velocities of 280 m/s, self-ignition occurs more slowly and less intensively.

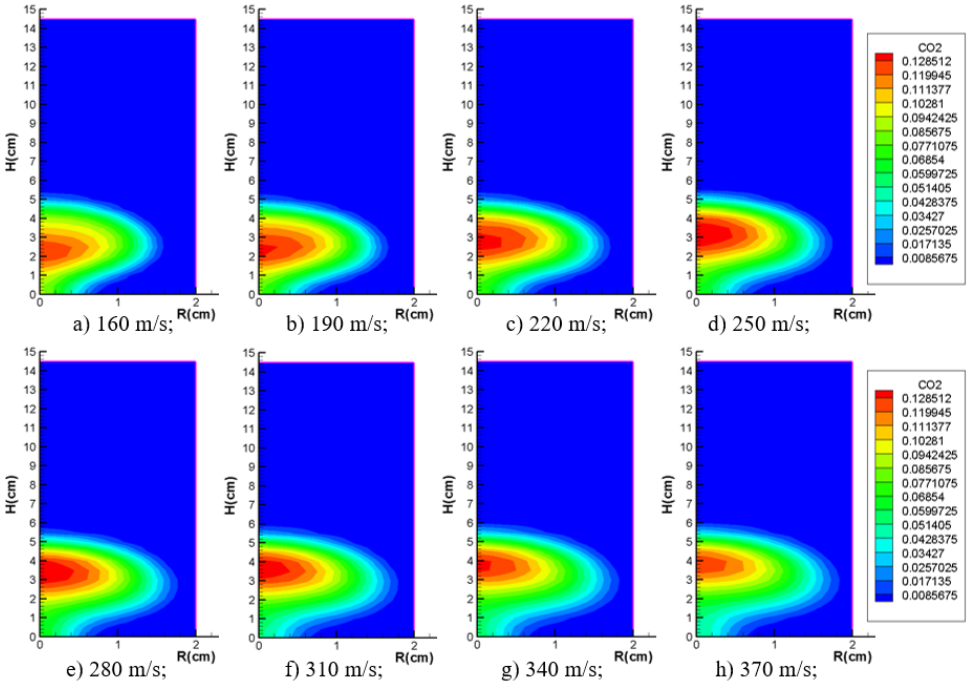

Fig.6. Fields of carbon dioxide (CO_2) concentrations in the space of the combustion chamber at time t = 4 ms, at different speeds.

The figure 6 shows the fields of carbon dioxide concentrations at time t = 4 ms, at different speeds. The largest amount of carbon dioxide was noted at speed in the interval 220 m/s - 280 m/s, but the amount of carbon dioxide released is within the maximum allowable value. This means that at speeds of 220 - 280 m/s, the process of burning liquid fuel proceeds more intensively.

The mathematical model used in numerical modeling in KIVA-II is the basis of the KIVA-3V software. The following authors compared the experiment and numerical modeling, in which the dependence of the torch length on temperature was studied [6]. Figure 7 shows the dependence of the flame length on temperature, on the basis of which it is possible to confirm the agreement between the results of the numerical experiment and the experimental data. Consequently, based on the conclusions of the authors, KIVA-II adequately describes real processes and can be used for research purposes.

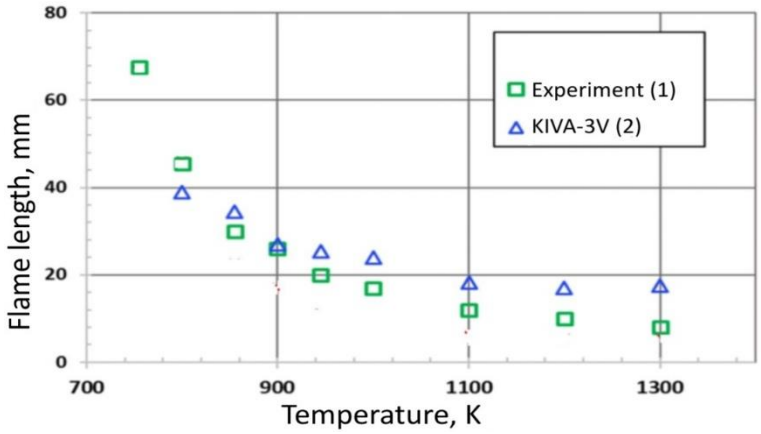

Fig.7. Dependence of the flame length on temperature: 1 - full-scale experiment (Sandia National Laboratories), 2 - numerical experiment (KIVA-3V) [7]

6. Conclusion

In this work, in the course of the study, the distributions of heptane droplets by size and temperature before evaporation, the distributions of the concentration fields of carbon dioxide, and the temperature fields depending on the rate of fuel injection into the combustion chamber were obtained.

As a result of the study, it was revealed that in the range of injection speeds from 250 m/s to 280 m/s, fuel droplets warm up much faster, respectively, evaporate and ignite faster. Consequently, the process of fuel combustion is faster, more intense and more efficient with low fuel consumption.

Research allows choosing conditions for more optimal combustion of heptane, under which the maximum thermal effect of the reaction and small emissions of harmful substances into the environment are observed. The results obtained will not only reduce the negative impact on the environment, but expand the scientific understanding of thermal physics, physics of reactants, thermal power engineering, aircraft and rocket science.

REFERENCES

1. McAllister S., Chen J., Carlos Fernandez-Pello A. *Fundamentals of Combustion Process*. Mechanical Engineering Series, Springer Publication. 2011, 302 p. (Electronic textbook).

2. Askarova A.S., Gorohovsky M.A., Bolegenova S.A., Berezovskaya, I.E. *Numerical modeling of the processes of ignition and combustion of liquid fuels: monograph.* Almaty, Kazakh University. 2015, 124 p. [in Russian]

3. Kowalski M., Żurek J., Jankowski A. Modelling of combustion process of liquid fuels under turbulent conditions. *Journal of KONES Powertrain and Transport*, 2015, Vol. 22, Is. 4, pp.355 – 364. doi:10.5604/12314005.1168562

4. Amsden A.A., O'Rourke P.J., Butler T.D. KIVA-II: A Computer Program for Chemically Reactive Flows with Sprays. *Technical report.* 1989, 180p. doi:10.2172/6228444

5. Askarova A.S., Bolegenova S.A., Voloshina I.E., Ryspaeva M.Zh. Influence of liquid fuel mass on its self-ignition and combustion. *Proceedings of the National Academy of Sciences of the Republic of Kazakhstan*. *Series of Physics and Mathematics*, 2002, No.2, pp. 3 – 11. [in Russian]

6. *Engine combustion network database*. *Sandia National Laboratories*, USA. 2007. Web. Available at: https://ecn.sandia.gov/engines/

7. Kärrholm F.P., Tao F., Nordin N. Three-dimensional simulation of diesel spray ignition and flame lift-off using KIVA-3V CFD code. SAE *Technical Paper*, 2008, 2008-01-0961. doi:10.4271/2008-01-0961

Article accepted for publication 12.05.2023

DOI 10.31489/2023No3/52-61

UDC 537.322

THERMOELECTRIC MONITORING OF THERMAL RESISTANCE IN ELECTRONIC SYSTEMS

Abouellail A.A.[1], Chang J.[2], Soldatov A.I.[3,4], Soldatov A.A.[3,4], Kostina M.A.[3,4], Vasiliev I.M.[5]

[1] Sphinx University, New Asyut, Egypt

[2] Institute for Advanced Study of Shenzhen University, Shenzhen, China

[3] National Research Tomsk Polytechnical University, Tomsk, Russian Federation, mariyakostina91@mail.ru

[4] Tomsk State University of Control Systems and Radioelectronics, Tomsk, Russian Federation

[5] Scientific and production center LLC "LEMZ-T", Tomsk, Russian Federation

The article proposes to apply the method of thermoelectric testing to determine the thermophysical parameters of the thermal interface. A thermal interface is located between metal surfaces, between which, thermoelectromotive force occurs during heating at any stage of the device operation. The obtained graphs of the temperature difference dependence on the heating time, measured by thermocouples, and measured using thermoelectromotive force confirm the accuracy of the thermoelectric method of testing. Graphs visualize the heat transfer process with thermal resistance variation, temperature fluctuations and the resulting thermoelectromotive force. The proposed method makes it possible to monitor thermal resistance with an error of less than 8 %.

Keywords: thermal interface, thermal resistance, thermoEMF, Seebeck effect, thermoelectric monitoring.

1. Introduction

In modern electronic technology, heat-conducting paste is widely used to ensure good thermal contact (low thermal resistance) between the body of a powerful semiconductor element and a heat sink. It functions as a thermal interface, which improves the quality of heat transfer from a heating element to a heat sink [1-5]. Defects that appear after applying the heat-conducting paste to the heat sink can lead to negative consequences, such as reduced performance and service life of the conductor element, false operation of overheating protection circuits, etc. Therefore, well-timed monitoring of thermal contact makes it possible to avoid a decrease in the reliability of the device and the system as a whole, as well as its premature failure.

At present, monitoring of the thermophysical parameters of a thermal interface after its application to a heat sink surface is carried out manually [6] or by indirect methods [7], and available methods only offer casual inspection or random testing. Inspection of the thermophysical parameters of the thermal interface is possible in some cases, but for its implementation, the device under study must have a temperature-dependent parameter, however, it should be borne in mind that the data obtained also depend on the indirect parameters of the product, for example, on the heat capacity of the product. Available monitoring methods do not provide ability to inspect thermal contact after installing a heat-generating element on a heat sink with a thermal interface in automatic mode, and neither do they provide ability to exclude the influence of other factors of the thermal circuit of the device under study.

As widely used thermal interfaces, heat-conducting gaskets, pastes, and adhesives can be distinguished [8-10]. The silicone heat-conducting paste (SHCP-8) is a particular example of a thermal interface material, which is widely used in Russia to improve thermal conductivity between thermocoductive elements and is locally produced in accordance with the requirements of standard technological regulations GOST 19783-74 [11] and typically recommended for use in in the temperature range from - 60 ºC to + 180 ºC. Among foreign modeling systems, we can specify HK-part HY880, ARCTIC MX-4, etc.

In modern industries, attempts are made to minimize the volume of electronic devices as much as possible, while maintaining its specific power; therefore, heat sinks for cooling transistors are in such a size that the temperature of the transistor chip at rated load does not exceed the normal operating conditions specified in the technical specifications, i.e. about 150°C.

2. **Problem statement**

The main thermophysical characteristic of a thermal interface, which characterizes its quality, is thermal resistance. The contribution of thermal resistance of the thermal interface to the total thermal resistance of the device thermal circuit R_{thcs} is from 20 % to 65 %, therefore the thermal interface must completely fill the air gap between the heat element body and the heat sink, and the thickness of the thermal interface layer must be at an optimal value, because a very thin layer may not provide high-quality heat transfer due to incomplete filling of air cavities (Figure 1) [12-18].

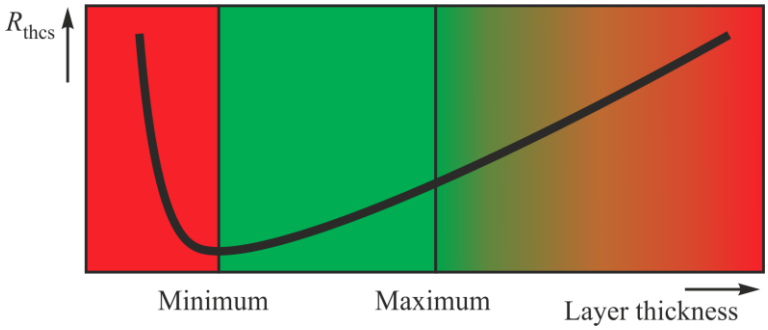

Fig.1. The dependence of the thermal resistance between the heat generating element and the heat sink on the thickness of the thermal interface layer [6]

The presence of air cavities in the gap between the body of the heating element and the cooling heat sink or poor thermophysical characteristics of the thermal interface due to improper application of the thermal interface, with prolonged use of the device, can lead to overheating of the device and ultimately a failure or, at best, reduction in the service life of the product. Therefore, manufacturers of semiconductor devices give recommendations on choosing a heat sink and choosing the right heat-conducting compound. This is especially important for field effect transistors. the open state resistance directly depends on the temperature of the chip, and the open state resistance, in turn, affects the efficiency of voltage converters.

Some companies supply their devices to consumers with a thermal interface already applied, which increases the cost of the device compared to other alternatives. However, this measure does not exclude the possibility of integrity violation of the thermal interface during transportation or installation of the heat-generating device on a heat sink without additional visual inspection before installation. Currently, there are several methods for providing the thermal resistance when installing a heating unit on a heat sink.

Weighing on precision scales is a method that does not guarantee the required thermal resistance, since it depends not only on the amount of heat-conducting compound, but also on its distribution between the heat sink and the body of the device. With uneven distribution of the thermal interface, local overheating of the element is possible [6].

Using a stencil is another method, where the required thermal resistance is provided by using the optimal amount of thermal interface. Its amount depends on the thickness of the stencil, the area of the holes and the distance between the holes and is calculated by the formula [7]:

$$V_{TIS} = S_{hol.} \cdot h_{st.}, \quad (1)$$

where V_{TIS} is the volume of the thermal interface, $S_{hol.}$ is the total area of all holes in the stencil, and $h_{st.}$ is the stencil thickness.

This method does not allow for monitoring the thermal resistance of the system (heat element - thermal interface – heat sink) after the system is assembled.

Simple comb-type Mechanical Thickness Gauges are widely used to provide the required thermal resistance (Figure 2). The thickness gauge is installed on the surface to be checked with a thermal interface with base teeth, and moves parallel to the surface under study, leaning on the base teeth. Because the measuring teeth are at a known distance from the base teeth, the mark left by them on the thermal interface layer indicates the thickness of the thermal interface.

.

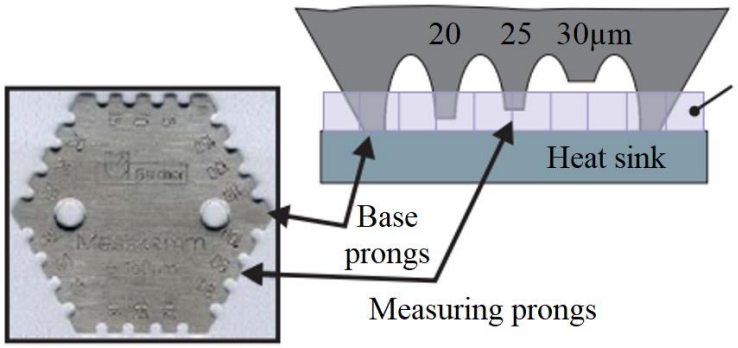

Fig.2. Comb Type Mechanical Thickness Gauge [6]

The disadvantage of this method is the damage to the layer in the inspection zone and the mandatory visual check after each measurement.

Monitoring the thermophysical characteristics of a thermal interface using a transfer circuit is a method that is implemented in many manufactured devices, which have a so-called temperature-dependent parameter. The total thermal resistance "chip-to-case" or "chip-to-environment" R_{Tjx} of semiconductor devices is given by:

$$R_{Tjx} = \frac{T_{j.} - T_x}{P_{pn}}, \tag{2}$$

where T_j – semiconductor chip temperature; T_x – housing or ambient temperature; P_{pn} – heat dissipation power of the device [19].

The method of monitoring standard thermal resistance requires the thermal resistance of the system (heat-generating element body - thermal interface - cooling heat sink) to be determined through the values of previously known thermal resistances and capacitances of the thermal circuit elements:

$$C_{th\Sigma} = \frac{P_{heat} \cdot t}{T_{SC.}(t) - T_{SC.}(0)}, \qquad R_{th\Sigma} = \frac{T_{SC.}(t) - T_{SC.}(0)}{P_{heat}}, \tag{3}$$

where P_{heat} – device power dissipation value; $T_{SC}(t)$ – initial temperature of the device chip, $C_{th\Sigma}$ – heat capacity, $R_{th\Sigma}$ – thermal resistance [20].

When determining the transfer function, it is necessary to maintain the temperature of the body of the object constant, which complicates the control process and the scheme of the measuring installation as a whole.

The modulation method for monitoring the thermophysical parameters of a thermal interface [21] has a sequence of current pulses with a duration t_{imp}, which is applied to the object under study, and can be expressed by the formula:

$$t_{imp} = t_{av}(1 + k \cdot \sin 2\pi ft), \tag{4}$$

where t_{av} – average pulse duration; k – modulation factor; f – pulse frequency [22].

In this case, the average heating power $P_{heat}(t)$ will be determined by the expression:

$$P_{heat}(t) = P_{av} + P_{var} \cdot k \cdot \sin 2\pi ft, \tag{5}$$

where P_{av} – average delivered power; P_{var}– peak-to-peak amplitude of the variable component of the supplied power [23].

A non-linear change in the heating power affects the change in the chip temperature with some time shift (temperature phase shift). The temperature phase shift is determined:

$$\varphi = arctg \frac{B(f)}{A(f)}, \tag{6}$$

where $A(f)$ – imaginary component and $B(f)$ – material component.

Functions $A(f)$ and $B(f)$ are defined through the discrete Fourier transform by the expressions:

$$A(f)=\frac{2}{N}\sum_{i=1}^{N}T_{SC}(t)\cdot\cos 2\pi(\frac{i}{N}),$$
$$B(f)=\frac{2}{N}\sum_{i=1}^{N}T_{SC}(t)\cdot\sin 2\pi(\frac{i}{N}). \quad (7)$$

Thermal impedance module $|Z_T(f)|$ defined as:

$$|Z_T(f)|=\sqrt{\frac{A^2(f)+B^2(f)}{P_{\text{var}}}}\ . \quad (8)$$

The analysis performed showed that, at present, there is no non-destructive method for monitoring the thermal resistance of the system with a heat-generating unit - thermal interface - heat sink in the assembled state.

3. Mathematical Modeling

The main thermophysical characteristic of a thermal interface is its thermal resistance, which in the steady state is determined by the formula:

$$R_S=\frac{\Delta T}{P}, \quad (9)$$

where ΔT – temperature difference; P – thermal power flow passing through the thermal interface.

To measure the temperature difference at the boundaries of the thermal interface layer, it is necessary to install two temperature sensors so that one of them has thermal contact only with the body of the semiconductor element as close as possible to the thermal interface and does not have thermal contact with the heat sink, and the second has thermal contact with the heat sink and does not have thermal contact with the body of the semiconductor element. Installing temperature sensors in this way complicates the verification process and introduces an error in determining the thermal resistance, because part of the heat is dissipated in the body of the semiconductor device up to the temperature sensor [24].

When two metals of different chemical nature come into contact, due to the difference in charge carriers at the external level, thermoEMF appears between dissimilar metals [25-28]. Due to the influence of temperature on the concentration of charge carriers at the external level, the value of the electromotive force in this case will directly depend on temperature:

$$E=(T_2-T_1)\frac{k}{e}\ln\frac{n_2}{n_1}, \quad (10)$$

where T_2 – hot junction temperature; T_1 – cold junction temperature; k - Boltzmann's constant; e – electron charge; n_2 – carrier concentration of heatsink material (alloys of WCu or MoCu); n_1 – body material carrier concentration (alloys of Al or Cu).

Value:

$$\frac{k}{e}\ln\frac{n_2}{n_1}, \quad (11)$$

is a constant for two metals and is called the thermopower coefficient or the Seebeck coefficient and is denoted by α. Formula (10) is shortened to the form:

$$E=(T_2-T_1)\cdot\alpha. \quad (12)$$

Expressing ΔT from the formula (11) ($\Delta T=T_2-T_1$) and substituting into the formula (9), we get:

$$R_S=\frac{E}{\alpha\cdot P}. \quad (13)$$

To determine the dependence of heat distribution in the object under study over time, as well as on thermal resistance, we will build a mathematical model in which two cylinders with a radius R and a height L_1 and L_2 are interconnected (Figure 3.a). The lower part of the cylinder with height L_1 at points A and D heats up instantly to 100°C, which corresponds to placing the cylinder in boiling water. Heat is transferred to

.

a cylinder with a height L_2, and its upper part is cooled by air with a temperature corresponding to normal climatic conditions. At the contact point of the cylinders, there is a heat-conducting layer with a thickness of l_s (distance B_1B_2 in Figure 3.a).

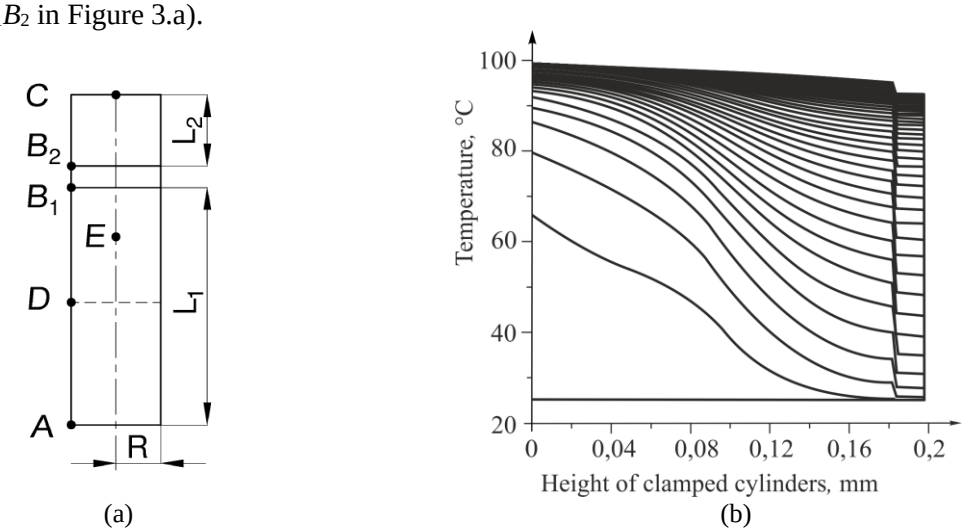

(a) (b)

Fig.3. Object under study; (a) Schematic representation, (b) temperature-time dependence of heat distribution in the cylinder

The mathematical model assumes that the contact between the cylinders is ideal, the thermal conductivity coefficients of substances are constant and do not depend on temperature, the temperature of boiling water is constant and equal to 100°C, and the thermal resistance in the contact zone of two cylinders is completely described by the effective thermal resistance of the contact layer.

By setting the parameters of the cylinders R=25 mm, AC=20 cm, AB_1=19.5 cm, AE=19 cm, AD=9.5 cm, the properties of the material of the cylinders correspond to the properties of the aluminum alloy material (for example: AMg6, AW-5056, AW-AI, Mg5Cr, etc.), the properties of the material of the heat-conducting layer correspond to the properties of the silicone heat-conducting paste SHCP-8 with a thickness of 0.05 mm, according to the results of calculations, we obtain a temperature slice (Fig. 3.b) of heat propagation in cylinders with lengths L_1 and L_2 connected through a thermal interface layer.

As can be seen from the obtained temperature distribution, the effective heat distribution in the region of 0.18 mm (Fig. 3.b) is deteriorated due to the low thermal resistance of the thermal interface compared to the thermal resistance of the cylinders. This picture clearly shows the effect of thermal resistance of the thermal interface on heat dissipation. When the specific thermal conductivity of the thermal interface and its thickness change, the transition process establishment time and the maximum temperature change (Fig. 4).

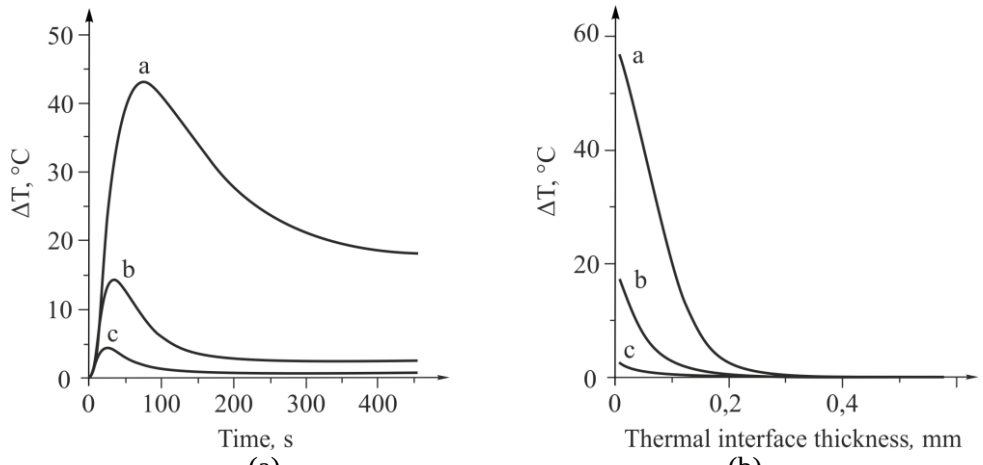

(a) (b)

Fig.4. Dependence of the temperature difference between two cylinders on: (a) time and on (b) the thickness of the thermal paste, curve a - thermal conductivity of the thermal paste is 10 times less than the nomin value; curve b - nominal specific thermal conductivity; curve c - thermal conductivity of thermal paste is 10 times higher than the nominal

Comparing the curves in Fig. 4, we can conclude that after the rapid heating of the first cylinder, the heating of the second cylinder occurs with some delay due to the finite value of the heat flux through the contact boundary of the two cylinders. Due to the different heating rates of the cylinders, an extremum appears on the graph. As the temperature of the second cylinder rises, the difference between the temperatures of the first and second cylinders decreases and tends to a steady value. For different thermal conductivity of the thermal interface, the steady-state value will be different, the higher the thermal conductivity, the smaller the temperature difference between the cylinders. The value of the extremum also depends on the thermal conductivity, the higher the thermal conductivity, the lower the value of the extremum. The graphs in Fig. 5 show the results of a theoretical study of the influence of the thermal interface thickness on the thermoEMF, whose value depends on temperature difference of the cylinders.

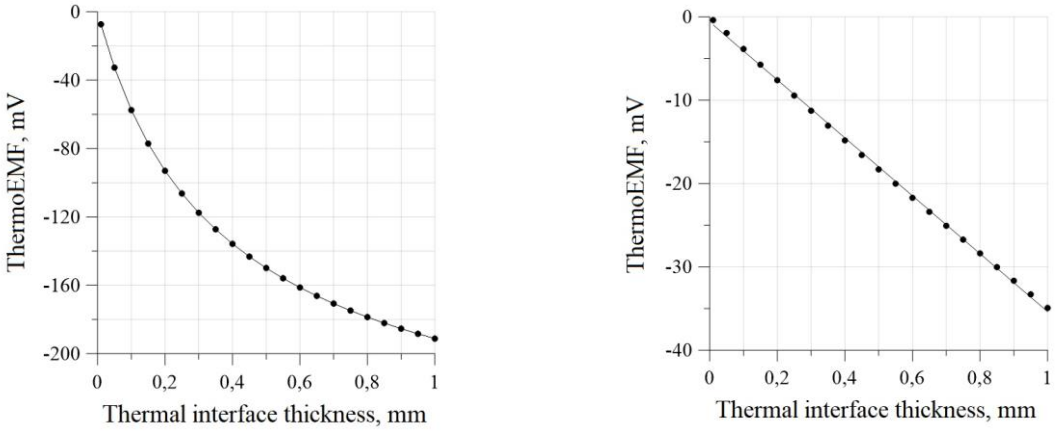

(a) (b)

Fig.5. Dependence of thermoEMF on the thickness of the thermal interface layer; (a) transient mode, (b) steady state

The change in thermoEMF in the transient mode is almost 4 times greater than in the steady state, however, the nature of the dependence in the transient mode is nonlinear, and in the steady state it is linear, which makes this mode more preferable for monitoring conditions.

The housings of power semiconductor devices are made of different materials (alloys of WCu or MoCu), and in addition, they can be coated with nickel, tin, silver or gold, which have different Seebeck coefficients. The influence of various coatings of the heat-generating unit on the thermoEMF is shown in Fig.6.

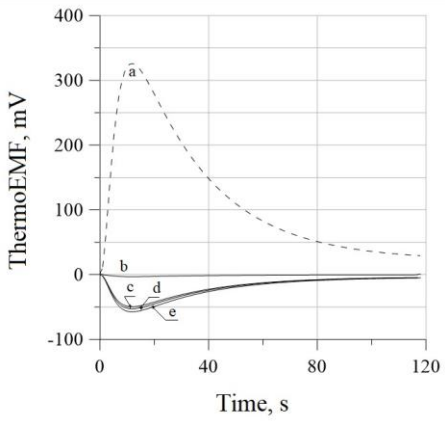

Fig.6. Dependence of thermoEMF on time with a thermal interface of 0.1 mm thickness between aluminum and copper coated with: a) nickel, b) tin, c) silver, d) gold, e) uncoated

Figure 6 shows that with respect to copper, nickel has the highest thermoEMF. This is due to its large value of the Seebeck coefficient compared to other materials [29]. Tin coating relative to copper gives the smallest value of thermoEMF due to its small Seebeck coefficient, with a maximum value was 3.2 mV. The remaining coatings give similar results due to the similar value of the Seebeck coefficient.

.

4. Model Verification

To verify the proposed model, experimental studies were carried out, and samples similar to the mathematical model were used as the object of study. The scheme of the experimental setup is shown in Figure 7 [30-32].

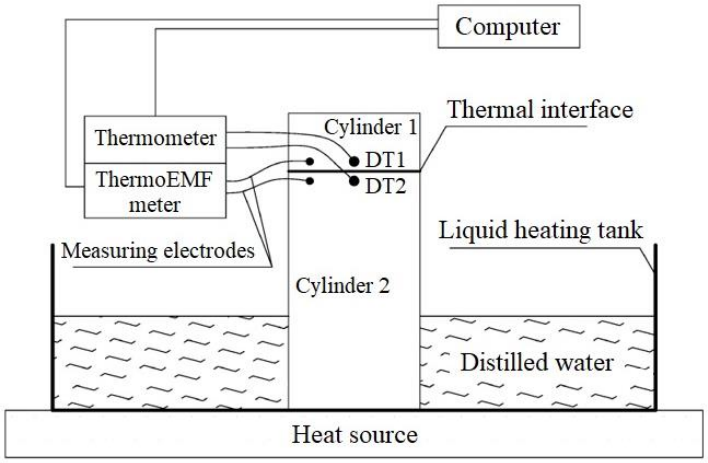

Fig.7. Schematic of the experimental setup

To measure the temperature difference at the boundaries of the thermal interface layer, two platinum rhodium-platinum rhodium thermocouples DT1 and DT2 (manufactured by Elemer R&D company, Russia) connected according to a differential circuit were used [33, 34]. The connection was carried out in such a way that the distance from the thermocouple to the boundary of contact between the body of the power semiconductor device and the heat sink was minimal. In addition, a high-accuracy millivoltmeter was connected to both cylinders to measure thermoEMF. The silicone heat-conducting paste was placed in the gap between the cylinders. The recalculated value of the temperature difference from thermoEMF and the value of the temperature difference measured using thermocouples is shown in Figure 8. Figure 8 shows that the deviation of the two dependences does not exceed 6 %, and the temperature difference caused by the high thermal resistance of the thermal interface, even in steady state, exceeds the heat loss in the environment.

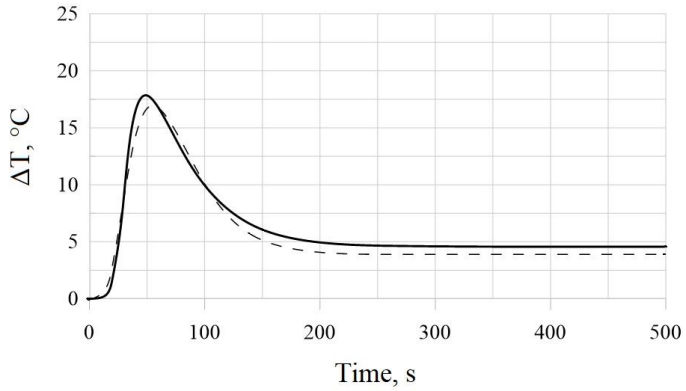

Fig.8. Dependence of the temperature difference at the boundary of the thermal interface of two samples on time, (solid line - measured by thermocouples, dotted line - measured using thermoEMF)

Further research was carried out using a cooling radiator made of AlSi12 silumin alloy, SHCP-8 thermal paste, and a KT808 semiconductor transistor in a TO-220 electronic package. The TO-220 package is widely used in the production of power semiconductor technology. Electronic package material is copper, while package coating material is tin. Platinum rhodium-platinum rhodium thermocouples DT1 and DT2 were attached to the body of the TO-220 power element and to the heat sink through a heat-conducting glue, connected in a differential circuit [35]. The connection was carried out in such a way that the distance from the thermocouple to the boundary of contact between the body of the power device and the cooling heat sink

was minimal. The dependences of the temperature difference between the body of the power device and the heat sink, obtained by using thermocouples and by recalculating the thermoEMF are shown in Figure 9.

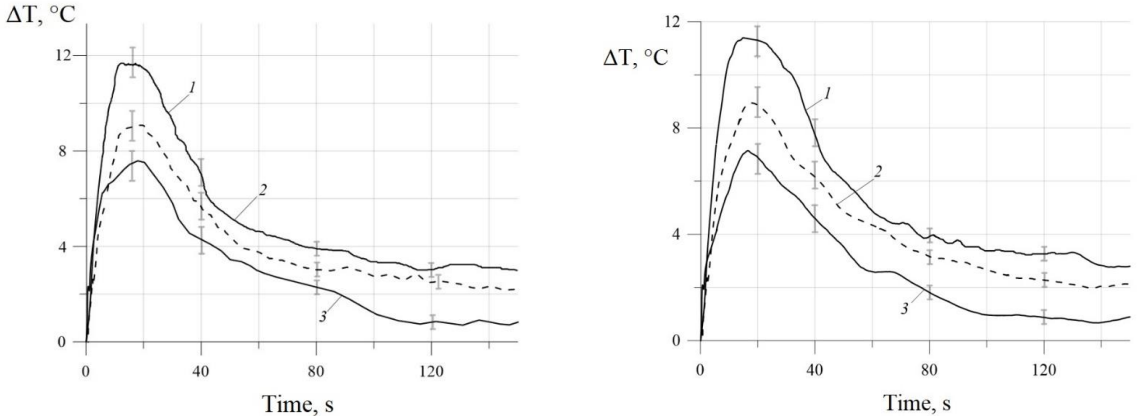

Fig.9. Dependences of the temperature difference between the body of the power device and the cooling heat sink on time; (a) obtained by using thermocouples, (b) obtained by recalculating thermos EMF, *curve 1* - without a thermal interface; *curve 2* - with partially applied thermal interface (50 %); *curve 3* - with applied thermal interface

The results of experimental studies of the dependence of thermoEMF on the area of coverage of the body of the power element with a thermal interface show an almost linear dependence; with an increase in the area of coverage, the thermoEMF linearly decreases (Fig. 10). Confidence interval does not exceed 8 %.

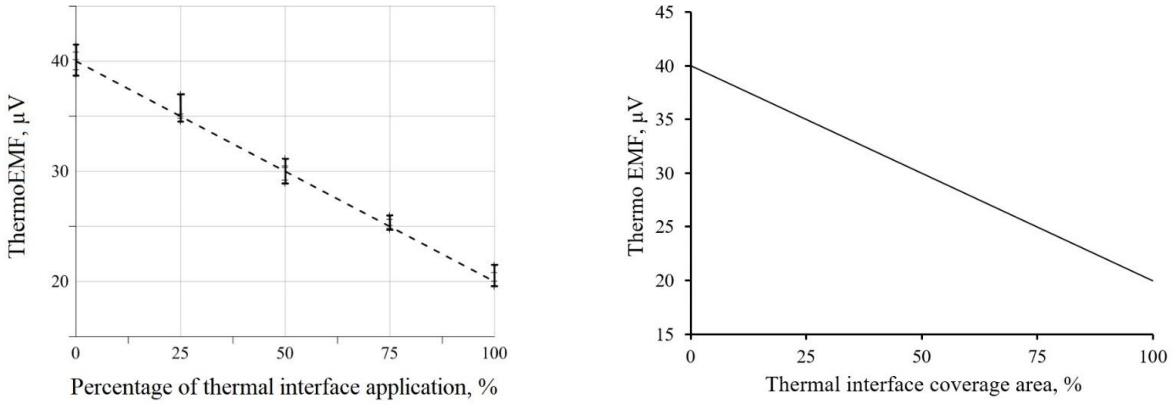

Fig.10. Dependence of thermoEMF on: (a) percentage of thermal interface application, and on (b) on the thermal interface coverage area of the body of the power semiconductor element

The obtained linear dependence of thermoEMF on the area of coverage of the body of the power element with a thermal interface makes it possible to use the thermoelectric method to monitor the thermal resistance of the system of the body of the power semiconductor element - thermal interface - cooling radiator. The result of the theoretical calculation of the thermal resistance Rs, using formula (13) is shown in Fig. 11, where the obtained values of the thermal resistance were obtained using linear filtering.

Variations in thermal resistance are characterized by a random error caused by temperature fluctuations during the experiment. The measured average thermal resistance of the thermal interface is (0.002721±0.0002) K/W, while the calculated value is 0.0025429 K/W, which implies that the difference between the calculated and experimental values does not exceed 8%.

When using heat sinks or devices in electronic housings made of other materials, it is necessary to first determine the calibration dependence of thermoEMF on the area covered by the thermal interface of the power element housing. It should be noted that the thermoelectric monitoring method can be used directly during the operation of electronic equipment.

.

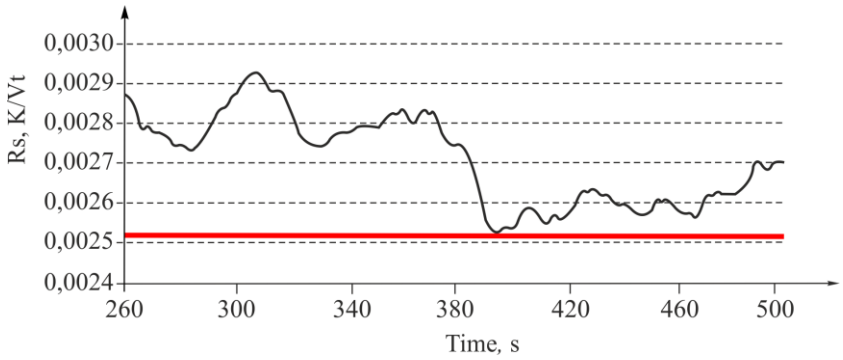

Fig.11. Thermal resistance of the thermal interface in steady state

5. Conclusion

The thermoelectric method is proposed, for the purpose of non-destructive testing of the thermal resistance of the system (electronic package of power semiconductor element - thermal interface - cooling radiator). This method, in comparison with the method of measuring the temperature difference using temperature sensors, gives a more reliable result due to the absence of the influence of the thermal resistance of thermal sensors when installed on the body of the power semiconductor device and the cooling heat sink, as well as the absence of thermal inertia of the temperature sensors. The proposed method makes it possible to monitor thermal resistance with an error of less than 8 %.

Laboratory tests in the application of the proposed method confirmed the correctness of the construction of the mathematical model and the theoretical justification of the method. The practical operation of the developed method for monitoring the thermophysical characteristics of the thermal interface showed that the developed monitoring system has high accuracy and repeatability.

References

1 Liu Y., Li J. A protocol to further improve the thermal conductivity of silicone-matrix thermal interface material with nano-fillers. *Thermochimica Acta,* 2022, Vol. 708, pp. 179136. doi: 10.1016/j.tca.2021.179136

2 Swamy M.C.K., Satyanarayan. A Review of Performance and Characterization of Conventional and Promising Thermal Interface Materials for Electronic Package Applications. *Journal of Electronic Materials*, 2019, Vol. 48, pp. 7623–7634. doi: 10.1007/S11664-019-07623-7

3 Zhang Y., Ma J., Wei N., Yanga J., Pei Q.-X. Recent progress in the development of thermal interface materials: a review. *Physical Chemistry Chemical Physics*, 2021, Vol. 23, pp. 753-776. doi: 10.1039/d0cp05514j

4 Xing W., Xu Y., Song C., Deng T. Recent Advances in Thermal Interface Materials for Thermal Management of High-Power Electronics. *Nanomaterials*, 2022, Vol. 12, No.19, pp.3365. doi: 10.3390/nano12193365

5 Prasher R. Thermal Interface Materials: Historical Perspective, Status, and Future Directions, *Proceedings of the IEEE*, 2006, Vol. 94, No. 8, pp. 1571-1586. doi: 10.1109/JPROC.2006.879796

6 Esau D. Thermal Paste Application. *SEMIKRON INTERNATIONAL GmbH*. 2010, Rev. 7, 6 p.

7 Schulz M. Thermal Interface – An Inconvenient Truth. *Article Bodo's Power Systems*, 2010, Vol. 6, pp. 1-4.

8 Chung, D.D.L. Thermal interface materials. *Journal of Materials Engineering and Performance*, 2001, Vol. 10, pp. 56–59. doi: 10.1361/105994901770345358

9 Becker G., Lee C., Lin Z. Thermal conductivity in advanced chips: Emerging generation of thermal greases offers advantages. *Advanced Packaging*, 2005, Vol. 14, No. 7, 14 p.

10 Roy C.K., Bhavnani S., Hamilton M.C., Johnson R.W., Knight R.W., Harris D.K. Thermal performance of low melting temperature alloys at the interface between dissimilar materials. *Applied Thermal Engineering*, 2016, Vol. 99, pp. 72-79. doi: 10.1016/j.applthermaleng.2016.01.036.

11 GOST 19783-74 Organo-silicon heat-conducting paste. Specifications. Date of introduction: 01.01.1975. Official publication Moscow: IPK Publishing House of Standards, 1996. 11 p. [in Russian]

12 Drexhage P., Beckedahl P. Thermal Paste Application. *SEMIKRON INTERNATIONAL GmbH*, 2018, Rev. 7, 24 p.

13 Freyberg M., Daucher C. Application of thermal paste for Power Modules without base plate. *Semikron International GmbH*, 1999, 9 p.

14 Shishkin R. Development of the production technology of a new highly effective thermal grease. *The International Journal of Advanced Manufacturing Technology*, 2023, Vol. 126, pp. 709-717. doi: 10.1007/s00170-023-11149-y

15 Guo X, Cheng S, Cai W, Zhang Y, Zhang X. A review of carbon-based thermal interface materials: mechanism, thermal measurements and thermal properties. *Materials & Design*, 2021, Vol. 209, pp. 109936. doi: 10.1016/j.matdes.2021.109936

16 Zhang Y., Ma J., Wei N., Yang J., Pei Q.X. Recent progress in the development of thermal interface materials: a review. *Physical Chemistry Chemical Physics*, 2021, Vol. 23, pp. 753–776. doi: 10.1039/d0cp05514j.

17 Sarvar F., Whalley D.C., Conway P.P. Thermal Interface Materials - A Review of the State of the Art. *Proc. of the 1st Electronic System integration Technology Conference*, 2006, pp. 1292-1302. doi: 10.1109/ESTC.2006.280178.

18 Otiaba K.C., Ekere N.N., Bhatti R.S., Mallik S., Alam M.O., Amalu E.H. Thermal interface materials for automotive electronic control unit: Trends, technology and R&D challenges. *Microelectronics Reliability*, 2011, Vol. 51, No. 12, pp. 2031-2043. doi: 10.1016/j.microrel.2011.05.001.

19 Smirnov V.I., Sergeev V.A., Gavrikov A.A., Shorin A.M. Modulation method for measuring thermal impedance components of semiconductor devices. *Microelectronics Reliability*, 2018, Vol. 80, pp. 205–212.

20 Smirnov V.I., Sergeev V.A., Gavrikov A.A., Shorin A.M. Thermal impedance meter for power MOSFET and IGBT transistors. *Proceeding of the IEEE Transactions on Power Electronics*, 2018. Vol. 33, No. 7, pp. 6211-6216.

21 Smirnov V.I., Sergeev V.A., Gavrikov A.A., Kulikov A.A., Shorin A.M. Comparative analysis of standard and modulation methods for measuring thermal resistance of power bipolar transistors. *Journal of Radio Electronics*, 2019, No. 1, pp. 1-14. [in Russian]

22 Smirnov V.I., Sergeev V.A., Gavrikov A.A., Kulikov A.A. The study of current localization in solar cells during the thermal resistance measurements. *Moscow Workshop on Electronic and Networking Technologies 2020 – Proceedings*, 2020, pp. 9067386.

23 Smirnov V.I., Sergeev V., Gavrikov A., Kulikov A. Measuring thermal resistance of gan hemts using modulation method. *Proceeding of the IEEE Transactions on Electron Devices*, 2020, Vol. 67, No. 10, pp. 4112-4117.

24 Abouellail A.A., Obach I.I., Soldatov A.A., Soldatov A.I. Surface inspection problems in thermoelectric testing. *Proc. of the MATEC Web of Conferences*, 2017, Vol. 102, pp. 01001. doi: 10.1051/matecconf/201710201001.

25 Soldatov A.I., Soldatov A.A., Sorokin P.V., Loginov E.L., Abouellail A.A., Kozhemyak O.A., Bortalevich S.I. Control system for device «thermotest». *Proceeding of the Intern. Siberian Conf. on Control and Communications (SIBCON)*, 2016, pp. 1–5. doi: 10.1109/SIBCON.2016.7491869.

26 Carreon H., Nagy P.B., Blodgett M. Thermoelectric nondestructive evaluation of residual stress in shot-peened metals. *AIP Conference Proceedings*, 2002, Vol. 615, No. 1, pp. 1667–167. doi: 10.1063/1.1472993.

27 Carreon H., Nagy P.B., Blodgett M. Thermoelectric nondestructive evaluation of residual stress in shot-peened metals. *Research in Nondestructive Evaluation*, 2002, Vol. 14, pp. 59-80. doi: 10.1007/s00164-002-0001-x.

28 Anatychuk L.I. On the discovery of thermoelectricity by volta. *Journal of thermoelectricity*, 2004. No. 2. pp. 5–10.

29 Lasance C.J.M. *The Seebeck Coefficient*. Available at: https://www.electronics-cooling.com/2006/11/the-seebeck-coefficient/ (accessed 7 February 2023).

30 Vasil'ev, I.M., Soldatov, A.A., Dement'ev, A.A., Soldatov, A.I. Control of Quality of Applying Heat-Conducting Compound. *Russian Journal of Nondestructive Testing*, 2020, Vol. 56, No. 3, pp. 284–290. doi: 10.1134/S1061830920030110.

31 Vasiliev I.M., Soldatov A.I., Abouellail A.A., Kostina M.A., Soldatov A.A., Soldatov D.A., Bortalevich S. Thermoelectric Quality Control of the Application of Heat-Conducting Compound. *Studies in Systems, Decision and Control*, 2021, Vol. 351, pp. 59–68. doi: 10.1007/978-3-030-68103-6_6.

32 Vasiliev I.M., Soldatov, A.I., Dementiev, A.A., Soldatov A.A., Abouellail, A.A. Automatic device for testing thermal resistance with thermoelectric effect. *Material Science Forum*, 2020, No. 4, pp. 154–156. doi: 10.1088/1742-6596/1499/1/012047.

33 Hu J., Nagy P.B. On the role of interface imperfections in thermoelectric nondestructive materials characterization. *Applied Physics Letters*, 1998, Vol. 73, pp. 467-469. doi: http://dx.doi.org/10.1063/1.121902.

34 Soldatov, A.I., Soldatov A.A., Kostina M.A., Kozhemyak O.A. Experimental Studies of Thermoelectric Characteristics of Plastically Deformed Steels ST3, 08KP and 12H18N10T. *Key Engineering Materials*, 2016, Vol. 685, pp. 310–314. doi:10.4028/www.scientific.net/kem.685.310.

35 Soldatov A.I., Soldatov A.A., Sorokin P.V., Abouellail A.A., Obach I.I., Bortalevich V.Y., Shinyakov Y.A., Sukhorukov M.P. An experimental setup for studying electric characteristics of thermocouples. *Proceeding of the Intern. Siberian Conf. on Control and Communications (SIBCON)*, 2017, pp. 1-4. doi: 10.1109/SIBCON.2017.7998534.

Article accepted for publication 09.06.2023

DOI 10.31489/2023No3/62-69

UDC 691.175; 678.8

STUDY OF PREPREGS LIFETIME BASED ON EPOXY RESIN WITH AROMATIC AMINE HARDENER

Baiserikov B.M.[1,3], Yermakhanova A.M.[1], Ismailov M.B.[1], Kenzhegulov A.K.[1,2], Kenzhaliyev B.K.[2]

[1] JSC "National Center of Space Research and Technology", Almaty, Kazakhstan
[2] Satbayev University, JSC Institute of Metallurgy and Ore Beneification, Almaty, Kazakhstan
[3] Satbayev University, Almaty, Kazakhstan

Today, there is a steady trend in the use of carbon fiber-reinforced plastics in the aerospace and defense industries, mainly based on using pre-impregnated semi-finished products - prepregs. Producing carbon fiber parts from prepregs often requires a long manufacturing time, during which the prepreg must maintain its performance properties. Therefore, one of the main characteristics of prepreg is its viability. This work developed a suitable resin composition with optimized properties and a methodology for studying the viability of prepreg samples, based on determining the stickiness and degree of curing of the prepreg depending on storage time. The influence of prepreg storage time on the strength characteristics of cured laminates was studied. Prepreg samples with long-term viability of up to 60 days were obtained. The experimental data obtained are of practical significance in the industrial production of carbon fiber products, as they establish a connection between the performance properties of the prepreg and storage time.

Keywords: polymeric composite material, prepregs, resin, hardener, polymeric matrix, carbon fiber, viability.

1. Introduction

The use of carbon fiber materials is growing more urgent in the aviation and aerospace industries. Compared to conventional structural materials in the form of metal alloys, carbon fiber-reinforced plastics provide the high-strength/weight ratio. The specific strength of carbon fiber reinforced plastic reaches up to 53-112 km, aluminum alloys up to 21 km, steels up to 27 km, titanium alloys up to 28 km [1-5].

The present-day production of aerospace products from carbon fiber-reinforced plastics is mainly based on prepreg technology. The core of this technology is to obtain a pre-impregnated reinforcement fiber by the system of thermally-reactive matrices- prepreg. The use of prepreg provides an opportunity to obtain the large-sized parts and guarantees a stable and good quality of product. However, this technology results in long production cycles. The manufacture of composite parts from prepregs often requires time for laying and preparation over several days or even weeks, during which the chemical reactions after completion of which the prepreg loses all of its performance properties take place in the prepreg, that adversely affect the strength properties of the final prepreg product. Therefore, one of the main characteristics of prepreg is its viability.

The viability of prepreg is the preservation of its technological properties (adhesiveness, drapability) during storage until processing (from several days to several months) [6-8]. As evidenced by analysis of scientific publications and patents, viability of the prepreg directly depends on the type of hardeners used. The use of anhydride hardeners makes it possible to obtain prepregs with viability of up to 5 days, hardeners, binders with aromatic amine hardeners diaminodiphenylsulfone and dicyandiamide have the greatest viability of up to 360 days [9-12].

In this study, a resin composition suitable for prepregs with optimized properties for prepreg production was developed. It is expected that change in the adhesiveness of prepreg due to aging will be its main disadvantage, which directly affects the quality of manufacture and the final mechanical properties. The works [13-17] contains the studies of the effect of prepreg storage time on physical properties, such as adhesiveness, degree of cure, volatile matter content, jelling time, viscosity, establish a good correlation between storage aging time when stored and conversion in curing, which indicates a decrease in the generated reaction heat, fluidity, and increase in the degree of curing, viscosity. However, the prepreg

composition is often not reported, that is crucial for a substantial understanding of the prepreg properties dependence on storage time.

Furthermore, most references indicate a change in adhesiveness, but there is still insufficient data on the effect on laminate quality [18-20], there is no generalizing disadvantage of changing prepreg properties in the literature. In that regard, the study of mechanical properties and quality of laminates depending on viability is of high research interest.

The purpose of work is a study of prepregs viability based on epoxy resin with aromatic amine hardener to assess manufacturability and determination the dependence of adhesiveness, degree of cure and mechanical properties on the prepreg storage time.

2. Experimental procedure

The prepregs used in the study have been obtained by impregnating a one-directional carbon woven reinforcing filler 12K-300-230 with an epoxy binder with the following composition: 100 weight parts modified epoxy-diane resin; 20 weight parts aromatic amine hardener 4,4'- diamino diphenyl sulfone, 10 weight parts plasticizer tricresyl phosphate [21-24].

The epoxy resin and hardener were loaded into a 300 ml beaker and combined under intensive stirring at 500 rpm and 100 °C in a magnetic stirrer for 30 minutes, then a plasticizer was added to reduce the viscosity. The components were mixed until a homogeneous mass was obtained.

The prepreg impregnation was performed on a laboratory prepreg preparation unit (Figure1), by passing the carbon fabric through the binder bath heated to a temperature of 60 °C while pulling the fabric at a speed of 0.5 m/min. The prepreg samples with a fabric/resin ratio of 65/35 have been obtained (Figure 2). Ingredient control the mass ratio of fabric to resin in the prepreg is adjusted by changing the thickness of the gap between the squeeze rollers to remove excess resin from the impregnated fabric. Fabric wetting width 300 mm. The ratio 65/35 was obtained with a gap thickness of 0.3 mm.

Fig.1. Laboratory unit for preimpregnation

a) *b)*

Fig.2. Roll of experimental prepreg sample (a), experimental prepreg sample (b)

.

There is no standard method for determining the viability of prepregs, therefore, this article discusses various methods widely used in the global industry. The viability of prepreg samples has been determined by evaluating its adhesiveness, degree of cure, and strength characteristics of cured prepreg laminates. The samples were stored at room temperature 25 ± 1 °C. The prepreg samples have been aged under ambient conditions and tested periodically. The adhesiveness s is an important feasture of prepreg, the loss of which indicates the expiry of its viability time.

The sounding method was used to measure adhesiveness. The adhesive capacity of the material to the surface of the probe was determined under the ASTM D2979 standard [25]. The sample tests for adhesiveness have been performed on a texture/mechanical properties analyzer with TA. XTplus Stable Micro Systems sensitive force sensor. A diagram of measuring is shown in Figure 3.

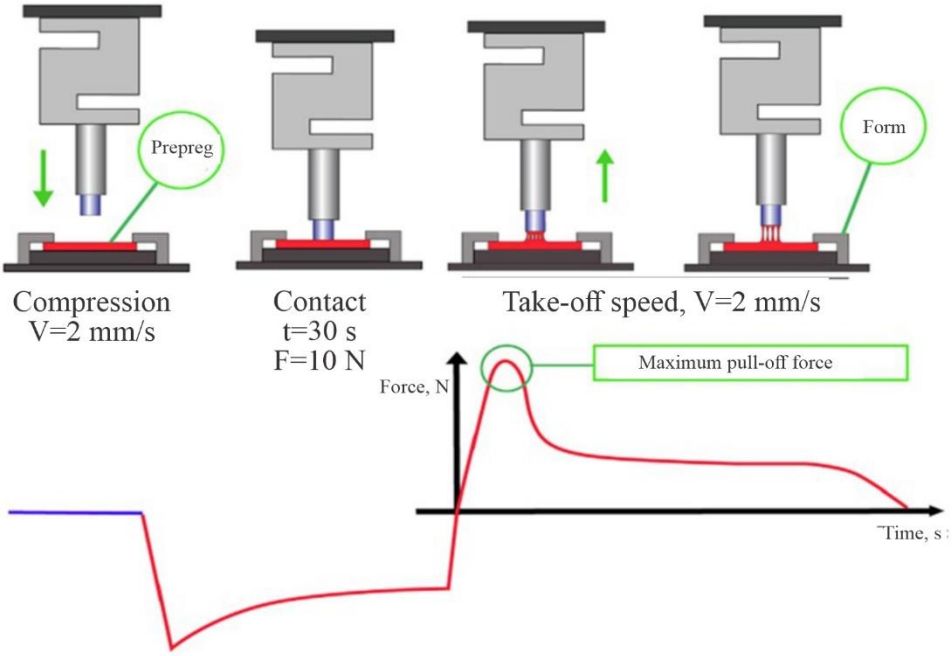

Fig.3. Scheme of measuring the adhesiveness of prepreg samples

The principle of this method is measuring the adhesiveness of adhesive-like materials, which include epoxy prepregs using a probe that separates under driving force the prepreg (adhesive) from the cylinder (substrate). The adhesiveness was measured as follows. The test sample was placed on a cylinder with a hole. A weight was placed on top of the sample for contact pressure. The testing machine drives the probe and returns the probe to its original position after contact with the sample, measuring the force required to separate (detach) the probe from the prepreg. The adhesiveness is expressed as the maximum value of this force. One of the indicators for assessing the viability, in addition to the adhesiveness of the prepreg, is its degree of cure. Since it is important to have data on the degree to which prepregs cure and lose its adhesiveness and draping properties [26].

The degree of cure of the tested (partially cured) prepreg is determined by the ratio of its heat of reaction to the total heat of reaction of the uncured prepreg. Knowing the heat of reaction of 100% unreacted material, it is possible to calculate the degree of curing of the sample using the following equation:

$$\alpha = \left(1 - \frac{H_S}{H_T}\right) * 100 \quad (1)$$

where H_S – total heat of reaction of the tested (partially cured) prepreg J/g; H_T – total heat of reaction of uncured prepreg J/g [27].

The thermal effect of the curing process was studied on a DSC131 EVO Setaram differential scanning calorimeter in the temperature range of 25-175 °C with the heating rate of 10 °C/min.

To study the effect of prepreg storage time on the strength characteristics of cured laminates, samples of carbon fiber reinforced plastic have been obtained from 8 layers of prepreg in the form of plates. For obtaining the prepreg laminates, a hand-molding method with subsequent vacuum treatment evacuation was employed. From the obtained carbon fiber laminates, the samples for tensile tests (GOST 32656-2014) with dimensions 250 x 25 x 2 mm and compression (GOST 33519-2015)] with dimensions 150 x 15 x 2 mm were prepared. The samples were tested on RMG-100MG4 electromechanical testing machine.

3. Results and discussion

The dependence of the degree of cure on the storage time of prepreg was studied. To calculate the degree of cure of the testing samples, the total heat of reaction of the uncured prepreg was determined (Figure 4). As shown by the Figure 4, the total reaction heat of the uncured prepreg was H_T=1024 J/g. The heat release reaction of the sample starts on the fifth minute, the duration of the exothermic reaction is about 80 minutes.

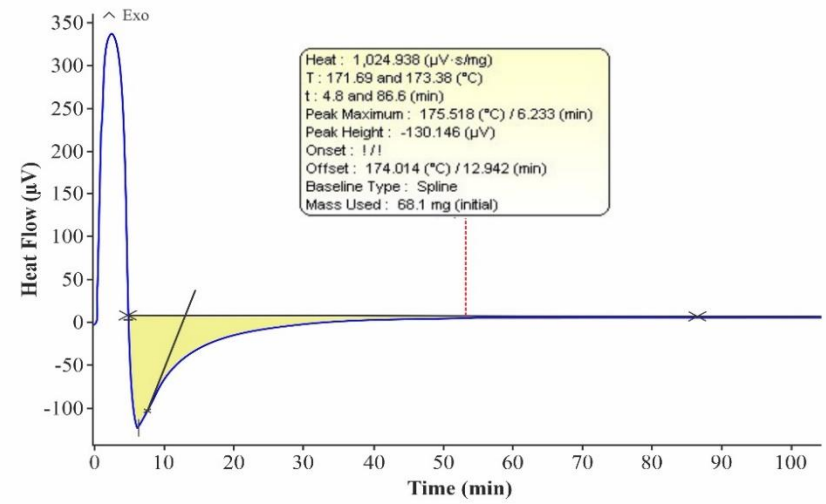

Fig.4. Total reaction heat of the uncured prepreg

Next, the heat of the curing reaction of prepreg samples after storage for up to 60 days was determined. By way of example, the figures show the heat of reaction of prepreg samples after storage for 30 (figure 5) and 60 days (Figure 6).

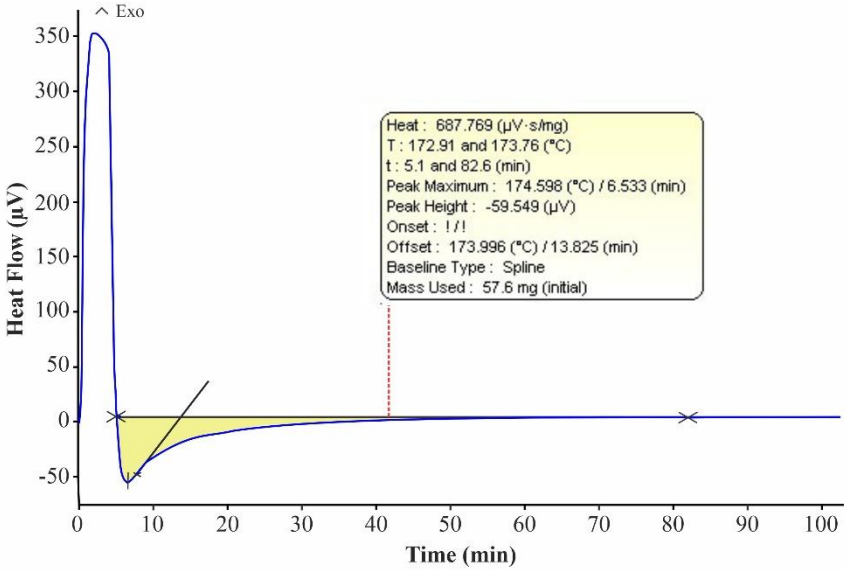

Fig.5. Heat of reaction of the prepreg samples after 30 days storage

.

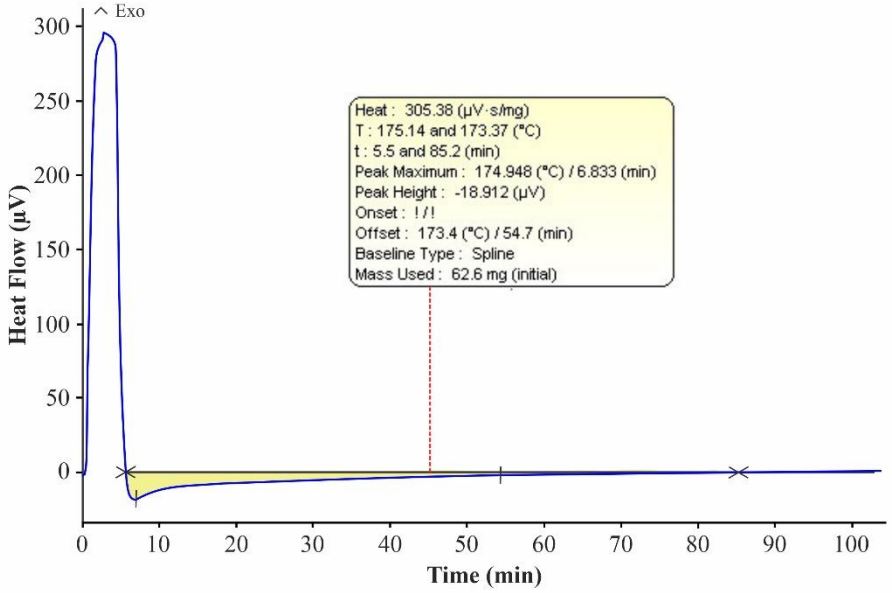

Fig.6. Heat of reaction of the prepreg samples after 60 days storage

According to the experimental results, the total heat of reaction of the prepreg sample after 30 days of storage was H_{S1} = 687 J/g, and the heat of reaction of the prepreg sample after 60 days of storage was H_{S5} = 305 J/g. According to test results, it was found that the peak exotherm decreases with increasing storage time of prepreg samples, this trend is the result of gradual partial curing of the matrix and phase separation during shelf aging. The degree of cure of the partially cured prepreg samples was determined by the ratio of its reaction heat H_s to the total reaction heat of uncured prepreg H_T. The degree of cure α % was calculated according to the formula (1).

The adhesiveness of the prepreg was investigated depending on the storage time at room temperature. The prepreg samples were tested until they lost all of its adhesiveness. The results of the study of the degree of cure and adhesiveness are shown in Figure 7.

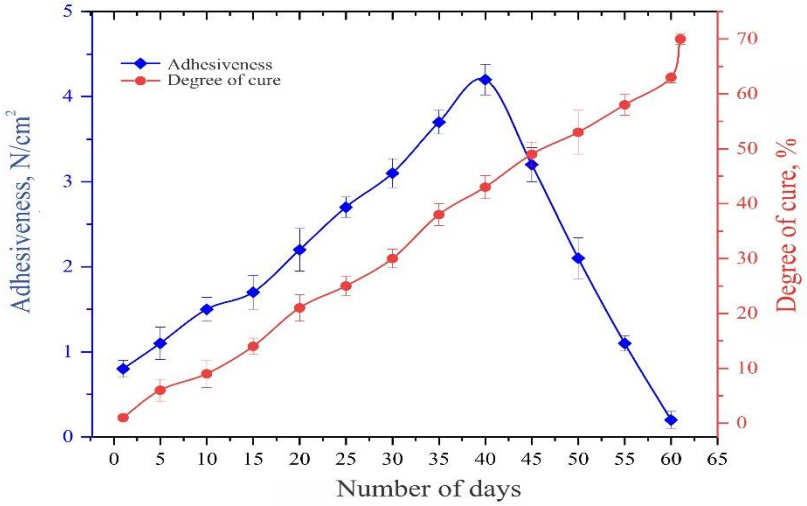

Fig.7. Dependencies of the degree of cure and adhesion of the prepreg samples on storage time

According to results of the study, the prepreg samples have retained its adhesiveness up to 60 days, and the degree of cure of this sample was 63 %. When working with prepregs having a very high adhesiveness of 4.2 N/cm^2, resin distribution and fiber orientation are severely disrupted or clots of reinforcing material are formed. The ratio of components turns out to be inconsistent since the removal of separating foil or substrate

from the prepreg always removes an indefinite amount of resin. A maximum adhesiveness depending on the degree of cure is generated at a conversion of 43 % on day 40 of storage. With further storage a gradual decrease in adhesiveness is observed, such prepreg performance is associated with an increased degree of cure and increased viscosity of the prepreg matrix. After 61 days of storage, the prepreg samples completely lose its adhesiveness with 70 % degree of cure. If the prepregs have no adhesiveness, it means that its preparation has reached too high a stage and their shelf life has expired. Such materials can no longer cure properly.

Therefore, the viability of prepreg samples was determined, which was up to 60 days. This long-term viability achieved with the 4.4-Diaminodiphenylsulfone hardener is caused by availability of amine groups with an aromatic ring; such amines slowly cure epoxide resines at room temperature. At room temperature, the curing practically stops at the reaction with primary amine.

The average shelf life of commercially available prepregs at room temperature is about 30-42 days [28]. In the research work [29], the authors obtained prepregs with a pot life of 4 to 20 days. The authors of [30] report that epoxy prepreg samples containing a cycloaliphatic amine can be stored at room temperature for at least 50 days. In work [31], epoxy prepregs were obtained with the presence of protective polymers in the curing system, which prevented the interaction of the hardener with the resin under storage conditions, allowing the viability of prepregs to be increased to 10 days.

In order to establish the optimal limits of the adhesion indicators, a degree of prepreg samples cure and to identify the relationship between these indicators and strength characteristics of the prepreg laminates, dependence of its strength on storage time have been studied (Figure 8).

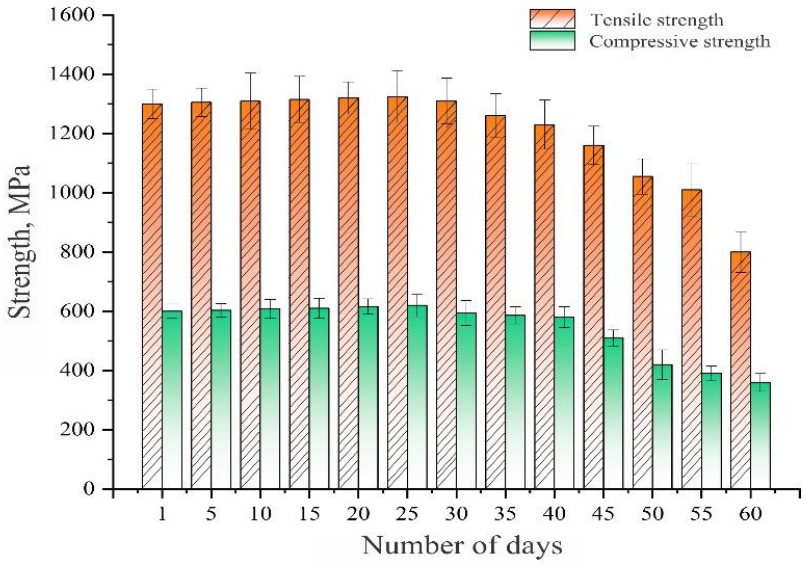

Fig.8. Effect of the prepreg storage time on the strength characteristics of the laminate

The analysis of the results obtained, has demonstrated that within 25 days, the strength has increased by 19 %, with adhesion and curing values were 2.7 N/cm^2 and 25 %, therefore, these parameters can be taken as optimal for prepreg based on epoxy resin with aromatic amine hardener. With further increase in storage time of more than 35 days, strength factor decreases significantly. The reduction of laminates strength is probably due to the fact that when the prepreg degree of cure is increased, the chemical activity of the matrix decreases, which results in decrease in the interlayers hardness between layers at the matrix-matrix interface. This trend of strength reduction after one month of prepreg storage is also observed in the studies [32-34], the authors attribute this to decrease in fluidity and growth of viscosity and degree of cure of the binder in the prepreg.

There are not many similar studies on the effect of storage time on tensile and compressive strength indicators. In [35], prepreg laminates with a tensile strength of 921 MPa were obtained; storing the prepreg for 60 days leads to a decrease in tensile strength by 33 %. As given in [18], based on the results of tensile tests, it can be noted that there are no significant changes in strength after storage time after 60 days, a decrease in strength from 1780 MPa to 1750 MPa.

.

As a result of the data obtained, the dependences of processibility and mechanical properties on prepreg storage time have been established. The degree of cure is constantly increasing throughout the storage time which is associated with a continuous continuation of the cross-linking reaction of the matrix. After 40 days, the adhesiveness gradually decreases, after 45 days there is a significant decrease in adhesivenes, and the degree of cure at this time is about 50 %. This is probably due to the fact that, as in all prepregs with tthermally-reactive matrix with degree of cure 50-60 % resin reaches the gelatinous state (jellification), where the resin behaves as a semi-solid gelling agent, and the adhesiveness reduces [36]. With a degree of cure of $\alpha > 60$ %, the resin gradually transforms into a solid state and the prepreg completely loses its adhesiveness and the running ability to drape.

4. Conclusions

The viability of prepregs based on epoxy resin with diaminodiphenylsulfone hardener was studied using a method to evaluate the adhesiveness, degree of cure, strength of cured laminates as a function of storage time at room temperature. The prepreg samples with viability up to 60 days were obtained. It has been established that an increase in the prepreg curing rate >40 % negatively affects the strength characteristics of the prepreg laminates obtained by reducing the chemical activity of the matrix, which results in decrease in the interlayer hardness between the layers at the matrix-matrix interface. The highest strength values of laminates were obtained from prepreg samples with adhesiveness 2,7 N/cm^2 and degree of cure 25 %, after 25 days of storage. As a result of the data obtained, the dependences of processibility and mechanical properties on prepreg storage time have been established.

Acknowledgments

This study is funded by the Aerospace Committee of the Ministry of Digital Development, Innovations and Aerospace Industry of the Republic of Kazakhstan (Project URN : BR 109019/0221/PCF).

References

1 Nelyub V.A. Technologies for obtaining prepregs. *All materials. Encyclopedic reference book.* 2013, No. 3. pp. 12–17. [in Russian]

2 Perepelkin K.E. *Reinforcing fibers and fibrous polymer composites*. St. Petersburg, Scientific foundations and technologies. 2009, 380 p. [in Russian]

3 Belova N.A. Composite materials based on carbon fibers. *Young scientist*, 2015, No. 24.1, pp. 5–7. [in Russian]

4 Meyirbekov M.N., Ismailov M.B., Manko T.A., Kozis K.V. Study of the influence of rubber on stremgth properties of carbon plastic. *Space Science and Technology*, 2022, Vol. 28, No. 5, pp. 67–74. doi:10.15407/knit2022.05

5 Ospanali A.T., Kenzhegulov A.K., Zhumadilov B.E., Suyundykova G.S., Medyanova B.S., Partizan G., Aliev B.A. Obtaining of carbon nanofibers based on polyacrylonitrile by the method of electrospinning. *Eurasian Physical Technical Journal*, 2020, Vol. 33, No. 1, pp. 35–38. doi:10.31489/2020No1/35-38

6 Ma Y., Gu Y., Li Y., et al. Interlaminar properties of carbon fiber composites laminates with resin transfer molding/prepreg co-curing process. *J. Reinf. Plast. Compos.*, 2014, Vol. 33, pp. 2228 – 2241. doi:10.1177/073168441455706

7 Mangalgiri P.D. Composite materials for aerospace applications. *Bull. Mater. Sci.*, 1999, Vol. 22, pp. 657–664. doi:10.1007/bf02749982

8 Suzuki T., Takahashi J. Prediction of energy intensity of carbon fiber reinforced plastics for massproduced passenger cars. *Proceedings of the 9th Japan International SAMPE Symposium*, Tokyo. 2005, pp.14 – 19.

9 Ashcroft, W.R. *Curing agents for epoxy resins.* Springer. 1993, 37-71 p. doi:10.1007/978-94-011-2932-9_2

10 Olin epoxy, Transportation-Composites (Resins & Systems). Available at: https://olinepoxy.com/industries/transportation/transportation-composites-resins-systems / (March22, 2022)

11 Specialchem company, Epoxy Resins for Adhesives and Sealants. Available at: https://adhesives.specialchem.com/selection-guide/epoxy-resins-for-adhesives-and-sealants/examples-of-elevated-temperature- (March11,2022)

12 Niazi M., Beheshty M.H. A new latent accelerator and study of its effect on physical, mechanical and shelflife of carbon fiber epoxy prepreg. *Iranian Polymer Journal*, 2019, Vol.28, pp.337–346. doi:10.1007/s13726-019-00704-8

13 Ji K.J., Wei C.Y., Deng W.H., et al. Evaluation of glass fibre/epoxy prepreg quality during storage. *Polym. Compos.*, 2002, Vol. 10, pp. 599–604. doi:10.1177/096739110201000803

14 Jones R.W., Yeow N., McClelland J.F. Monitoring ambient-temperature aging of a carbon-fiber/epoxy composite prepreg with photoacoustic spectroscopy. *Compos. Part A.*, 2008, Vol. 39, pp. 965 – 971. doi:10.1016/j.compositesa.2008.03.015

15 Grunenfelder L.K., Nutt S.R. Prepreg age monitoring via differential scanning calorimetry. *J. Reinf. Plast. Compos.*, 2012, Vol. 31, pp. 295–302. doi:10.1177/0731684411431020

16 Gu Y., Li M., Zhang Z, et al. Effects of resin storage aging on rheological property and consolidation of composite laminates. *Polym. Compos.*, 2009, Vol. 30, pp.1081–1090. doi:10.1002/pc.20659

17 Budelmann D., Detampel H., Schmidt C., Meiners D. Interaction of process parameters and material properties with regard to prepreg tack in automated lay-up and draping processes. *Compos. A. Appl. Sci. Manuf.*, 2019, Vol. 117, pp. 308 – 316. doi:10.1016/j.compositesa.2018.12.001

18 Blass D., Kreling S., Dilger K. The impact of prepreg aging on its processability and the postcure mechanical properties of epoxy-based carbon-fiber reinforced plastics. *J Materials: Design and Applications*, 2017, Vol. 231(1-2), pp. 62–72. doi:10.1177/1464420716665413

19 Smith A.W., Endruweit A., Choong G.Y.H., et al. Adaptation of material deposition parameters to account for out-time effects on prepreg tack. *Composites Part A*, 2020, Vol. 133, pp. 105835. doi:10.1016/j.compositesa. 2020.105835

20 Endruweit A., Choong G.Y.H., Ghose S., et al. Characterisation of tack for uni-directional prepreg tape employing a continuous application-and-peel test method. *Compos A Appl. Sci. Manuf.*, 2018, Vol. 114, pp. 295 – 306. doi:10.1016/j.compositesa.2018.08.027

21 Meiirbekov M.N., Ismailov M.B., Manko T.A. The effect of the modification of an epoxy resin by liquid oligomers on the physical-mechanical properties of composites. *Voprosy khimii i khimicheskoi tekhnologii*, 2020, Vol. 3, pp. 122-127. doi:10.32434/0321-4095-2020-130-3-122-127

22 Yermakhanova A.M., Baiserikov B.M., Kenzhegulov A.K., Meiirbekov M.N., Zhumadilov B.Y. Study on methods to improve the mechanical properties of aramid/epoxy composites. *Journal of Elastomers & Plastics*, 2023, Vol. 55, No. 2, pp. 331-346. doi:10.1177/00952443221147645

23 Mustafa M., Ismailov M.B., Sanin A.F. Study on the effect of plasticizers and thermoplastics on the strength and toughness of epoxy resins. *Naukovyi Visnyk Natsionalnoho Hirnychoho Universytetu*, 2020, No. 4, pp. 63-68. doi:10.33271/nvngu/2020-4/063

24 Yermakhanova A.M., Kenzhegulov A.K., Meiirbekov M.N., Samsonenko A.I., Baiserikov B.M. Study of radio transparency and dielectric permittivity of glass- and aramid epoxy composites. *Eurasian Physical Technical Journal*, 2023, Vol.20, No. 2(44), pp. 60-68. doi: 10.31489/2023NO2/70-78

25 ASTM D2979-01 Standard Test Method for Pressure-Sensitive Tack of Adhesives Using an Inverted Probe Machine. Available at: https://www.astm.org/d2979-01.html (March11, 2022)

26 Stark W., Jaunich M., McHugh J. Cure state detection for pre-cured carbon-fibre epoxy prepreg (CFC) using Temperature-Modulated Differential Scanning Calorimetry (TMDSC). *Polymer Testing*, 2013, Vol. 32, No. 7, pp.1261 – 1272. doi:10.1016/j.polymertesting.2013.07.007

27 Hale A. *Thermosets.* Handbook of thermal analysis and calorimetry. 2002, Vol.3, pp. 295 – 354.

28 Schmidt C., Weber P., Hocke T., Denkena, B. Influence of prepreg material quality on carbon fiber reinforced plastic laminates processed by automated fiber placement. *Procedia CIRP*, 2018, Vol. 67, pp. 422–427. doi:10.1016/j.procir.2017.12.236

29 Yang, et al. A novel bio-based, flame retardant and latent imidazole compound-Its synthesis and uses as curing agent for epoxy resins. *Journal of Applied Polymer Science*, 2022, Vol. 139, pp. e53079. doi: 10.1002/app.53079

30 Kuznetsova I.O., Grebeneva T.A. Regulation of the viability of epoxy SMC prepregs. *Bulletin of Science*, 2020, Vol. 2, No. 1(22), pp. 210 – 217. [in Russian]

31 Cheremukhina I.V. Features of diffusion processes when producing prepregs by layer-by-layer application of components. *Vestnik VGUIT*, 2021, Vol. 83, No. 2, pp. 224 – 229. doi:10.20914/2310-1202-2021-2-224-229. [in Russian]

32 Cole K.C., No Ёel D., Hechler J-J., et al. Room-temperature aging of Narmco 5208 carbon-epoxy prepreg. Part II: physical, mechanical, and nondestructive characterization. *Polym. Compos.*, 1991, Vol. 12, pp. 203-212.

33 Scola D.A., Vontell J., Felsen M. Effects of ambient aging of 5245C/graphite prepreg on composition and mechanical properties of fabricated composites. *Polym. Compos.*, 1987, Vol. 8, pp. 244–250.

34 Ji K.J., Wei C.Y., Deng W.H., et al. Evaluation of glass fibre/epoxy prepreg quality during storage. *Polym. Compos.*, 2002, Vol. 10, pp. 599–604. doi:10.1177/096739110201000803

35 Rabby M.M., Das P.P., Rahman M., Vadlamudi V., Raihan R. Prepreg age monitoring and qualitative prediction of mechanical performance of composite using dielectric state variables. *Polymers and Polymer Composites*, 2022, Vol. 30, pp. 09673911221145053. doi:10.1177/09673911221145053

36 *Degree of cure - A104*. Available at: https:// compositeskn.org/KPC/A104 / (March22, 2023)

Article accepted for publication 04.07.2023

.

DOI 10.31489/2023No3/70-79

UDC 621.382: 004.3

DEVELOPMENT OF A MICROCONTROLLER DEVICE FOR REPRODUCING AUDIO INFORMATION

Tussupbekova A.K.*, Afanasyev D.A., Seldyugaev O.B., Karabassov V.A., Alpyssova G.K., Abikenov A.T., Sheinmeier E.V.

Academician E.A.Buketov Karaganda University, Karaganda, Kazakhstan

The paper presents the results of the design, development and manufacture of a microcontroller device for reproducing sound information in the presence of a person. The description of the concept of a microcontroller device and the architecture of the system are given. The technical specification for the manufacture of the device and its software has been compiled. A prototype of the audio information playback device based on Arduino-UNO was made. In order to reduce the cost of one product, the device was upgraded and the ATtiny13A-SU microcontroller was selected as the microcontroller. An electrical principal scheme, a printed circuit board of the device and software for it have been developed. 17 operating audio information playback devices have been manufactured. A technical solution for further improvement of the microcontroller device is proposed.

Keywords: audio bench, microcontroller device, printed circuit board, Arduino-UNO, ATtiny13A-SU, audio information.

1. Introduction

The development of various fields of electronics, computer technology, data collection and communications has created a favorable environment for the development of various areas of technic and technology [1-3]. It is expected that the modern concept of designing and using electronic devices will profoundly change our lives, allowing us to create ubiquitous, distributed, high-performance, high-speed systems that can surprisingly change the way which we interact with the world [2, 3]. There are many commercial, industrial, educational and cultural opportunities for the use of various electronic devices [4-7].

Intelligent electronic control systems can be designed in different ways, but it is reasonable to expect that sensors, actuators and control units will be present in most applications. To do this, embedded hardware platforms can be used to implement these elements, and there are many options available on the market. Among the various platform options, open source platforms are gaining the most popularity among developers. There are currently several good open source platforms. The presence of many research and industrial projects developed using various platforms is a good indicator of which platforms are the most popular. Such platforms include RaspberryPi, BeagleBoard, Arduino, etc.

Compared to other platforms, the Arduino platform has a number of advantages, representing a built-in breadboard designed for projects in the field of electronics, but not necessarily working as a computer. Arduino is used for automation and electronic projects that require repeated execution of certain tasks, and therefore the software and hardware resources of this platform are more limited compared to other platforms.

Most Arduino models are developed using a microcontroller manufactured by Atmel (hereinafter, Microchip), and most of them belong to the ATmega family (8-bit). In addition, this characteristic has two practical meanings: firstly, the Arduino board is usually cheaper; and secondly, it has less computing power than a conventional RaspberryPi or BeagleBoard [8, 9]. Special IDE (IDE – integrated development environment) software developed by the Arduino manufacturer is used for software development.

Nevertheless, the simplicity of Arduino finds its place in many automation and control projects and facilitates the manufacturing process of microcontroller devices. Arduino microcontroller devices are also widely used in the educational process [10], for use in the mining industry [11], for use in smart cities [12], etc. A good example of improving the quality of the infrastructure of Karaganda Buketov University is the development of a device for reproducing a musical composition in the presence of a person. The microcontroller device is equipped with a human detection sensor in a given geometric space for this. The specified musical composition is played, when a person is detected.

Despite the abundance of various electronic devices on such sites as Aliexpress, Ebay, etc., it is impossible to buy an electronic device on these sites that performs all the necessary functions described above. It is not possible to buy a device to play audio information at a certain scheduled time or when the necessary condition or conditions are met.

Today it is impossible to imagine a modern city without recreation areas and benches. Modern technologies make it possible to increase the comfort and standard of living of people. Interactive benches ("talking", "smart", "musical") are becoming popular objects with which residents of the city actively interact [13] and thanks to the reproduced information and cultural aspect have become widespread in Russia (Moscow, Tula, Nizhny Novgorod, etc.) [14, 15] and in far abroad (Great Britain, Sweden, USA, etc.) [16-18].

A number of technical solutions for musical benches with a device for reproducing sound information or sound are shown in Table 1. Thus, despite the widespread use of this idea, in each case the benches have a different design, the reproduced information and schematic execution differ. The difference and novelty of our technical solution is the automatic reproduction of sound information in the presence of a person, increased attention to the vandal-proof characteristics of an electronic device and the possibility of installing this device on any bench.

Table 1. Technical characteristics of a number of sound benches

Brief description of the product, location	The main technical characteristics, Features of this solution	Cost
Solar Audio Bench, National Library of Wales [16]	Activated by two buttons the electronics. Programmable via supplied USB Programming Dongle Audio Output: 1W into 8Ω Speaker. Frequency Range: 75Hz – 20KHz.	Electronic kit - 599 – 767 GBP
Audiorama's sound bench, Lund Stockholm, Sweden [17]	Custom-made bench for sound art in the public space. 4 columns on a bench. The project is under development.	-
Touchme sound bench [18]	Measures intensity of touch between people and turns it into sound.	-
Play panca sound bench, Munich, Germany [19]	Big passive amplifier for enhancing voice from smartphones. Smartphones can put in the long end of the bank and listen to their amplified music.	Sound bench– 31000 Euros
Microcontroller device for reproducing audio information, Karaganda, Kazakhstan	Activation of the melody when an object is located at a distance of 1 meter from the distance sensor. Vandal-proof housing, high moisture protection	50-75 dollars for kit

In this regard, the purpose of this work is to create a microcontroller device for reproducing audio information with the ability to configure various functions performed. The main function of this device is to play a musical melody when a person is detected in a given geometric space. Depending on the function performed, the device can be supplemented with the necessary sensors, a real-time clock, additional non-volatile power, etc.

The areas of use are not limited to the above functions. The information playback device can also be used in a number of other applications, for example, accompanying visual information (painting, sculpture, etc.) with additional information in various languages, reproducing information about a person being in a prohibited area with a loud sound message, etc.

All of the above devices can be implemented on a single platform based on a single microprocessor device.

2. Desing of microcontroller device

Initially, work was carried out to develop the concept of a microcontroller device. The device must perform a number of functions:

1. Register the presence of a person in a certain place of space;
2. Reproduction audio information at the required volume;

.

3. Repeat the execution of functions 1 and 2 in the presence of a person a specified number of times.

To speed up the manufacturing process of a microcontroller device, it was decided to create this device using a number of functional modules:

1. A human presence sensor in a certain place of space;
2. MP3 player for reproduction audio information;
3. Audio frequency amplifier;
4. Microcontroller to coordinate the operation of all other functional elements of the circuit;
5. Necessary power supplies + 12 V, + 5 V.

The JSN-SR04T sensor was chosen as a sensor for detecting the presence of a person in a given space. The ultrasonic element that allows you to send and receive ultrasonic pulses is designed for use at a distance of 20 cm to 450 cm with an accuracy of 2 mm. The measured angle is 75 °. In our case, the operating response distance was chosen to be 1 m.

A simple operation algorithm is selected for the operation of the device. The ultrasonic module, on command from the microcontroller, sends a packet of 7 pulses to determine the distance to the object. Information about the distance to the obstacle comes from the sensor with a delay. The information is embedded in the duration of the pulse coming from the distance sensor. After determining the distance, the microcontroller gives an impulse to start the MP3 player at a distance less than the specified one. After the delay performed on the microcontroller and equal to the playback time of the melody, the cycle repeats.

In accordance with the component base and the algorithm of operation, an electrical functional circuit of a microcontroller device for reproducing audio information was developed. In the first version, the function of the microcontroller was performed by the Arduino Uno board (Fig. 1, a). Work was carried out on it to launch a microcontroller device and check the coordinated operation of the main elements of the circuit.

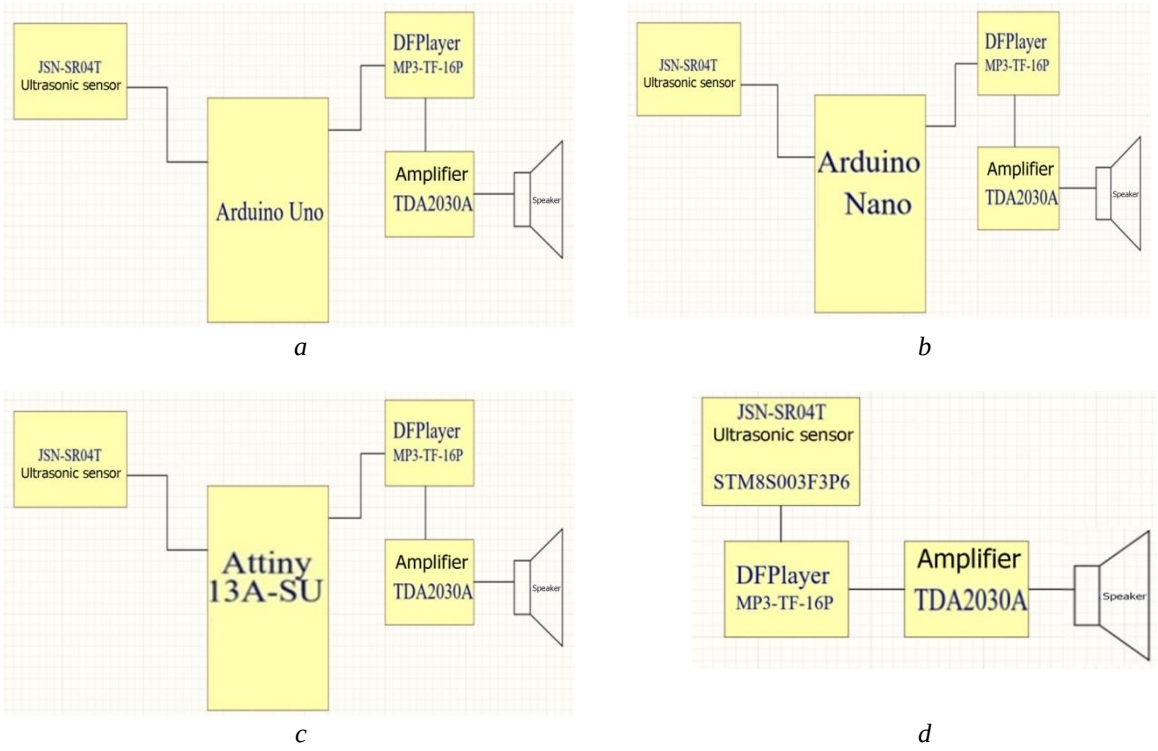

Fig.1. Stages of work on the functional scheme of a microcontroller device for reproducing audio information

The sound quality of this system is determined by the frequency range of the audio frequency amplifier (TDA2030A Audio Power Amplifier Module) of the speaker used for playback (VT-412, 60 W) and MP3 player used for sound reproduction (MP3-TF-16P or DY-SV17F).

The TDA2030A Audio Power Amplifier Module allows you to amplify the audio signal in the entire audio range from 10 Hz to 20 kHz. It has low rates of intermodulation distortion [20]. The sound speaker has

an operating range from 80 Hz to 20 kHz with a nominal operating power of 30 watts. Therefore, the developed system allows you to get high-quality sound.

The prototype of the audio information playback device is made on the basis of the Arduino platform using the Arduino-UNO microcontroller board. This prototype was installed in a gazebo located near Building No. 2 (Faculty of Physics and Technology, 28A Universitetskaya Str., Karaganda) in the period from early April to mid-June 2023.

To reduce the mass of the device, its dimensions and its cost, it was decided to replace the Arduino Uno microcontroller with an Arduino Nano (Fig. 1, b). This concept showed the futility of its development and a number of technical difficulties in implementing the device.

To implement the above algorithm and control the operation of all elements of the device, it is enough to have a microcontroller with 2 pins, a minimum set of functions and the ability to control the operation of external devices in the range from microseconds to seconds. Table 2 shows microcontrollers of various series that meet the requirements for microcontrollers.

Table 2 shows microcontrollers with reprogrammable program memory. Comparing the data and evaluating the advantages and disadvantages allowed us to choose ATtiny13 as the main microcontroller. The choice of this microcontroller was led by the presence of such parameters as high reliability of the microcontroller, availability of technical support from the manufacturer, minimal and sufficient availability of all necessary components, average price and availability of purchase compared to other series of microcontrollers. Therefore, it was decided to replace the Arduino Nano with the ATtiny13A-SU microcontroller, a family of eight-bit microcontrollers from Microchip [21]. A technical specification for the manufacture of the device and software was compiled for the device based on ATtiny13A-SU.

Table 2. Technical characteristics of the main series's of 8-bit microcontrollers

Series/ main types	Main Features	Dignities	Cost
PIC10/ PIC10F200, PIC10F202, PIC10F204, PIC10F206	RISC-microprocessor; 8-Bit Microcontroller; 6/8-Pin Flash-Based, Clock frequency − 4 MHz; Number of pins – 6; Program memory – 256, 512 Bytes	- good continuity of different families; - a single free development environment MPLAB IDE; - compatibility by pins, peripherals, supply voltages, development tools, libraries and stacks of the most popular communication protocols; - a wide range of different controllers with all possible variations of peripherals, memory, number of pins, performance, power and temperature ranges, etc.	$ 0,8 – 1,6
Avr attiny/ ATtiny13, ATtiny25, ATtiny45, ATtiny85	RISC-microprocessor; Core – avr; Data bus width − 8-bit; Clock frequency − 20 MHz; Number of pins – 8; Program memory – 1/2/4/8 kByte	- high performance/power consumption; - convenient programming modes; - wide range of products; - availability of hardware and software support; - high load capacity of the outputs.	$ 1,03 - 2,5
STM8/ STM8S103F3P6	RISC-microprocessor; Core – stm8; 8-Bit Microcontroller; Clock frequency − 16 MHz; Number of pins – 16; Program memory – 8 kByte	- increased reliability; - flexibility of work; - stability of parameters; - advanced options; - price/functionality ratio; - performance; - a promising platform.	$ 2
PADAUK/ PFC161-S08B	RISC-microprocessor; 8-Bit Microcontroller; Clock frequency − 16 MHz; Number of pins – 6; Program memory – 1 kByte	- lowcost	$ 0,066

.

3. Hardware implementation

The technical specification for the manufacture of an electronic board includes the following requirements for the development of a printed circuit board. The overall dimensions of the printed circuit board being developed together with the A325 power supply unit should be placed in a box of the KSC 11-304 brand (distribution box o/n 125*125*50). The board has two holes with a diameter of 3 mm for attaching the board to the KSC 11-304 box. The board is two-layer, with one-sided placement of components. The second surface of the board is a polygon (grounded). The material is FR4. The minimum distance between the conductors is 1 mm, the minimum width of the conductors is 0.5 mm. In narrow places, smaller distances are allowed (it is possible to use jumpers for wiring tracks, no more than 5). The thickness of the copper foil is 35 microns.

The scheme should contain the following components:

- JSN-SR04T ultrasonic distance sensor with serial data transmission;
- DY-SV17F audio module mini mp3 player or DF Player mini;
- Hi-Fi sound amplifier, 18 W on a TDA2030A chip;
- ATtiny13A-SU microcontroller with one indicator LED connected to the ATtiny13A-SU 7 pin, microcontroller restart button and power protection capacitors;
- Voltage stabilizer 5 V, brand 78M05 with input and output capacitors;
- Terminal contacts for connection to the +12V power supply circuit;
- By bringing the grounding to the circuit.

Climatic conditions of use of the device: moisture protection according to the IP43 standard, minimum temperature not less than -10 ° C, maximum temperature 70 ° C.

The functional diagram of the device is shown in Fig. 1, b. The electrical schematic diagram is shown in Figure 2. The main components of the circuit are:

- DY-SV17F audio module mini mp3 player (DD2, Figure. 2);
- ultrasonic distance sensor with serial data transmission JSN-SR04T;
- ATtiny13A-SU microcontroller (DD1, Figure 2);
- converter and voltage stabilizer for 5V based on the 78M05 chip (VT1, Figure 2);
- power supply (12 V, 2 A);
- speaker (60 W).

4. Software implementation

The technical specification for the software includes the following requirements for software development. The program is a code in the C programming language for the AVR microcontroller. The program implements the control of an ultrasonic distance sensor and playback of audio files using an MP3 player. The purpose of the program: the implementation of distance monitoring using an ultrasonic sensor and the playback of audio files using DF Player mini at a given time. General requirements for the program include: the program must be designed for an AVR microcontroller with a specified clock frequency F_CPU 9 kHz; the corresponding pins of the microcontroller must be connected and configured to work with an ultrasonic sensor (TRIG_PIN and ECHO_PIN), DF Player mini (ADKEY_PIN) and LED (LED_PIN).

The functional requirements for software development are as follows:

- When the ping_ultra_sonic() function is called, the distance is measured using an ultrasonic sensor.
- When the enable_dht_player() function is called, DF Player mini is activated.
- The led_init() function initializes the pin of the LED.

Non-functional requirements for software development are as follows:

- Performance requirements such as delays (_delay_us () and _delay_ms ()) and distance (G_DISTANCE) must be defined and configured according to the project requirements.
- The number of repeated triggers (G_MAX_TRIG) must be limited to a certain value.
- The requirements for the maximum delay of music playback (G_MUSIC_DELAY) must be defined.

The architecture of the system is as follows:

- The program is designed for an AVR microcontroller using I/O (input/output) ports for connecting and controlling components.
- Implemented functions for working with an ultrasonic sensor, MP3 player and LED.

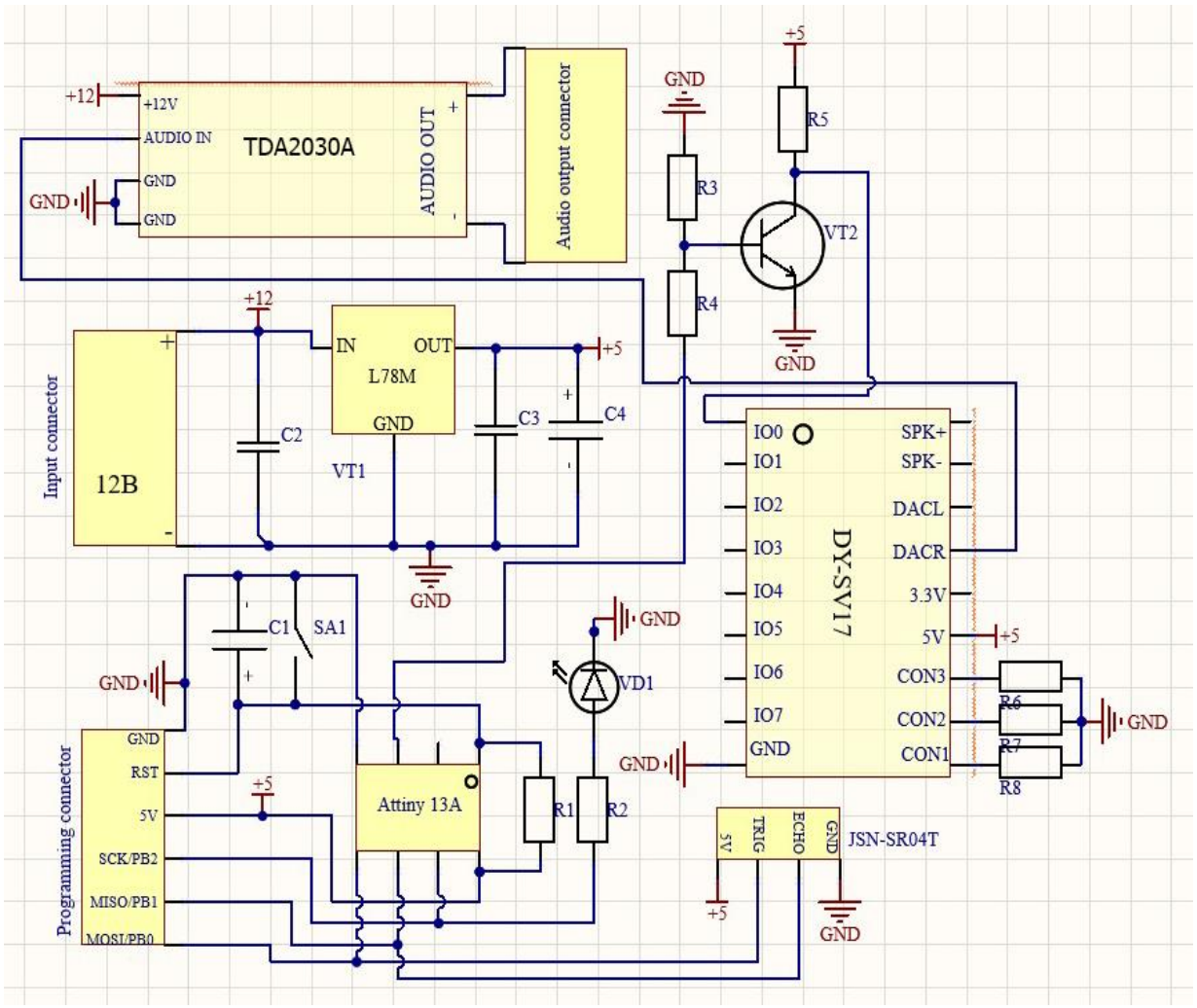

Fig. 2. Electrical principal scheme of a microcontroller device for reproducing audio information

Initially, the software for controlling the operation of the device and the layout of the printed circuit board of the information playback device with ATtiny13A-SU was written. The operation of the electronic device and this software showed poor noise immunity. The main interference, leading to false operation, was associated with the use of a switching power supply used to convert 220 V A.C. to 12 V D.C.

Also, interference was observed from switching power supplies of LED lamps placed on the alley located between the 2nd building of the University (Karaganda, Universitetskaya Str., 28A) and the dormitories of the university (Karaganda, Universitetskaya Str., 28/4). The ground plane was left on the reverse side of the PCB to increase noise immunity. Other methods to reduce the effect of interference on the operation of the electrical circuit have also been used. The algorithm of work was changed and the software for ATtiny13A-SU was also changed to reduce false positives of the device. It has been proposed to trigger sound information when reacquiring information about a distance less than a threshold distance (G_MAX_TRIG= 3 or G_MAX_TRIG= 5, Fig. 3). The algorithm of the program is shown in Figure 3. An application for an author's certificate has been submitted for the software [22].

A printed circuit board of a microcontroller device for reproducing audio information and a program for the ATtiny13A-SU microcontroller have been developed. The printed circuit board is made using photoresist and chemical etching in a mixture of hydrogen peroxide and citric acid. The

.

Sprint Layout 6 program was used to create and lay out printed circuit boards. The program has a simple, intuitive interface and allows you to quickly produce non-complex printed circuit boards.

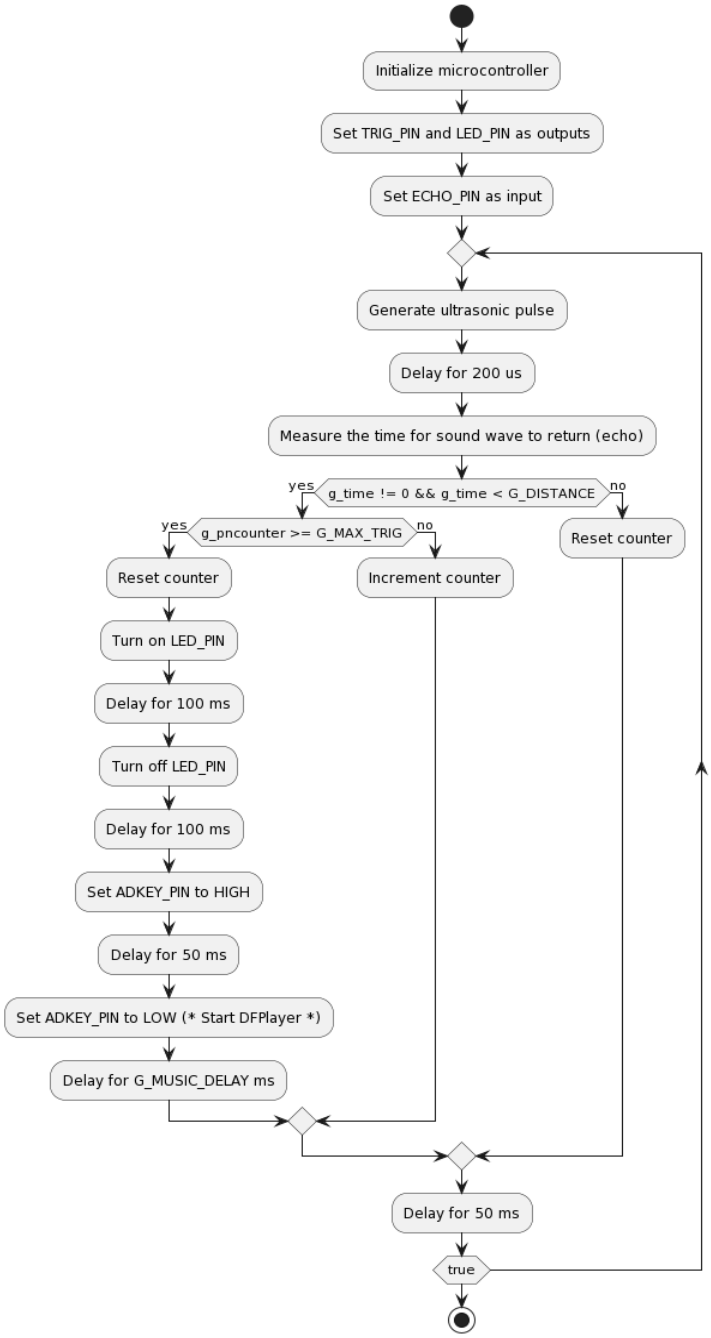

Fig. 3. The algorithm of the program of the audio information playback device (All designations given in the algorithm fully correspond to the designations given in the technical specification for the software)

5. Results and discussions

To transfer the drawing to the foil-clad paper-based laminate and fix the photoresist under the action of ultraviolet light, inverting of Fig. 4, a was carried out. The inverted figure is shown in Fig. 4, b. The connection diagram of the 78M05 converter for 5V voltage stabilizer based is shown in [23]. The appearance of the printed circuit board (PCB) is shown in Fig. 5. To control the elements in the diagram, software has been developed in the C programming language in the Microchip Studio development environment for the ATtiny13A-SU microcontroller. Microchip Studio is an integrated development environment (IDE) for developing and debugging applications of AVR and

SAM microcontrollers. Taking into account the analysis of characteristic malfunctions in the operation of this scheme, the software was upgraded.

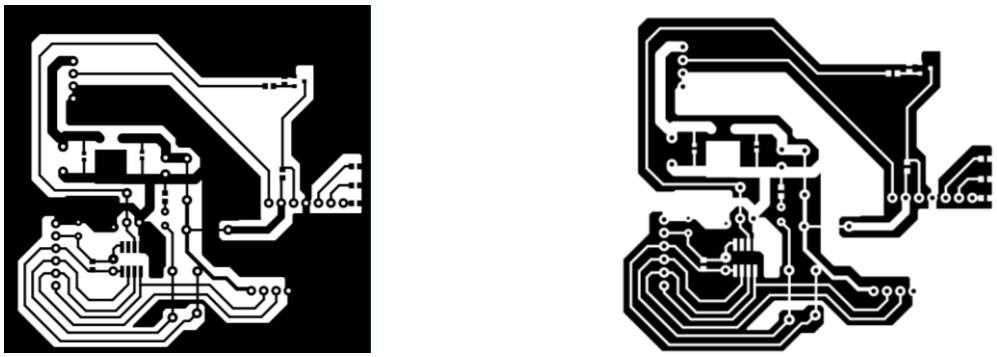

a) b)

Fig. 4. Circuit board drawing image: Non-inverted (a) and inverted (b) PCB drawing

a) b)

Fig. 5. Appearance of the printed circuit board: a) view of the board from below b) view of the finished board from above

Based on the results of work on the microcontroller device, 17 devices were manufactured, placed on benches on the alley located between the 2nd building of the University (Karaganda, Universitetskaya Str., 28A) and the dormitories of the university (Karaganda, Universitetskaya Str., 28/4) (Fig. 6).

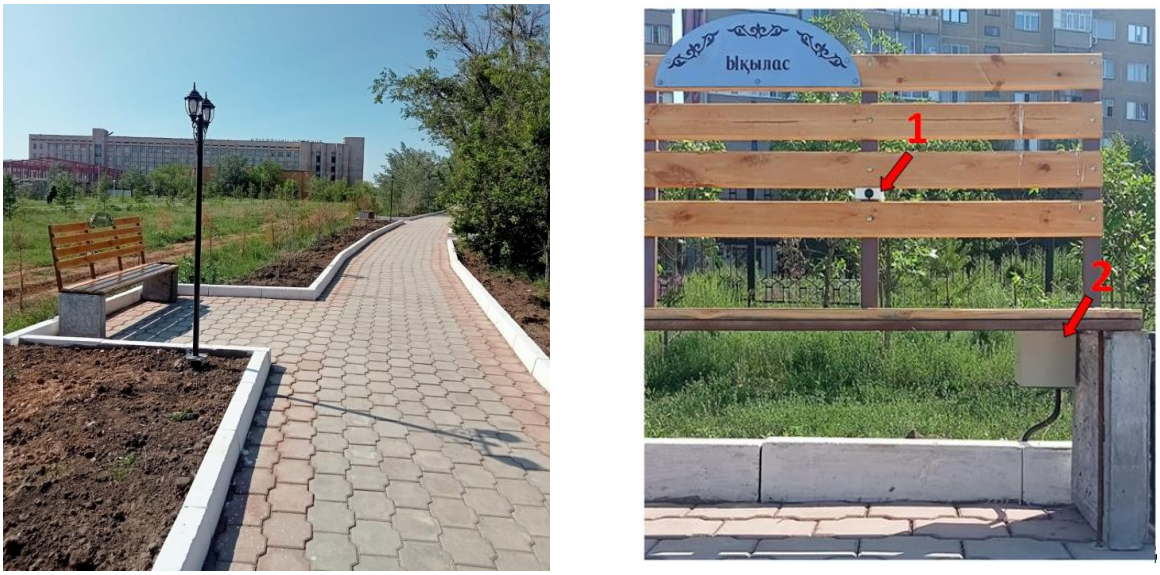

a b

Fig. 6. The appearance of the alley (a) and the place of attachment of the device on the bench (b)

.

The location of the ultrasonic sensor in Figure 6, b is shown by the number 1, the location of the electronic module with the speaker in the vandal-proof box is shown by the number 2. Sound output from the sound column is made from the bottom of the vandal-proof box. This is done to eliminate the possibility of water getting into the electrical part of the circuit. The top and sides are sealed and don't allow water to enter the box. The quality of sound information reproduction is high, which confirmed the operating time of the devices. The devices in the sound alley were connected on May 15, 2023. At the time of submitting the article for publication on September 1, 2023, 17 devices had been operating for 3.5 months 24 hours, 7 days a week without turning off the power. To further improve the microcontroller device, it is proposed to use the resources of the STM8S003F3P6 microcontroller, which is part of the JSN-SR0T4-2.0 ultrasonic distance sensor. In this case, the functional diagram of the microcontroller device will have the form shown in Figure 1, d. The use of this solution reduces the number of components used, reduces the cost of manufacturing and increases the functionality of a microcontroller device for reproducing audio information (the memory capacity of the STM8S003F3P6 program is 8 kilobytes instead of 1 kilobyte for ATtiny13A-SU).

6. Conclusions

1. Work has been carried out to develop the concept of a microcontroller device for reproducing audio information in the presence of a person. The device must perform a number of functions, the main of which are the registration of the presence of a person in a certain place of space and the reproduction of sound information with the necessary volume.

2. Initially, prototyping of a microcontroller device for reproducing audio information based on an Arduino Uno board was carried out. The results of prototyping showed the operability of the chosen technical solution and the possibility of its use in further work.

3. The work went from using the Arduino Uno board to the Arduino Nano board. Then it was decided to develop a microcontroller device for reproducing audio information based on the ATtiny13A-SU microcontroller. The technical specification for the manufacture of the device and the software of this device has been compiled.

4 An electrical principal scheme and a printed circuit board of a microcontroller device for reproducing audio information for the ATtiny13A-SU microcontroller have been developed. The printed circuit board is made using photoresist and chemical etching in a mixture of hydrogen peroxide and citric acid. Software has been developed to control the operation of the audio information playback device. Based on the results of testing the operation of the device, changes were made to the software. 17 devices were manufactured, placed on benches located in the alley on the territory of the E.A. Buketov Karaganda University. At the time the article was submitted to the journal, 17 devices had worked for 3.5 months without breakdowns.

5. Work is underway to improve the microcontroller device for reproducing audio information, aimed at increasing the functionality of the device and reducing its production cost.

Funding

This research is funded by an intra-university grant from the Karaganda E.A. Buketov University (Grant number 24-ВГ-23).

Acknowledgment

The authors of the article are grateful to T. Rakhimgaliyev for participating in the development of software for the ATtiny13A-SU microcontroller and S. Tuleuov for providing mechanical elements printed on a 3D printer and used in audio information reproduction devices.

REFERENCES

1. Lin J.; Yu, W.; Zhang N.; Yang X.; Zhang H.; Zhao W. A Survey on Internet of Things: Architecture, Enabling Technologies, Security and Privacy, and Applications// *IEEE Internet Things J.* 2017, V.4, P.1125–1142. doi:10.1109/JIOT.2017.2683200.

2. Talari S.; Shafie-khah M.; Siano P.; Loia, V.; Tommasetti, A.; Catalão, J.P.S. A Review of Smart Cities Based on the Internet of Things Concept. *Energies*, 2017, V.10, P.421.doi: 10.3390/en10040421.

3. Peixoto J.P.J.; Costa D.G. Wireless visual sensor networks for smart city applications: A relevance-based approach for multiple sinks mobility. *Future Gener. Comput*. Syst. 2017, V.76, P.51–62.doi:10.1016/j.future.2017.05.027.

4. Glasmeier A.K.; Nebiolo M. Thinking about Smart Cities: The Travels of a Policy Idea that Promises a Great Deal, but So Far Has Delivered Modest Results. *Sustainability*, 2016, V.8, P.1122.doi:10.3390/su8111122.

5. Allam Z.; Newman P. Redefining the Smart City: Culture, Metabolism and Governance// *Smart Cities*, 2018, V.1, P.4–25.doi:10.3390/smartcities1010002.

6. Molina B.; Palau, C.E.; Fortino G.; Guerrieri A.; Savaglio C. Empowering smart cities through interoperable Sensor Network Enablers. *Proceedings of the 2014 IEEE International Conference on Systems, Man, and Cybernetics (SMC)*, San Diego, CA, USA, 2014; pp. 7–12.

7. Fortino G.; Savaglio C.; Zhou M. Toward opportunistic services for the industrial Internet of Things. *Proceeding of the 13th IEEE Conference on Automation Science and Engineering (CASE)*, Xi'an, China, 2017, pp.825–830.

8. Official website of the Arduino manufacturer. Date of application 28.12.2022. Available at: https://www.arduino.cc.

9. What is Arduino? Date of application 04.01.2023. Available at: http://arduino.ru/About. [in Russian].

10. El-Abd M. A Review of Embedded Systems Education in the Arduino Age: Lessons Learned and Future Directions. *International Journal Of Engineering Pedagogy*, 2017, Vol.7, Iss.2, pp. 79-93. doi:10.3991/ijep.v7i2.6845.

11. Kim S-M., Choi Yo., Suh J. Applications of the Open-Source Hardware Arduino Platform in the Mining Industry: A Review. *pplied Sciences-Basel*. 2020, Vol.10, Iss.14, No. 5018. doi:10.3390/app10145018.

12. Costa D.G., Duran-Faundez C. Open-Source Electronics Platforms as Enabling Technologies for Smart Cities: Recent Developments and Perspectives. *Electronics*, 2018, Vol.7, Iss.12, No. 404. doi:10.3390/electronics7120404.

13. Kuzmenko B. S., Sklez O. S. IOT engineering: development of a smart bench for urban space improvement. *Young scientist*. 2021, 8.1 (49.1), p. 11-12. [in Russian].

14. Vasilyeva L. An unusual bench. *Science and life*. 2019, 1, p. 110-111. [in Russian].

15. Mironov V. How cities become "smart" with the help of street gadgets. *Urban real estate*, 03.03.2015. Available at: https://realty.rbc.ru/news/577d23139a7947a78ce91720?utm_source=amp_realty_full-link [in Russian].

16. Smith A. Audio Bench – National Library of Wales. (no date) Available at: https://www.blackboxav.co.uk/project/audio-bench-national-library-of-wales/

17. Valeria Naters. Ljudbänken XCHANGE: Jacob Kirkegaard. 25.05.2023. Available at: https://www.lmc.lu.se/en/article/ljudbanken-xchange-jacob-kirkegaard.

18. Official website of the playtronica online store. Date of application 16.04.2023. Available at: https://shop.playtronica.com/products/touchme.

19. A platform for art and design (no date) Available at: https://spazioarte.de/en/products/play-panca-sound-bench.

20. Technical data sheet of the TDA2030A audio power amplifier module. TDA2030A. 18 W hi-fi amplifier and 35 W driver. Doc ID 1459 Rev 2. July 2011. Available at: https://www.thierry-lequeu.fr/

21. Technical data sheet of the ATtiny13A-SU microcontroller. Date of application 06.02.2023. Available at: https://www.microchip.com/en-us/product/attiny13a.

22. Copyright certificate No. 229451. Program for controlling a microcontroller device for reproducing sound information in the presence of a person/ Dulatbekov N.O., Abykenov A.T., Rakhimgaliev T.A., Tussupbekova A.K., Karabassov V.A., Afanasiev D.A. – declared 09.08. 2023. – P. 2. [in Russian].

23. Technical data sheet Precision regulators for 500 mA. Date of application 14.03.2023. Available at: L78MxxAB, L78MxxAC. Precision 500 mA regulators. DocID 2147 Rev. 13. May 2012.

Article accepted for publication 08.08.2023

.

DOI 10.31489/2023No3/80-87

UDC 538.9

ANALYSIS OF CHANGES IN FRACTAL, STATISTICAL AND KINETIC PARAMETERS DURING THE HETEROANNIHILATION OF PARTICLES ON THE SIMULATED STRUCTURALLY INHOMOGENEOUS SURFACES

Karstina S.G.[1], Markova M.P.[2], Moldanazarova U.[1,3]

[1] E.A. Buketov Karagandy University, Karaganda, Kazakhstan, skarstina@mail.ru

[2] Omsk State Technical University, Omsk, Russia, markovamp@mail.ru

[3] University of Liverpool, Liverpool, United Kingdom, psumolda@liverpool.ac.uk

To investigate the mechanisms of interaction of particles on structurally inhomogeneous surfaces, the influence of surface morphology, distribution of interacting particles and their mobility on the mechanisms of ongoing processes, various modeling approaches are widely used. The paper presents the results of comparison of kinetic, statistical and fractal parameters changing in the process of heteroannihilation of particles distributed chaotically and multifractally on a simulated structurally inhomogeneous surface. To simulate the complex behavior of particles in time and space during heteroannihilation with changes in their mobility across the surface and various interaction probabilities, a class IV probabilistic cellular automaton method was applied. Based on the $_{simulation}$ results, it is shown that the interaction probability, initial distribution, and mobility of interacting particles influence the formation of kinetic modes at different iterations of the heteroannihilation process. It was found that a decrease in the mobility of interacting particles leads to a longer preservation of spatial heterogeneity in the system. An increase in the mobility of interacting particles and the probability of their interaction increases the rate of change in the fractal dimensionality and the rate coefficients of heteroannihilation kinetics. Decrease of fractal dimensionality during heteroannihilation is accompanied by decrease of asymmetry and increase of excess characterizing shape and degree of symmetry of distribution of interacting particles. At the same time, large values of asymmetry and excess indicate a significant deviation from the normal distribution of interacting particles on the surface.

Keywords:*heteroannihilation, fractal kinetics, fractal dimensionality, structurally inhomogeneous surface, multifractal analysis, interaction probability.*

1. Introduction

To investigate the interaction mechanisms of particles distributed on structurally inhomogeneous surfaces, various modeling approaches can be used to take into account the distribution of molecules, the interaction radius, the rates of running processes, the surface morphology, thermodynamic and statistical characteristics of the system. Such approaches include methods of fractal and multifractal analysis, which can be used to describe numerically the evolution of complex systems, the mechanisms of processes occurring in them, to identify the factors affecting the behavior of structurally inhomogeneous systems, to establish empirical relationships between fractal parameters and experimentally determined microstructural characteristics, to describe the inhomogeneous fractal object by means of the spectrum of fractal dimensions, to establish connection between geometrical, statistical and kinetic parameters of the system, to identify the type and number of interacting particles in the considered system [1-3]. In addition, fractal and multifractal analysis are widely used in the study of luminescence kinetics and electron excitation energy transfer processes in various media and on surfaces with different topologies [2,4-8], fermentative processes [9], the dynamics of intracellular reactions [10-12], and others.

2. Theory and research methods

Various experimental studies have shown that the kinetics of processes in structurally inhomogeneous media cannot be explained by the law of acting masses because of the anomalous, time-dependent behavior of the rate constant [7]. The key factor in this special behavior is the reaction probability.

For example, according to the approach proposed by Kopelman to describe the kinetics of all diffusion-controlled reactions (reaction order ≥ 2) in inhomogeneous media, the dependence of the rate coefficient on time is described by the equation [7]:

$$k(t) = k_0 \cdot t^{-h} \quad (1)$$

where k_0 is the rate constant in classical kinetics, t is time (t > 0), h is a fractal parameter or measure of system dimensionality (0 ≤ h ≤1). The fractal parameter h in the Kopelman equation increases with increasing concentration of obstacles and particles that undergo transformations in the interaction. In this case, the individual influence of the concentrations of obstacles and interacting particles is cumulative with time. Schnell and Turner, who consider fractal kinetics, the rate coefficient of which follows the Zipf-Mandelbrot distribution, propose another dependence of the rate coefficient on time:

$$\mathrm{k(t)} = \frac{\mathrm{k_0}}{(\mathrm{r+t})^{\mathrm{h}}}, 0 \leq \mathrm{h} \leq 1 \quad (2)$$

In equation (2), the parameters k_0 and h have the same value as in equation (1), and r is a positive constant that represents the time after which the reaction is affected by inhomogeneities in the distribution of molecules, such as clusters of molecules [13]. In addition, a number of works have found that the diffusion anomaly and fractality of kinetics increase with increasing medium density, decreasing the mobility and size of interacting particles or obstacles [14-17]. In accordance with this, in this paper, we compare and contrast the kinetic, statistical and fractal parameters of the processes occurring on the simulated structurally inhomogeneous surface with chaotically and multifractally distributed interacting particles on it. The method used in this work allows to standardize the description of the loss kinetics of interacting particles on surfaces of different structure and morphology.

In this work we consider a model of a surface with inhomogeneously distributed interacting particles of two varieties (*A* и *B*) on it, which form disordered structures of different topology at the initial moment of time and as a result of heteroannihilation. The interest in this kind of systems is related to the need to understand the most general regularities in the behavior of complex nonlinear dynamical systems that reveal a self-consistent tendency towards critical regimes [4-10,18].

Disordered structures on the surface were modeled by introducing the probability of filling the surface nodes with molecules of each variety. The modeled surface and the particles of the two varieties distributed on it were used to simulate the heteroannihilation process described by the equation of the form $A+B\rightarrow 0$. The particles considered in the simulation are analogs of donors and acceptors of electron excitation energy.In modeling the heteroannihilation process, it was assumed that all particles are mobile. Particle mobility was modeled as diffusion motion in a randomly chosen direction. To change the mobility of the particles, the temperature of the simulated surface was varied in the range 193-281K. When distributing the particles over the surface and modeling their mobility, it was taken into account that two particles cannot occupy the same position on the surface at the same time. To simulate the complex behavior of interacting particles on a simulated surface in time and space at a given probability of interaction in the considered temperature interval and to reproduce the processes of heteroannihilation, the method of probabilistic cellular automata of class IV was used [5, 6]. A cellular automaton is a discrete dynamic system whose behavior is completely determined by a set of local rules. The dynamics of cellular automata of class IV depends on the peculiarities of the initial distribution of interacting particles. Some initial distributions may lead to degeneration of the automaton, others to the emergence of a cyclic sequence of states, others to continuously changing activity patterns of interacting particles. In the process, various spatiotemporal structures may emerge, change shape, and die. In the same environment qualitatively different processes with different direction of evolution may arise. Application of cellular automata allows to describe nonlinear processes observed in the system under consideration in discrete language, considering that the measured quantity itself can take a finite set of values. The using of IV class probabilistic cellular automaton method for modeling heteroannihilation processes between particles of different varieties at any iterative step results in simultaneous changes in the state of the whole system. This allowed in the present paper to take into account the connection between the state of the system at the microlevel and changes at the macrolevel during computer modeling. The lattice model was used to simulate random wandering of particles involved in the process of heteroannihilation, energy migration along the donor subsystem and its annihilation in the donor-

.

acceptor pair when two particles of different varieties approach to a distance equal to the interaction radius. The structure of the modeled surface was specified by the number of nodes and lattice dimension. The dynamics of heteroannihilation processes on the modeled surface depended on the temperature of the system under consideration, the activation energy, the initial concentration of particles of each variety, and the nature of their initial distribution on the surface.

An iteration time (*N*), was chosen as the time step for modeling the processes of annihilation occurring on the surface, representing the act of moving a particle to a neighboring free node on the surface and interacting with a particle of a different sort located in the neighboring node of the simulated surface (interaction radius) with a given probability. The position of interacting particles at each step of iteration was varied synchronously with the number of free nodes in the nearest neighboring cells. After that the number of remaining particles of each kind was counted.The analysis of the modeled system at different iterations was performed using the multifractal analysis (MFA) method, which allows estimating the fractal parameters of the matrix, such as the generalized Renyi fractal dimensions D_q, the ordering parameter Δ, the heterogeneity parameter *h*, and the entropy of the system*S*. The heteroannihilation process was modeled at different interaction probabilities (from 20% to 100%). An interaction probability equal to 100% corresponds to the instantaneous annicc yjb6hilation of a pair of particles of different species located at a distance of the interaction radius, while a decrease in the interaction probability allows the modeling of longer-lived pairs. The interaction probability between particles at a distance greater than the interaction radius was assumed to be 0%. All modeling results presented in this work included 3000 iterations on a 500x500 knot lattice. The degree of surface coverage by particles of the two varieties was 40%. The ratio of particles of different types was varied in the ratios 1:1, 1:2, and 1:5. No additional kinetic modes were observed at iterations greater than 3000 for the selected lattice size and degree of surface coverage by the particles under consideration. The program used for simulation was written in C++.

3. Results and discussion

A system representing inhomogeneously distributed particles on a structurally inhomogeneous surface can be considered as a multifractal set consisting of subsets with different fractal dimensionality characterizing the degree of spatial filling of the multifractal set. A change in the filling probability of fractal subsets leads to a change in the kinetic dependences and characteristics of the processes occurring in such systems. Taking this into account, when considering the kinetics of heteroannihilation on a structurally inhomogeneous surface, several fractal subsets with different distribution patterns can be distinguished.The total number of such subsets will be considered equal to*K*, and the fraction of particles of sort *A*, distributed over such subsets will be considered equal toA_1, A_2, A_3,..,A_K. For different fractal subsets the following distributions of particles *A* and B relative to each other are possible: 1) particles of kind *A* have no particles of kind *B* in the nearest coordination spheres.This case will correspond to the longest decay time (τ_1), 2) the number of particles of kind *A* $\leq$ the number of particles of kind *B* that are at a distance of the interaction radius (the first coordination sphere). This case corresponds to the shortest decay time (τ_K). All other types of distributions in which the interaction zone of particle *A* contains several particles of kind *B* will be intermediate, the decay time for which (τ_i) corresponds to the condition$\tau_1 < \tau_i < \tau_K$.This approach allows us to approximate the kinetic dependence by the sum of exponents in the form:

$$I(t) = \sum_{i=1}^{K} A_i \, e^{-t/\tau_i}. \quad (3)$$

In this case, if the distance between *A* and *B* is greater than the interaction radius, the exponent in formula (3) must contain a value that depends on the medium dimensionality, the concentration of the interacting molecules, and the interaction radius. This approach can also be used to study the processes of remote radiation-free energy transfer, contact quenching of luminescence, reversible capture of charge carriers by traps, and others [2].

Taking into account the presence of different kinetic modes in the fractal subsets of the system being modeled, the fractal, statistical and kinetic parameters at different iterations that characterize the change in the distribution of interacting particles during heteroannihilation were calculated. The fractal dimension d_f, was chosen as a fractal parameter, asymmetry and excess were used as statistical parameters, and the velocity coefficient *k*was used as a kinetic parameter. Fractal dimension, or Hausdorff dimension, is a

quantitative characteristic of a set of points in n-dimensional space, showing how densely points fill a subspace when their number becomes very large. Excess and asymmetry have been used to describe the shape and degree of symmetry of the distribution of interacting particles. Calculations of fractal dimensionality, excess and asymmetry were performed using the Gwyddion software [19].

In determining the fractal dimensionality we considered the set of points *F*embedded in the Euclidean space $E_n$of dimension $n \geq 1$. $n=1,2,3,...$,an arbitrary arbitrarily small number $\varepsilon > 0$, defining an n-dimensionalε-cube in the space E_n. The minimum number ofn-dimensional ε-cubes covering the set of points *F* with the accuracy ε denote $N_n(\varepsilon)$.Then, the expression for the fractal dimension of the set *F* will be [18]:

$$d_f = d_f[F] = -\lim_{\varepsilon \to 0} \frac{\ln (N_n(\varepsilon))}{\ln (\varepsilon)}. \quad (4)$$

From formula (4) we see that for Euclidean space E_n the fractal dimension $d_f = n$. In the general case $d_f \neq n$. Negative values ofd_f characterize the degree of emptiness of the set. The limit in formula (4) exists if the set *F* has the property of self-similarity or scale invariance.If the number of points in an n-dimensional ε-cube with number *i*is denoted by $n_i(\varepsilon)$, then we can determine the probability that a randomly taken point from the set is in an n-dimensional ε-cube with number*i* by the formula:

$$p_i(\varepsilon) = \lim_{N_n(\varepsilon) \to \infty} \frac{n_i(\varepsilon)}{N_n(\varepsilon)} \quad (5)$$

Accordingly, $p_i(\varepsilon)$in formula (5) characterizes the relative population of n-dimensional ε-cubes in the spaceE_n. If the distribution of points in the cells is unequal, then the fractal is inhomogeneous, i.e. it is a multifractal. In general case, multifractal is characterized by some nonlinear function [20]:

$$\tau(q) = \lim_{\varepsilon \to 0} \frac{\ln Z(q,\varepsilon)}{\ln \varepsilon}, \text{where } -\infty < q < +\infty, \quad (6)$$

determining the behavior of the statistical sum $Z(q, \varepsilon)$for $\varepsilon \to 0$:

$$Z(q,\varepsilon) = \sum_{i=1}^{N(z)} p_i^q(\varepsilon) \approx \varepsilon^{\tau(q)} \quad (7)$$

Taking this into account, surfaces with multifractal and chaotic initial distributions of interacting particles were modeled and the process of heteroannihilation was simulated using the probabilistic cellular automaton of class IV. When modeling a surface with an initial chaotic distribution of interacting particles, the Randomize random number generator was used to select the coordinates of particles on a planar lattice. The change in the entropy of the system was chosen as a criterion for multifractal formation, the decrease of which indicated the formation of surface structures differing from each other by statistical parameters such as homogeneity and ordering. The change in the statistical characteristics of the particle distribution over the modeled surface as a result of heteroannihilation can be estimated using the function $f(\alpha)$, which describes the Hausdorff dimension spectrum of homogeneous subsets of the original set, which is a multifractal: $f(\alpha) = q\alpha - \tau(q)$, where $\alpha = \frac{d\tau(q)}{dq}$. The homogeneous subsets that give the largest contribution to the statistical sum (7) for a given q are taken into account. The spectrum of generalized fractal dimensions of Renyi D_q, $-\infty < q < +\infty$, whose calculation methodology is described in detail in [5, 21, 22, 23], can be used to analyze changes in the fractal parameters of the particle distribution during heteroannihilation of particles on the modeled structurally inhomogeneous surface. The values of the parameter q determine the contribution to the statistical sum (7) of cells with different particle densities: from cells with the lowest particle density and low probability of their filling ($q \to -\infty$) to cells with the highest particle density and high probability of detection of such cells ($q \to \infty$). The function $D_q(q)$ is monotonically increasing with increasing q. Thus, for a homogeneous fractal all generalized fractal Renyi dimensions will coincide. The parameters D_0, D_1 were the most informative for the purposes of this paper. D_0 is calculated at q=0 and represents a constant value, which can be considered as a rough parameter for a multifractal. The calculated value of the fractal dimension D_1 at q=1 characterizes the rate of increase in the amount of information with

.

decreasing scale of the investigated structure. The numerical values of the parameters D_0, D_1 did not exceed 2.36.

The examples of simulated surfaces with initial chaotic and multifractal distributions of interacting particles at temperature T=273K and interaction probabilities of 100% and 20% in different iterations (N=100 and N=2000) are presented in figure 1.

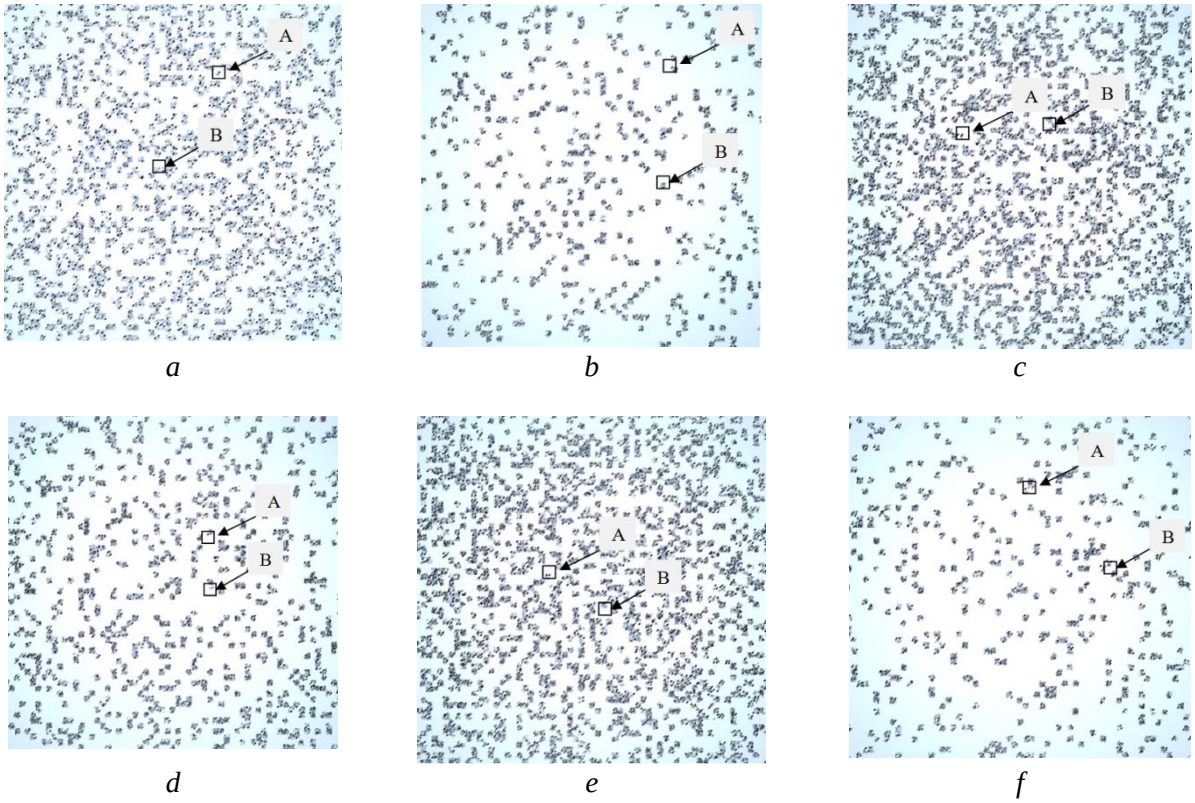

Fig.1. Changes in the distribution of interacting particles on the modeled surface at the temperature T=273K and interaction probabilities of 100% (a, b, e, f) and 20% (c, d): a), c), e) - number of iterations N=100, b), d), f) - number of iterations N=2000. Initial distribution of interacting particles is chaotic (a, b, c, d) and multifractal (e, f)

The normalized kinetic curves for the simulated heteroannihilation process at temperatures T=193K, 237K and 273K and interaction probabilities equal to 20% and 100% are shown in Figure 2 for the cases with initial chaotic and initial multifractal distributions of interacting particles.

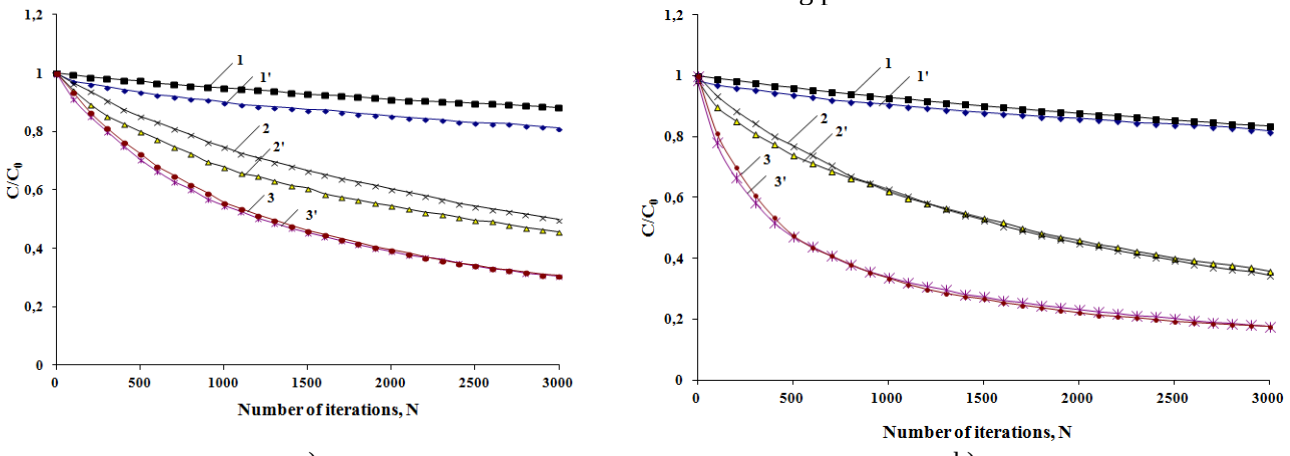

Fig.2. Normalized kinetic curves for the simulated heteroannihilation process with initial chaotic (curves 1',2',3') and initial multifractal (curves 1,2,3) distributions of interacting particles at temperatures 193K (curves 1 and 1'), 237K (curves 2 and 2'), 273K (curves 3 and 3') and interaction probabilities 20% (a) and 100% (b)

In Figure 2 the initial number of particles of kind A on the modeled surface is C_0, C=C(N) s the number of particles of kind *A* for each *N*-th iteration of the simulated heteroannihilation process As can be seen from Figures 1 and 2, the interaction probability, the initial distribution of interacting particles, and the temperature-dependent mobility of interacting particles affect the formation of kinetic modes at different iterations of the heteroannihilation process.

Figure 2 shows that the influence of the initial distribution of interacting particles is most pronounced at lower temperatures (193K and 237K) and lower values of interaction probability (20%). This may be due to the anomalous nature of diffusion of interacting particles over the simulated surface and dependence of the "diffusion coefficient" *K(r)* of a particle on the distance r between its current and starting positions: $K(r) \approx r^{-\theta}$, where θ is the index of anomalous straying on the modeled surface [24].This is confirmed by the observed dependence of fractal dimensions on the number of iterations (Figure 3). The decrease in d_f in Figure 3 is associated with an effective decrease in the number of space points available to the diffunding particle.

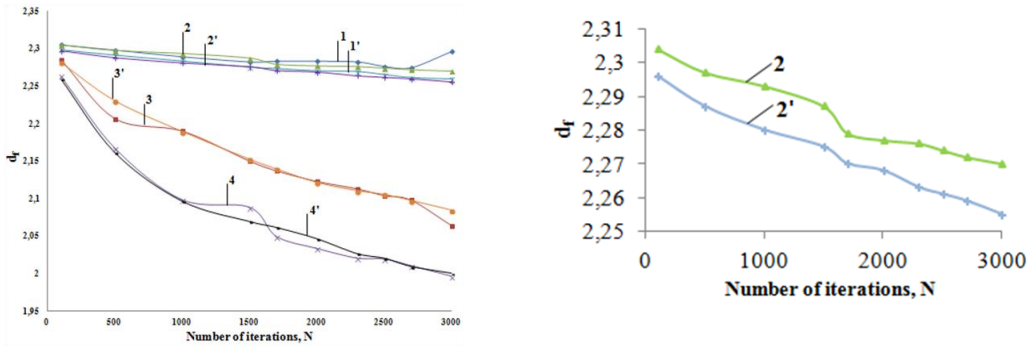

Fig.3. Changes in fractal dimension of the simulated system during heteroannihilation for the initial chaotic (curves 1',2',3,4') and multifractal (curves 1,2,3,4') distributions at 20% (curves 1,1',3,3') and 100% (curves 2,2',4,4') interaction probabilities and 193K (curves 1,1',2,2') and 273K (curves 3,3',4,4') temperatures. Inset: change in fractal dimensionality during heteroannihilation for the initial chaotic (curve 2') and multifractal (curve 2) distributions at 100% interaction probability and 193K temperature

The values of fractal dimensions at 193K remain higher at 20% and 100% probabilities compared with the same data for 273K. This indicates that in the distribution of interacting particles at low temperatures the spatial heterogeneity persists longer. At the same time, as seen in the inset to Figure 3, the values of fractal dimensions at low temperatures for the initial chaotic distribution remain lower than for the initial multifractal distribution over the whole considered time interval. Thus, an increase in the mobility of interacting particles, interaction probability, and changes in the free volume available to interacting particles leads to a sharper change in the fractal dimensionality, and, consequently, to a change in the fractality of heteroannihilation kinetics. This conclusion is consistent with the results of other works, e.g. [9, 25].

Similar trends are observed in the changes in asymmetry and excess during heteroannihilation (Figure 4). Large values of asymmetry and excess indicate a significant deviation from the normal distribution of interacting particles over the surface. A positive excess means that the outliers in the data are more intense than for the normal distribution. A distribution with significant negative asymmetry has a long tail to the left of the mathematical expectation. At the same time, comparison of the dependencies presented in Figures 3 and 4 shows that decrease of fractal dimension as a result of heteroannihilation leads to decrease of asymmetry and increase of excess. Analysis of the kinetic dependences of the modeled heteroannihilation process showed the existence of two different velocity regimes at different time intervals: the short-term interval ($N \leq 1500$) and the long-term interval ($N \geq 1500$). The calculations showed that the values of the velocity coefficients at both the short- and long-time intervals depend on the initial distribution of interacting particles, their mobility, and the interaction probability.As the mobility of particles increases, the velocity coefficient for the short-range interval increases for both multifractal and chaotic initial distributions. The only exception is the case with the multifractal initial distribution at the interaction probability of 20%, for which the decrease of the rate coefficient with the increase of mobility of interacting particles was observed. This can be due to anomalous diffusion of interacting particles, caused by formation of local stable structures on the surface, limiting rapprochement of particles.

.

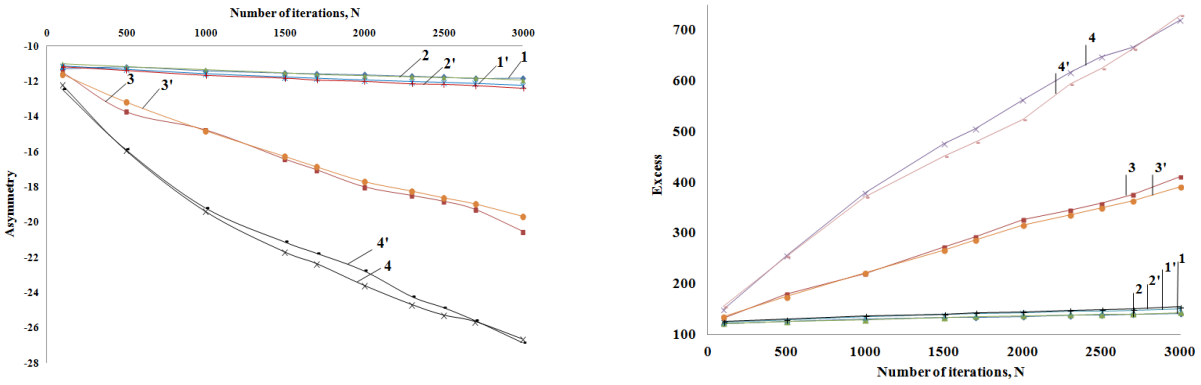

a) b)

Fig.4. Changes in asymmetry (a) and excess (b) of the simulated system during heteroannihilation for the initial chaotic (curves1',2',3',4') and multifractal (curves 1, 2,3,4') distributions at interaction probabilities of 20% (curves 1,1',3,3') and 100% (curves 2,2',4,4') and temperatures of 193K (curves 1,1',2,2') and 273K (curves 3,3',4,4')

For the long-time interval for both the chaotic and multifractal distributions, regardless of the interaction probability, the velocity coefficient decreased as the particle mobility increased. The ratio of velocity coefficients for the short- and long-time intervals increased as the mobility of particles increased, irrespective of the interaction probability. The observed trends in simulations of interaction processes of particles on a structurally heterogeneous surface indicate the fractal nature of the kinetics with different degrees of fractality depending on the particle mobility, interaction probability and initial distribution of interacting molecules, which is in agreement with the results of other works [9, 26, 27].

4. Conclusion

In this paper the process of heteroannihilation in a system representing a structurally inhomogeneous surface with chaotically and multifractally distributed on it particles of two kinds at the initial moment of time is modeled by the method of probabilistic cellular automata of class IV. Comparison of kinetic, statistical and fractal parameters calculated for the considered system has shown their dependence on interaction probability, mobility of interacting particles and character of initial distribution of interacting particles throughout the considered iteration interval. The analysis of fractal dimensions at different iterations of the heteroannihilation process allowed to establish that the distribution of interacting particles at low temperatures retains spatial inhomogeneity longer, which is associated with a change in the fractality of the kinetics of this process.

The effect of the initial distribution of interacting particles is most pronounced at lower temperatures (193K and 237K) and lower values of the interaction probability (20%). This may be due to the anomalous diffusion character of the interacting particles, caused by the formation of local stable structures on the surface, limiting the convergence of the particles. In this case, the values of fractal dimensions at low temperatures for the initial chaotic distribution remain lower than for the initial multifractal distribution throughout the considered iteration interval. An increase in the mobility of interacting particles, interaction probability, and changes in the free volume available for interacting particles leads to a sharper change in the fractal dimensionality and, consequently, to a change in the fractality of the heteroannihilation kinetics. Analysis of the kinetics of heteroannihilation showed the existence of two different rate regimes at different iteration intervals. Thus, the method used in this work allows us to standardize the description of the loss kinetics of interacting particles on surfaces of different structure and morphology.

Acknowledgments

Moldanazarova Ulserik was supported by the grant AP14972893 from the Committee of Science of the Ministry of Science and Higher Education of the Republic of Kazakhstan.

REFERENCES

1 Vertyagina Y., Marrow T.J. Multifractal-based assessment of Gilsocarbon graphite microstructures. *Carbon*, 2016, Vol. 109, pp. 711 – 718. doi:10.1016/j.carbon.2016.08.049.

2 BodunovE.N. Kinetics of luminescence attenuation of nanocrystals: physical models and approximation by the sum of three exponents. *Optics and spectrosc.*, 2023, Vol.131, pp.100-103. doi.10.21883/OS.2023.01.54545.91-22.

3 MwemaF., Tien-Chien J. Statistical and Fractal Description of Defects on Topography Surfaces. *MATEC Web of Conferences*, 374, 01001 (2023) ICARAE2022. doi. 10.1051/MATECCONF.2023.37401001.

4 Bryukhanov V.V., et al. Effect of Temperature on the Rate of Triplet–Triplet Annihilation of 1,2-Benzanthracene in a Polymer Matrix. *Journal of Applied Spectroscopy*, 2004, Vol. 71, pp. 54– 59. doi:10.1023/B:JAPS.0000025348

5 BaktybekovK., KarstinaS., Vertyagina E., Myrzakhmet M., Akimbekov E. Dependence of accumulated luminosity of thermostimulated luminescence on type of the electron–hole center distribution in a crystal. *Journal of Luminescence*, Vol. 122-123, 2007, pp. 374 – 376. doi:10.1016/j.jlumin.2006.01.194.

6 Karstina S.G., Markova M.P., Bryukhanov V.V. Homo- and Heteroannihilation of Triplet-Excited Bengali Rose and Anthracene Molecules on Silica in a Wide Temperature Range. *Journal of Applied Spectroscopy*, 2003, Vol. 70, pp. 733–739, doi: 10.1023/B:JAPS.0000008871.70120.d4.

7 BagnichS.A.. Migration of triplet excitations of complex molecules in disordered media and in systems with limited geometry. *Solid State Physics*, 2000, Vol. 42, pp. 1775-1801. https://doi.org/10.1134/1.1318866.

8 PituliceaL., Vilasecad E., IsvoranaA., et al. Aspects Of Fractal Kinetics Of Enzymatic Reactions By Monte Carlo Simulations. *Annals of West University of Timisoara Series Chemistry*, 2011, Vol. 20(2), pp. 95 –104.

9 Grima R., Schnell S. A systematic investigation of the rate laws valid in intracellular environments. *Biophys. Chem.*, 2006, Vol. 24, pp. 1 – 10, doi: 10.1016/j.bpc.2006.04.019.

10 Grima R. Schnell S. How reaction kinetics with time-dependent rate coefficients differs from generalized mass action. *Chem.phys.chem*., 2006,Vol. 7, pp. 1422 – 1424. https://doi.org/10.1002/cphc.200600081.

11 Turner T.E., Schnell S., Burrage K. Stochastic approaches for modeling in vivo reactions.*Comput. Biol. And Chem.*, 2004, Vol. 28, pp. 165 – 178. doi: 10.1016/j.compbiolchem.2004.05.001.

12 Kopelman R. Fractal reaction kinetics. *Science*, 1988, Vol. 241, pp. 1620 – 1626. doi:10.1126/science.241.4873.1620.

13 Schnell S., Turner T.E. Reaction kinetics in intracellular environments with macromolecular crowding: simulations and rate laws. *Progress in Biophysics and Molecular Biology*, 2004, Vol. 83, pp. 235-260, doi: 10.1016/j.pbiomolbio.2004.01.012.

14 Zhdanov V.P. Simulation of enzymatic cellular reactions complicated by phase separation. *Physical Review E*, 2000, Vol. 63, pp. 0119081 – 0119086. doi:10.1103/PhysRevE.63.011908.

15 Isvoran A., Vilaseca E., Ortega. F., et al. About implementing a Monte Carlo simulation algorithm for enzymatic reactions in crowded media. *JSCS*, 2006, Vol. 71, pp. 75 – 86. doi:10.2298/JSC0601075I.

16 Isvoran A., Unipan L. Fractal kinetics of enzymatic reactions in three dimensional crowded media. A computational study. *Annals of West University of Timişoara, Series of Chemistry*, 2007, Vol. 16, pp. 121 – 126.

17 Berry H. Monte Carlo simulations of enzyme reaction in two dimensions: Fractal kinetics and spatial segregation. *Biophysical J*, 2002, Vol. 83, pp. 1891 – 1902. doi: 10.1016/S0006-3495(02)73953-2.

18 Zelenyi L.M., Milovanov A.V. Fractal topology and strange kinetics: from percolation theory to problems in cosmic electrodynamics. *Successes of physical sciences*, 2004, Vol. 174, No. 8, pp. 809– 852, doi:10.1070/PU2004v047n08ABEH001705.

19 Nečas D., Klapetek P. Gwyddion: An open-source software for SPM data analysis, *Cent. Eur. J. Phys*, 2012, 10(1), pp. 181-188. https://doi.org/10.2478/s11534-011-0096-2.

20 BozhokinS.V., Parshin D.A.*Fractals and multifractals*. Moscow-Izhevsk, 2001, 128 p.[in Russian].

21 Karstina, S.G., et al. Analysis of the Luminescence Decay on the SiO_2 Surface at Different Temperatures within the Multifractal Formalism. *Russ Phys. 2005*, 48, pp. 553–558. doi:10.1007 /s11182-005-0169-z.

22 Karstina, S.G. Computer Modelling and Description of Stablemolecular Cluster Formation Dynamics in Dispersion Matrix Using Multifractal Analysis. *Eurasian phys. tech. j*., 2017, Vol. 14, No. 2(28), pp. 27-30.

23 Karstina S.G., Baktybekov K.S., Baratova A.A. Thermodynamical and Kinetical Formation's Conditions of Firm Fractal Structures on the Surface. *Nonlinear world, 2007*, No. 3 (5), pp. 133-138.

24 Kucherenko M.G., Ignatiev A.A. Kinetics of diffusion-dependent annihilation of quasiparticles on fractals under conditions of their correlated initial distribution. *Electr. scientific journal "Researched in Russia"*, 2006, 138p.

25 Fan J., Wang L., LiuF., LiuZ., LiuY., Zhang S. Model of Moisture Diffusion in Fractal Media. *Thermal science*, 2015, Vol. 19, No. 4, pp. 1161– 1166. doi:10.2298/TSCI1504161F.

26 Popov A.A., Lee S.C., Kuksa P.P., et al. Parallel Algorithm for Large Fractal Kinetic Models with Diffusion. *Biorxiv*, 275248. doi: 10. 1101/275248.

27 Ben-Avraham D., Havlin S. *Diffusion and reactions in fractals and disordered systems*. Cambridge University Press, London, 2000, 316 p. https://doi.org/10.1017/CBO9780511605826.

Article accepted for publication 15.05.2023

.

SUMMARIES	ТҮСІНІКТЕМЕЛЕР	АННОТАЦИИ

Кучеренко М.Г., Кручинин Н.Ю.

Айнымалы электр өрісінде өткізгіштігі төмен нанобөлшектегі адсорбцияланған полиэлектролиттің конформациялық құрылымы

Нанобөлшек материалының плазмалық жиілігінен едәуір төмен жиіліктегі сыртқы гармоникалық өзгеретін квазистатикалық электр өрісінде поляризацияланатын салыстырмалы түрде төмен электр өткізгіштікке ие (легирленбеген жартылай өткізгіш) наносфероидта адсорбцияланған полиэлектролиттің гаусс тізбегі түйіндерінің квази-тепе-теңдікті конформациялық құрылымы моделінің аналитикалық формасы ұсынылған. Квазистатикалық жуықтаудан тыс шығатын модель нұсқалары талқыланды, яғни жеткілікті созылыңқы наноқұрылымдар жағдайында байқалатын кешігу әсерлерін ескеріледі. Молекулалық динамика әдісімен статикалық немесе айнымалы сыртқы электр өрісінде орналасқан сфералық германий нанобөлшегінің бетіндегі жалпы бейтарап полиамфолитті полипептидтердің электрлік индукцияланған конформациялық өзгерістері зерттелді. Статикалық электр өрісінде полиамфолитте зарядталған байланыстар арасындағы қысқа қашықтық жағдайында нанобөлшектің поляризация осі бағытында созылған макротізбектің көптеген ілмектері пайда болды. Егер полипептидтің қарама-қарсы зарядталған аминқышқылдарының қалдықтары арасындағы ара-қашықтық нанобөлшектің диаметрінен артық болса, онда зарядталған түйіндер негізінен поляризацияланған германий нанобөлшегінің қарама-қарсы зарядталған полярлық аймақтарында локализацияланған. Айнымалы электр өрісінде нанобөлшектің экваторлық аймағында белдеулі полиамфолит жиегі пайда болды, оның макро тізбектерінің түйіндері поляризацияланатын айнымалы электр өрісінің амплитудасы артқан кезде беттен десорбцияланды.

***Кілт сөздері*:** Жартылай өткізгіш нанобөлшек, макромолекула, конъюгаттар, конформациялар, молекулалық динамика.

Кучеренко М.Г., Кручинин Н.Ю.

Конформационная структура адсорбированного полиэлектролита на наночастице с невысокой проводимостью в переменном электрическом поле

Предложена аналитическая форма модели квазиравновесной конформационной структуры звеньев гауссовой цепи полиэлектролита, адсорбированного на наносфероиде с относительно низкой электрической проводимостью (нелегированный полупроводник), поляризующемся во внешнем гармонически изменяющемся квазистатическом электрическом поле с частотой, существенно меньшей плазменной частоты материала наночастицы. Обсуждаются варианты модели, выходящие за рамки квазистатического приближения, то есть учитывающие эффекты запаздывания, проявление которых будет заметным в случае достаточно протяженных наноструктур. Методом молекулярной динамики исследованы электрически индуцированные конформационные изменения в целом нейтральных полиамфолитных полипептидов на поверхности сферической германиевой наночастицы, находящейся в статическом или в переменном внешнем электрическом поле. В статическом электрическом поле в случае небольшого расстояния между заряженными звеньями в полиамфолите образовывалось большое количество петель макроцепи, вытянутых в направлении оси поляризации наночастицы. В случае, если расстояние между противоположно заряженными аминокислотными остатками полипептида превышало диаметр наночастицы, заряженные звенья в основном были локализованы в противоположно заряженных приполярных областях поляризованной германиевой наночастицы. В переменном электрическом поле образовывалась опоясывающая полиамфолитная опушка в экваториальной области наночастицы, звенья макроцепи которой при увеличении амплитуды поляризующего переменного электрического поля десорбировались с поверхности.

Ключевые слова: полупроводниковая наночастица, макромолекула, конъюгаты, конформации, молекулярная динамика.

Бердібеков А.Т., Халенов О.С., Зиновьев Л.А, Лауринас В.Ч., Грузин В.В., Доля А.В.

Алюминий өнімдерінің теңіз суындағы коррозиясының себебі.

Ұсынылған жұмыста алюминий өнімдерінің теңіз суындағы коррозиясы өнімдердің бетіндегі алюминий ұяшықтарының толық тотықпауының салдарынан болады деп болжанады. Алюминий ұяшықтарының толық тотықпауы 450°С-қа дейінгі температурадаларда текше беттік орталықтандырылған алюминий ұяшығының ромбты ішкі жүйесінің алюминий атомдарымен химиялық әрекеттесу үшін оттегі молекулаларының энергиясының жеткіліксіздігінен болады. Йодтың 5% спирттік ерітіндісінің беті алдын ала 450°С дейін қыздырылған оттегімен байланыста болған және ультракүлгін сәулеленуге ұшыраған алюминий фольгамен 12 сағат әрекеттескенде химиялық реакция жылдамдығының айтарлықтай төмендейтіндігі көрсетілген. Оттегінің химиялық жоғары белсенді түрлерімен 12 сағаттық жанасу нәтижесінде фольга үлгілерінің бетіндегі алюминий ұяшықтарының көпшілігі толығымен тотығады және шын мәнінде галогендермен химиялық

әрекеттесуге түспейтін корундқа айналады деп болжанады.
Кілтті сөздер: кванттық-химиялық есептеулер, алюминий, алюминий оксиді, кубтық кіші жүйе, тотығу, галогендер.

Бердибеков А.Т., Халенов О.С., Зиновьев Л.А, Лауринас В.Ч., Грузин В.В., Доля А.В.
Причина коррозии изделий из алюминия в морской воде.
В представленной работе сделано предположение, что коррозия алюминиевых изделий в морской воде возникает из-за неполного окисления ячеек алюминия на поверхности изделий. Неполное окисление ячеек алюминия происходит по причине того, что у молекул кислорода при температурах до 450 °С не хватает энергии для химического взаимодействия с атомами алюминия ромбической подсистемы кубической гранецентрированной ячейки алюминия. Показано, что происходит значительное уменьшение скорости химической реакции при взаимодействии 5% спиртового раствора йода с алюминиевой фольгой поверхность которой предварительно в течении 12 часов контактировала с кислородом, нагретым до 450 °С и подвергнутым ультрафиолетовому облучению. Предполагается, что в результате 12 часового контакта с химически высокоактивными формами кислорода большая часть ячеек алюминия на поверхности образцов фольги была полностью окислена, фактически превратившись в корунд, который не вступает в химическое взаимодействие с галогенами.
Ключевые слова: квантово-химические расчеты, алюминий, оксид алюминия, кубическая подсистема, окисление, галогены

Сатаева Г.Е., Баратова А.А., Сакипов К.Е., Әбдіғапар А.А., Шарифов Д.М.
C_{60} полистирол-фуллерен жүйесі негізіндегі көміртегі бар нанокомпозиттік қабықшалардың оптикалық қасиеттері
Көміртек негізіндегі нанокомпозиттер өзінің бірегей қасиеттеріне және әртүрлі технологиялық қолданбаларда пайдалану мүмкіндігіне байланысты үлкен назар аударды. Берілген жұмыста C_{60} фуллерен наноқоспаларға ие полистирол негізіндегі көміртегі бар нанокомпозиттік полимерлі қабықшалардың спектрлік қасиеттерін анықтау үшін эксперименттік зерттеулер жүргізілді. Нәтижелер плистирол матрицасына фуллерен нанобөлшектерін қосу материалдың оптикалық қасиеттерін жақсартатынын көрсетті. Атап айтқанда, көміртегі қоспасының концентрациясының жоғарылауымен үлгілердің оптикалық тығыздығы артады, жұтылу коэффициенті артып, ал тыйым салынған аймақ ені азаяды. Берілген нәтижелер фуллерен негізіндегі нанокомпозиттер оптоэлектронды және нанотехнологиялық қолданбалар үшін перспективті материалдар болып табылатынын көрсетеді. Бұл жұмыстың нәтижелері көміртегі негізіндегі нанокомпозиттер және олардың электроника, энергияны сақтау және сенсорлық қосымшаларды қоса алғанда бірқатар салаларда пайдалану әлеуеті бойынша зерттеулер санының артуына ықпал етеді. Фуллерен негізіндегі нанокомпозиттердің жақсартылған оптикалық қасиеттері олардың жаңа оптоэлектронды құрылғылар мен сенсорларды жасау үшін әсіресе пайдалы болуы мүмкін екенін көрсетеді. Алынған нәтижелер фуллерен негізіндегі нанокомпозиттерді әртүрлі технологиялық қолдану үшін жан-жақты және маңызды материал ретінде пайдаланудың кең мүмкіндіктерін көрсетеді.
Кілт сөздері: нанокомпозиттік полимерлі қабықшалар, көміртегі нанобөлшектері, фуллерен, полистирол.

Сатаева Г.Е., Баратова А.А., Сакипов К.Е., Абдигапар А.А., Шарифов Д.М.
Оптические свойства углеродсодержащих нанокомпозитных пленок на основе системы полистирол-фуллерен C_{60}.
Нанокомпозиты на основе углерода привлекают значительное внимание благодаря своим уникальным свойствам и возможностям их использования в различных технологических приложениях. В данной работе проведены экспериментальные исследования по определению спектральных свойств углеродсодержащих нанокомпозитных полимерных пленок на основе полистирола с нанодобавками фуллерена C_{60}. Результаты показывают, что включение наночастиц фуллерена в матрицу плистирола улучшают оптические свойства материала. В частности, с увеличением концентрации углеродной добавки увеличивается оптическая плотность образцов, увеличивается коэффициент поглощения и уменьшается ширина запрещенной зоны. Эти результаты позволяют предположить, что нанокомпозиты на основе фуллеренов являются перспективными материалами для оптоэлектронных и нанотехнологических приложений. Результаты этой работы способствуют растущему объему исследований нанокомпозитов на основе углерода и их возможностей для использования в ряде областей, включая электронику, хранение энергии и сенсорные приложения. Улучшенные оптические свойства нанокомпозитов на основе фуллеренов позволяют предположить, что они могут быть особенно полезны для разработки новых оптоэлектронных устройств и датчиков. Полученные результаты показывают широкие перспективы использования нанокомпозитов на основе фуллерена как универсальной и многообещающий материал для различных технологических применений.
Ключевые слова: нанокомпозитные полимерные пленки, углеродные наночастицы, фуллерен, полистирол.

Утамурадова Ш.Б., Далиев Ш.Х., Рахманов Д.А., Дорошкевич А.С., Генов И.Г., Туан П.Л., Кириллов А.К.
Платинамен диффузиялық-легирленген және протондармен сәулеленген кремнийдегі ақау түзілу процестері.
Берілген жұмыста импеданс спектроскопиясы әдісін қолдана отырып, платинамен легирленген *n*-типа (*n*-Si) монокристалды кремнийдегі ақаудың пайда болу процестеріне технологиялық режимдердің және протондарды имплантациялаудың (дозаыс 5×10^{14} бөлшек / $см^{-2}$) әсері зерттелді. Кремнийдің электр өткізгіштігінің радиациялық индукцияланған өзгерістері кремнийдегі қоспалармен легирлеудің технологиялық режимдеріне айтарлықтай тәуелді екендігі анықталған. Годографтар платинамен легирлеу кремний үлгілерінің электр кедергісінің төмендеуіне әкелетінін көрсетті. $5{,}1\cdot10^{14}$ бөлшектер / $см^2$ дозада 2 МэВ энергиялы протондармен сәулелену зерттелетін кремний үлгілерінің электр кедергісінің айтарлықтай (2-3 есе) артуына әкеледі. 1200°С температурада легирленген үлгілердің радиациялық әсерге салыстырмалы түрде жоғары төзімділігі (кедергінің өзгеруі 16% - дан аспайды: иондық имплантация нәтижесінде 55 кОм-дан 65 кОм-ға дейін) 1100°С-пен салыстырғанда көлемде ион (платина) қоспаларының жоғары концентрациясына шартталған деген қорытындыға келді.
Кілт сөздері: кремний, платина, легирлеу, жоғары температуралы диффузия, протондық сәулелену.

Утамурадова Ш.Б., Далиев Ш.Х., Рахманов Д.А., Дорошкевич А.С., Генов И.Г., Туан П.Л., Кириллов А.К.
Процессы дефектообразования в кремнии, диффузионно-легированном платиной и облученном протонами
В настоящей работе изучено влияние технологических режимов и имплантации протонов (доза 5×10^{14} частиц / $см^{-2}$) на процессы дефектообразования в монокристаллическом кремнии *n*-типа (*n*-Si), легированном платиной с использованием метода импедансной спектроскопии. Установлено, что радиационно-индуцированные изменения электропроводности кремния существенно зависят от технологических режимов легирования примесями в кремнии. Годографы показывают, что легирование платиной приводит к снижению электросопротивления образцов кремния. Облучение протонами с энергией 2 МэВ в дозе $5{,}1\cdot10^{14}$ частиц/$см^2$ приводит к значительному (в 2-3 раза) увеличению электрического сопротивления исследуемых образцов кремния. Сделан вывод, что относительно высокая стойкость к радиационному воздействию (изменение сопротивления не более 16 %: от 55 кОм до 65 кОм в результате ионной имплантации) образцов, легированных при 1200°С, предположительно обусловлена более высокой концентрацией примесей ионов (платины) в объеме по сравнению с 1100°С. образцы кремния.
Ключевые слова: кремний, платина, легирование, высокотемпературная диффузия, протонное облучение.

Березовская И.Э., Тасмұханова А.Ә., Рыспаева М.Ж., Оспанова Ш.С.
Сұйық отынның бүрку жылдамдығының жану процесіне әсерін сандық әдіспен зерттеу.
Бұл жұмыста сұйық отынның жану камерасына отын айдаудың әртүрлі жылдамдығында жануы зерттелді. Зерттелетін процестер келесі теңдеулер арқылы сипатталады: үздіксіздік, импульс, энергия, *k-ε* турбуленттілік моделі және т.б. Есептеу эксперименті KIVA-II бағдарламалық құралын қолдану арқылы жүргізілді. Сандық әдіс тиімді және әртүрлі факторларды ескереді, мысалы, көп сатылы химиялық тізбекті реакциялар, жылу мен массаның конвекция, сәулелену, турбуленттілік арқылы берілуі және т.б. Инъекция жылдамдығының оңтайлы параметрлерін анықтау үшін гептанды жану камерасына айдау жылдамдығының гептанның жану және өздігінен тұтану процесіне әсері зерттелді. Гептанды енгізу жылдамдығы 30 м/с аралықпен 160-тан м/с 400-ге м/с дейін өзгерді. Гептан бөлшектерінің булану алдындағы өлшемдері мен температуралық таралулары, реагенттер мен жану өнімдерінің концентрация өрістері, сонымен қатар жану камерасындағы температуралық өрістер жанармайдың саптама арқылы жану камерасына айдалу жылдамдығына байланысты алынды. Жану камерасының тиімділігін арттыру және қоршаған ортаға кері әсерін азайту мақсатында гептанды айдау жылдамдығының оңтайлы диапазоны 250 м/с – 280 м/с болып анықталды.
Кілттік сөздер: сандық әдістер, компьютерлік модельдеу, химиялық кинетика, сұйық отынның жануы, гептан, турбулентті жылу және масса алмасу, айдау, жану камерасы.

Березовская И.Э., Тасмуханова А.А., Рыспаева М.Ж., Оспанова Ш.С.
Исследование влияния скорости впрыска жидкого топлива на процесс сгорания численным методом.
В данной работе исследовалось воспламенение жидкого топлива при различных скоростях впрыска топлива в камеру сгорания. Исследуемые процессы описываются следующими уравнениями: неразрывности, импульса, энергии, k-ε модели турбулентности и другими. Вычислительный эксперимент проводился с использованием программного обеспечения KIVA-II. Численный метод эффективен и учитывает различные факторы, такие как многоступенчатые химические цепные реакции, перенос количества тепла и массы конвекцией, излучением, турбулентностью и т. д. Изучено влияние скорости впрыска гептана в камеру сгорания на процесс горения и самовоспламенения гептана для определения оптимальных параметров скорости впрыска. Скорость вспрыска гептана варьировалась от 160 м/с до 400 м/с с интервалом в 30 м/с. Получены распределения по размерам и температуре частиц гептана перед испарением, поля концентрации реагентов и продуктов сгорания, а также

температурные поля в камере сгорания в зависимости от скорости впрыска топлива через форсунку в камеру сгорания. Определен оптимальный диапазон скорости впрыска гептана, составляющий 250 м/с – 280 м/с, с целью повышения эффективности работы камеры сгорания и снижения негативного воздействия на окружающую среду.

Ключевые слова: численные методы, компьютерное моделирование, химическая кинетика, горение жидкого топлива, гептан, турбулентный тепломассоперенос, впрыск, камера сгорания.

Abouellail A.A., Chang J., Солдатов А.И., Солдатов А.А., Костина М.А., Васильев И.М.

Корпус-термоинтерфейс-радиатор жүйесінің жылу кедергісін термоэлектрлік бақылау.

Мақалада термоинтерфейсінің жылуфизикалық параметрлерін анықтау үшін термоэлектрлік бақылау әдісін қолдану ұсынылады. Термоинтерфейс металл беттердің арасында орналасқан, құрылғы жұмысының кез келген кезеңінде қыздыру кезінде олардың арасында термоЭҚК пайда болады. Жылуэлектрлік әдістің дұрыстығын растайтын терможұптармен өлшенген және термоЭҚҚ көмегімен өлшенген температура айырмашылығының қыздыру уақытынан графиктері келтірілген. Графиктер жылу кедергісін, температураның флуктуациясын және нәтижесінде пайда болған термоЭҚҚ енгізу кезінде жылу беру процесін көрнекі түрде көруге мүмкіндік береді. Ұсынылған әдіс термиялық кедергіні 8% - дан аз қателікпен басқаруға мүмкіндік береді.

Кілт сөздері: термоинтерфейс, жылу кедергісі, термоЭҚК, Зеебек эффектісі, термоэлектрлік бақылау.

Abouellail A.A., Chang J., Солдатов А.И., Солдатов А.А., Костина М.А., Васильев И.М.

Термоэлектричекий контроль теплового сопротивления системы корпус-термоинтерфейс-радиатор

В статье предложено применять способ термоэлектрического контроля для определения теплофизических параметров термоинтерфейса. Термоинтерфейс расположен между металлическими поверхностями, между которыми при нагреве возникает термоЭДС, на любом этапе эксплуатации прибора. Приведены графики разницы температур от времени нагрева, измеренного термопарами, и измеренные с помощью термоЭДС, подтверждающие правильность термоэлектрического метода. Графики позволяют наглядно увидеть процесс теплопередачи при введении теплового сопротивления, флуктуации температуры и результирующей термоЭДС. Предлагаемый метод позволяет контролировать термическое сопротивление с погрешностью менее 8 %.

Ключевые слова: термоинтерфейс, тепловое сопротивление, термоЭДС, эффект Зеебека, термоэлектрический контроль.

Байсериков Б.М, Ермаханова А.М., Исмаилов М.Б., Кенжегулов А.К., Кенжалиев Б.К.

Ароматты амин қатайтқышы бар эпоксидті шайыр негізіндегі препрегтердің өміршеңдігін зерттеу.

Қазіргі уақытта авиациялық-ғарыштық және қорғаныс өнеркәсібінде көміртекті пластиктерді пайдаланудың тұрақты үрдісі байқалады, ол негізінен алдын ала сіңдірілген жартылай фабрикаттар - препрегтерді пайдалануға негізделген. Препрегтік көміртекті пластикалық бөлшектерді өндіру көбінесе ұзақ өндірістік уақытты қажет етеді, оның барысында алдын-ала пайдалану қасиеттерін сақтау керек. Сондықтан препрегтің негізгі сипаттамаларының бірі – оның өміршеңдігі. Бұл жұмыста оңтайландырылған қасиеттері бар шайырдың қолайлы құрамы және сақтау уақытына байланысты препрегтің жабысқақтығы мен қатаю дәрежесін анықтауға негізделген препрег үлгілерінің өміршеңдігін зерттеу әдісі жасалды. Алдын-ала сақтау уақытының өңделген ламинаттардың беріктік сипаттамаларына әсері зерттелді. 60 күнге дейін ұзақ өміршеңдігі бар препрег үлгілері алынды. Алынған эксперименттік мәліметтер көміртекті пластиктен жасалған бұйымдарды өнеркәсіптік өндіруде практикалық маңызға ие, себебі олар алдын-ала дайындаудың пайдалану қасиеттері мен сақтау мерзімдері арасында байланыс орнатады.

Түйінді сөздер: полимерлі композициялық материал, препрегтер, шайыр, қатайтқыш, полимерлі байланыстырғыш, көміртекті талшық, өміршеңдік.

Байсериков Б.М, Ермаханова А.М., Исмаилов М.Б., Кенжегулов А.К., Кенжалиев Б.К.

Исследование жизнеспособности препрегов на основе эпоксидной смолы с ароматическим аминным отвердителем

Настоящее время наблюдается устойчивая тенденция использования углепластиков в авиационно-космической и оборонной промышленности, основанная преимущественно на использовании предварительно пропитанных полуфабрикатов - препрегов. Производство углепластиковых деталей из препрегов часто требует длительного производственного времени, в течение которого препрег должен сохранять свои эксплуатационные свойства. Поэтому одной из основных характеристик препрега является его жизнеспособность. В данной работе разработана подходящая композиция смолы с оптимизированными свойствами и методика исследования жизнеспособности образцов препрега, основанная на определении липкости и степени отверждения препрега в зависимости от времени хранения. Изучено влияние времени

хранения препрега на прочностные характеристики отвержденных ламинатов. Были получены образцы препрега с длительной жизнеспособностью до 60 дней. Полученные экспериментальные данные имеют практическое значение при промышленном производстве изделий из углепластиков, так как устанавливают связь между эксплуатационными свойствами препрега и сроками хранения.
Ключевые слова: полимерный композиционный материал, препреги, смола, отвердитель, полимерное связующее, углеродное волокно, жизнеспособность.

Тусупбекова А.К., Афанасьев Д.А., Сельдюгаев О.Б., Карабасов В.А., Алпысова Г.К., Абыкенов А.Т., Шейнмаиер Э.В.

Дыбыстық ақпаратты орындаудың микроконтроллерлік құрылғысын әзірлеу.

Жұмыста адамның қатысуымен дыбыстық ақпаратты ойнатып орындаудың микроконтроллерлік құрылғысын жобалау, әзірлеу және дайындау нәтижелері келтірілген. Микроконтроллер құрылғысының тұжырымдамасының сипаттамасы, жүйенің архитектурасы берілген. Құрылғы мен оның бағдарламалық жасақтамасын жасауға техникалық тапсырма жасалды. Arduino-UNO негізінде дыбыстық ақпаратты орындау құрылғысының прототипі жасалды. Бір өнімнің құнын төмендету мақсатында құрылғыны жаңарту жүргізілді және Attiny13A-SU микроконтроллері басқару микроконтроллері ретінде таңдалды. Электр сұлбасы, құрылғының баспа платасы және оған бағдарламалық қамтамасыз ету әзірленді. Дыбыстық ақпаратты ойнатудың 17 қолданыстағы құрылғысы жасалды. Микроконтроллер құрылғысын одан әрі жетілдірудің техникалық шешімі ұсынылды.
Түйінді сөздер: музыкалық орындық, микроконтроллерлік құрылғы, баспа платасы, Arduino-UNO, Attiny13A-SU, дыбыстық ақпарат.

Тусупбекова А.К., Афанасьев Д.А., Сельдюгаев О.Б., Карабасов В.А., Алпысова Г.К., Абыкенов А.Т., Шейнмаиер Э.В.

Разработка микроконтроллерного устройства воспроизведения звуковой информации

В работе приведены результаты проектирования, разработки и изготовления микроконтроллерного устройства воспроизведения звуковой информации в присутствии человека. Приведены описание концепции микроконтроллерного устройства, архитектура системы. Составлено техническое задание на изготовление устройства и его программного обеспечения. Изготовлен прототип устройства воспроизведения звуковой информации на базе Arduino-UNO. С целью уменьшения стоимости одного изделия была проведена модернизация устройства и в качестве управляющего микроконтроллера был выбран микроконтроллер Attiny13A-SU. Разработаны электрическая принципиальная схема, печатная плата устройства и программное обеспечение к нему. Изготовлено 17 действующих устройств воспроизведения звуковой информации. Предложено техническое решение дальнейшего усовершенствования микроконтроллерного устройства.
Ключевые слова: музыкальная скамья, микроконтроллерное устройство, печатная плата, Arduino-UNO, Attiny13A-SU, звуковая информация.

Карстина С.Г., Маркова М.П., Молданазарова У.

Құрылымы біртекті емес беттерде модельденген бөлшектердің гетероаннигиляциясы кезіндегі фракталдық, статистикалық және кинетикалық параметрлердің өзгерісіне талдау.

Құрылымы біртекті емес жазық беттердегі бөлшектердің өзара әсерлерін қарастырғанда, жазық беттің морфологиясы, әсерлесетін бөлшектердің таралуы және олардың процесс кезіндегі қозғалысы әртүрлі моделдік әдістерде кеңінен қолданылады. Бұл жұмыста құрылымы біртекті емес жазық бетте хаосты және мультифракталды таралған бөлшектердің гетероаннигиляция процесі кезіндегі өзгеретін кинетикалық, статистикалық және фракталды параметрлерінің салыстыру нәтижелері келтірілген. Гетероаннигиляция процесі кезіндегі бөлшектердің беттік қозғалысы мен әртүрлі өзараәсерлесу ықтималдықтарын өзгергендегі олардың уақыт және кеңістік бойынша өзгеретін қасиеттерін имитациялау үшін IV класты ықтималдық ұялы автомат әдісі қолданылды. Осылайшы модельдеу нәтижесінде гетероаннигиляция процесінің әртүрлі итерациясы кезінде әсерлесетін бөлшектердің әсерлесу ықтималдығы, бастапқы таралуы және қозғалу еркіндігі кинетикалық режимдердің құрылуына әсер ететіндегі көрсетілді. Әсерлесетін бөлшектердің қозғалу еркіндігін төмендету арқылы жүйеде кеңістіктік біртектіліктің болмауын ұзағырақ уақытқа сақтауға болатыны көрсетілді. Әсерлесетін бөлшектердің қозғалу еркіндігі мен әсерлесу ықтималдығын арттыру арқылы фракталды өлшемнің өзгеру жылдамдығын және гетероаннигиляция кинетикасының жылдамдық коэффициентін жоғарылатуға болатыны көрсетілді. Гетероаннигиляция кезінде фракталды өлшемді төмендету арқылы өзара әсерлесетін бөлшектердің таралу симметриясының деңгейі мен формасының сипаттамасы болып табылатын асимметрияны азайтуға және эксцессаны арттыруға болаттындығы байқалды. Дегенмен, асимметрия мен эксцессаның үлкен мәндері өзара әсерлесетін бөлшектердің қалыпты беттік таралуынан ауытқитынын көрсетеді.
Түйінді сөздер: гетероаннигиляция, фракталды кинетика, фракталды өлшемділік, құрылымы біртекті емес бет, мультифракталдық талдау, өаза әрекеттесу ықтималдығы.

Карстина С.Г., Маркова М.П., Молданазарова У.

Анализ изменения фрактальных, статистических и кинетических параметров при гетероаннигиляции частиц на смоделированной структурно-неоднородной поверхности

При изучении механизмов взаимодействия частиц на структурно-неоднородных поверхностях, влияния морфологии поверхности, распределения взаимодействующих частиц и их подвижности на механизмы протекающих процессов широко применяются различные модельные подходы. В работе представлены результаты сравнения и сопоставления кинетических, статистических и фрактальных параметров, изменяющихся в процессе гетероаннигиляции частиц, распределенных хаотически и мультифрактально на смоделированной структурно-неоднородной поверхности. Для имитации сложного поведения частиц во времени и в пространстве в процессе гетероаннигиляции при изменении их подвижности по поверхности и различных вероятностях взаимодействия, применялся метод вероятностного клеточного автомата IV класса. На основании результатов моделирования показано, что вероятность взаимодействия, начальное распределение и подвижность взаимодействующих частиц оказывают влияние на формирование кинетических режимов на разных итерациях процесса гетероаннигиляции. Установлено, что понижение подвижности взаимодействующих частиц приводит к более длительному сохранению в системе пространственной неоднородности. Увеличение подвижности взаимодействующих частиц и вероятности их взаимодействия увеличивает скорость изменения фрактальной размерности и скоростные коэффициенты кинетики гетероаннигиляции. Уменьшение фрактальной размерности при гетероаннигиляции сопровождается уменьшением асимметрии и увеличением эксцесса, характеризующими форму и степень симметричности распределения взаимодействующих частиц. При этом, большие значения асимметрии и эксцесса указывают на значительное отклонение от нормального распределения взаимодействующих частиц по поверхности.

Ключевые слова: гетероаннигиляция, фрактальная кинетика, фрактальная размерность, структурно-неоднородная поверхность, мультифрактальный анализ, вероятность взаимодействия.

INFORMATION ABOUT AUTHORS | **АВТОРЛАР ТУРАЛЫ МӘЛІМЕТТЕР** | **СВЕДЕНИЯ ОБ АВТОРАХ**

Abdigapar, A.A. – 2 years Master's student, L.N. Gumilyov Eurasian National University, Astana, Kazakhstan, abdigaparalen@gmail.com

Abouellail, A.A. – Candidate of techn. sciences, Lecturer, Sphinx University, New Asyut, Egypt; Scopus Author ID:56825975400; ORCID iD: 0000-0002-9357-6214; ahmed.abouellail@sphinx.edu.eg

Abykenov, A.T. – Student, Physical and Technical Faculty, E.A Buketov Karaganda University, Karaganda, Kazakhstan, abykenovazamat@gmail.com

Afanasyev, D.A. - PhD, Professor of the Department of Radiophysics and Electronics, Physical and Technical Faculty, E.A Buketov Karaganda University, Karaganda, Kazakhstan, ORCID ID: 0000-0002-0437-5315, Scopus ID: 41661115200, WoS Researcher ID: D-4196-2012, a.d.afanasyev2@gmail.com

Alpyssova, G.K. - PhD, Associate Professor, Department of Radiophysics and Electronics, Academician E.A.Buketov Karaganda University, Karaganda, Kazakhstan; Scopus Author ID: 57204979025; ORCID iD: 0000-0002-7164-2188; gulnur-0909@mail.ru

Baiserikov, B.M. – Master (Eng), Researcher, JSC «National Center of Space Research and Technology», Almaty, Kazakhstan; Satbayev University, Almaty, Kazakhstan; SCOPUS Author ID: 58040708000; ORCID iD: 0000-0003-0804-3147; baiserik.b.91@mail.ru

Baratova, A.A. – Candidate of phys.-math. sciences, PhD, Associate Professor, L.N. Gumilyov Eurasian National University, Astana, Kazakhstan, Scopus Author ID: 55221822500, aa.baratova@yandex.kz

Berdibekov, A.T. - colonel, PhD, Associate Professor, Research Institute of Arms and Military Equipment of the Military Research Center, the National Defense University named after the First President of the Republic of Kazakhstan – Elbasy, Astana, Kazakhstan.

Berezovskaya I.E. - PhD, Senior Lecturer, Department of Thermophysics and Technical Physics, Faculty of Physics and Technology, al-Farabi Kazakh National University, Almaty, Kazakhstan; Scopus Author ID: 56943245500; Yryna.Berezovskaya@kaznu.kz

Chang, J. – Candidate of techn. sciences, Post doctoral student, Institute for Advanced Study of Shenzhen University, Shenzhen, China; Scopus Author ID: 57220076559; jiangleichang@foxmail.com

Daliev, Sh.Kh. – Doctor of phys.-math. sciences, Professor, Leading Researcher of laboratory Semiconductor Physics, Institute of Semiconductor Physics and Microelectronics, National University of Uzbekistan named after Mirzo Ulugbek, Tashkent, Uzbekistan; Scopus Author ID: 12646710600; ORCID iD: 0000-0001-7853-2777.

Dolya, A.V. – Master (Sci.), Research Institute of Arms and Military Equipment of the Military Research Center, the National Defense University named after the First President of the Republic of Kazakhstan – Elbasy, Astana, Kazakhstan.

Doroshkevich, A.S. – PhD**,** Head of group EG-5, Joint Institute for Nuclear Research, Dubna, Russia; Scopus Author ID:12545381500; ORCID iD: 0000-0003-4290-1520.

Genov, I.G. – PhD, Senior researcher of laboratory of Neutron physics, Joint Institute for Nuclear Research, Dubna, Russia; Senior researcher, Institute of Electrochemistry and Energy Systems "Acad. Evgeni Budevski", Bulgarian Academy of Sciences, Sofia, Bulgaria; Scopus Author ID: 55658961400.

Gruzin, V.V. – Doctor of techn. sciences, Professor, Research Institute of Arms and Military Equipment of the Military Research Center, the National Defense University named after the First President of the Republic of Kazakhstan – Elbasy, Astana, Kazakhstan; Scopus Author ID: 57191036631; ORCID iD:0000-0002-1128-5246

Ismailov, M.B. –Doctor of techn. sciences, Professor, Director, Department of Jet Propulsion and Materials Science, JSC «National Center of Space Research and Technology», Almaty, Kazakhstan; Scopus Author ID: 57194178956; ORCID iD: 0000-0002-1111-4658; m.ismailov@spaceres.kz

Karabassov, V.A. – Head, digital officer of the Center Information Technology and Telecommunications, E.A Buketov Karaganda University, Karaganda, Kazakhstan, wladdawid2@gmail.com

Karstina, S.G. - Doctor of phys.-math. sciences, Professor, Physics and Nanotechnology Department, E.A. Buketov Karaganda University, Karaganda, Kazakhstan; Scopus Author ID:6506303497; WoS Researcher ID: AAW-5227-2021, ORCID iD: 0000-0001-8425-681X; skarstina@mail.ru

Kenzhaliyev, B.K. – Doctor of techn. sciences, Professor, General Director – Chairman of the Board, Satbayev University, JSC «Institute of Metallurgy and Ore Beneification», Almaty, Kazakhstan; Scopus Author ID: 6603486541; ORCID iD: 0000-0003-1474-8354; bagdaulet_k@mail.ru

Kenzhegulov, A.K. - PhD, Researcher, JSC «National Center of Space Research and Technology», Almaty, Kazakhstan; Satbayev University, JSC «Institute of Metallurgy and Ore Beneification», Almaty, Kazakhstan; Scopus Author ID: 57210622996; ORCID iD: 0000-0001-7001-2654; a.kenzhegulov@satbayev.university

Khalenov, O.S. – Researcher, E.A. Buketov Karaganda University, Karaganda, Kazakhstan; otangaliy@gmail.com

Kirillov, A. – PhD**,** Senior Researcher, Joint Institute for Nuclear Research, Dubna, Russia; Scopus Author ID: 55116623400; ORCID iD: 0000-0002-8727-2441

Kostina, M.A. – Candidate of technical Sciences, Associate Professor, National Research Tomsk Polytechnical University; Tomsk State University of Control Systems and Radioelectronics, Tomsk, Russia; Scopus Author ID: 57117553400; ORCID ID: 0000-0003-2626-6002; mariyakostina91@mail.ru

Kruchinin, N.Yu. – Candidate of phys.-math. sciences, Associate Professor, Department of Radiophysics and Electronics, Orenburg State University, Orenburg, Russian Federation; Scopus Author ID: 35170029600; ORCID iD: 0000-0002-7960-3482; kruchinin_56@mail.ru

Kucherenko, M.G. – Doctor of phys.-math. sciences, Professor, Director of the Center for Laser and Informational Biophysics, Orenburg State University, Orenburg, Russian; Scopus Author ID: 7003581468; WoS Researcher ID: E-9515-2015; ORCID iD: 0000-0001-8821 -2427; clibph@yandex.ru

Laurinas, V.Ch. – Candidate of phys.-math. sciences, Associate Professor, E.A. Buketov Karaganda University, Karaganda, Kazakhstan, Scopus Author ID:6504426206; ORCID iD:0000-0001-7079-254X; vitas-laurinas@rambler.ru

Markova, M.P. – Master of Science in Physics, Senior Lecture, Automated Information Processing and Control Systems Department, Omsk State Technical University, Omsk, Russia, ORCID iD: 0000-0001-7380-1499; markovamp@mail.ru

Moldanazarova, U. – PhD, Postdoctoral student, Physics and Nanotechnology Department, E.A. Buketov Karaganda University, Karaganda, Kazakhstan; Honorary Research Fellow, University of Liverpool, Liverpool, United Kingdom; WoS Researcher ID: AGZ-6409-2022; ORCID iD: 0009-0009-3883-9198; psumolda@liverpool.ac.uk

Ospanova, Sh.S. - PhD, Senior Lecturer, Department of Thermophysics and Technical Physics, Faculty of Physics and Technology, al-Farabi Kazakh National University, Almaty, Kazakhstan; Scopus Author ID:55988678700; shynarospanova1987@gmail.com

Rakhmanov, D.A. – PhD**,** Head of department of international relations, Institute of Semiconductor Physics and Microelectronics, National University of Uzbekistan named after Mirzo Ulugbek, Tashkent, Uzbekistan; Scopus Author ID: 57292855500; ORCID iD: 0000-0003-1275-5999;

Ryspaeva M.Zh. - PhD, Senior Lecturer, Department of Thermophysics and Technical Physics, Faculty of Physics and Technology, al-Farabi Kazakh National University, Almaty, Kazakhstan; Scopus Author ID: 22036127100; Maiya.Ryspayeva@kaznu.kz

Sakipov, K.E. – Candidate of techn. sciences, Associate Professor, L.N. Gumilyov Eurasian National University, Astana, Kazakhstan, Scopus Author ID: 57197722422, ksakipov@mail.ru

Satayeva, G.E. – Candidate of chem. sciences, Associate Professor, L.N. Gumilyov Eurasian National University, Astana, Kazakhstan, Scopus Author ID: 56183224500, lady.sataeva2012@yandex.kz

Seldygaev, O.B. – Candidate of chem. sciences, Junior Researcher at the Laboratory of Applied Mechanics and Robotics, Physical and Technical Faculty, E.A Buketov Karaganda University, Karaganda, Kazakhstan

Sharifov, Dz.M. – Candidate of phys.-math. sciences, L.N. Gumilyov Eurasian National University, Astana, Kazakhstan, Scopus Author ID: 6504653943, shjumm@mail.ru

Sheinmaier, E.V. – student, Physical and Technical Faculty, E.A Buketov Karaganda University, Karaganda, Kazakhstan, sheinmaier.edward.03@gmail.com

Soldatov, A.A. – Candidate of technical Sciences, Associate Professor, National Research Tomsk Polytechnical University; Tomsk State University of Control Systems and Radioelectronics, Tomsk, Russia; Scopus Author ID: 55308977400; ORCID iD: 0000-0003-0696-716X; soldatov.88@bk.ru

Soldatov, A.I. – Doctor of techn. sciences, Professor, National Research Tomsk Polytechnical University, Tomsk, Russia; Tomsk State University of Control Systems and Radioelectronics, Tomsk, Russia; Scopus Author ID: 24725397500, ORCID iD: 0000-0003-1892-1644; asoldatof@mail.ru

Tasmukhanova, A.A.– Master (Sci.), Physics Teacher, Faculty of Physics and Technology, al-Farabi Kazakh National University, Almaty, Kazakhstan; akhmetovaa2108@mail.ru

Tuan, P.L. – Master**,** Researcher, Laboratory of Neutron physics, Joint Institute for Nuclear Research, Dubna, Russia; Researcher, Hanoi Irradiation Center, Vietnam Atomic Energy Institute, Hanoi, Vietnam; Scopus Author ID: 57215496179

Tussupbekova, A.K. - PhD, Associate Professor of the Department of Radiophysics and Electronics, Physical and Technical Faculty, E.A Buketov Karaganda University, Karaganda, Kazakhstan, ORCID ID: 0000-0001-5299-9977, Scopus ID: 56242322500, WoS Researcher ID: U-7552-2018, tussupbekova.ak@gmail.com

Utamuradova, Sh.B. – Doctor of phys.-math. sciences, Professor, Director of Institute of Semiconductor Physics and Microelectronics, National University of Uzbekistan named after Mirzo Ulugbek, Tashkent, Uzbekistan; Scopus Author ID: 6506286512; ORCID iD: 0000-0002-1718-1122.

Vasiliev, I.M. – Candidate of technical Sciences, Engineer, Scientific and Production center LLC "LEMZ-T", Tomsk, Russia; Scopus Author ID: 57217205078; vasiliev_ivan91@mail.ru

Yermakhanova, A.M. – PhD, Acting Deputy Chairman of the Board, JSC «National Center of Space Research and Technology», Almaty, Kazakhstan; Scopus Author ID: 57203409618; ORCID iD: 0000-0002-2145-5122; a.yermakhanova@mail.ru

Zinoviev, L.A. – Candidate of chem. sciences, Associate professor, E.A. Buketov Karaganda University, Karaganda, Kazakhstan; lzinovyev@yandex.ru

GUIDELINES FOR AUTHORS

Eurasian Physical Technical Journal (Eurasian phys. tech. j.) is a peer-reviewed Open Access international scientific journal quarterly publishing original research results on actual problems of technical physics. Since 2019, Eurasian phys. tech. j. has been indexed in the Scopus database on 4 scientific areas: www.scopus.com/sourceid/21100920795. According to the analytical OJS platform, in 2022 the Eurasian phys. tech. j. was included in **Q3** in all 4 scientific areas.

Acceptance of the manuscript for publication in the Eurasian phys. tech. j. is carried out online through website - https://phtj.buketov.edu.kz/index.php/EPTJ. Authors should check that their submissions meet all of the following requirements, as submissions may be returned to authors that do not comply with these guidelines.

Scientific article topic and content

A scientific article should contain the results of original scientific research previously unpublished and not intended for publication in other publications.

Manuscript of the article should contain at least 75% of the original text.

Articles should be written in English. The articles topic should correspond to the following scientific fields of **Physics: Energy, Engineering, Materials Science, Physics and Astronomy.**

Publication Ethics and Malpractice Statement

Submission of an article to the Eurasian phys. tech. j. implies that the paper described has not been published previously, that it is not under consideration for publication elsewhere, that its publication is approved by all authors and tacitly or explicitly by the responsible authorities where the paper was carried out, and that, if accepted, it will not be published elsewhere in the same form, in English or in any other language, including electronically without the written consent of the copyright holder. In particular, translations into English of papers already published in another language are not accepted.

For information on Ethics in publishing and Ethical guidelines for journal publication see http://www.elsevier.com/publishingethics and http://www.elsevier.com/journal-authors/ethics.

The Eurasian phys.tech.j. strictly adheres the Code of Conduct of the Committee on Publication Ethics (COPE), and follows the COPE Flowcharts for Resolving Cases of Suspected Misconduct (http://publicationethics.org/files /u2/New_Code.pdf).

To verify originality, your article may be checked by the originality detection service Cross Check http://www.elsevier.com/editors/plagdetect.

Pre-publication process

Authors are responsible for the content of their publications. No other forms of scientific misconduct are allowed, such as plagiarism, falsification, fraudu-lent data, incorrect interpretation of other works, incorrect citations, etc. Authors are obliged to participate in peer review process and be ready to provide corrections, clarifications, retractions and apologies when needed. All authors of a paper should have significantly contributed to the research.

Reviewers should provide objective judgments and should point out relevant published works which are not yet cited. Reviewed articles should be treated confidentially. The reviewers will be chosen in such a way that there is no conflict of interests with respect to the research, the authors and/or the research funders.

Editors have complete responsibility and authority to reject or accept a paper, and they will only accept a paper when reasonably certain. They will preserve anonymity of reviewers and promote publication of corrections, clarifications, retractions and apologies when needed.

The acceptance of a paper automatically implies the copyright transfer to the Eurasian phys. tech. j.

All submitted papers will the sent for reviewing to leading experts in the given area.

The Editorial Board of the Eurasian phys. tech. j. will monitor and safeguard publishing ethics.

The editors reserve the right to accept or reject manuscripts.

The article and all documentation must be identified by the name of the 1st author: Akhmetov AA_et al_paper; Akhmetov AA_et al_fig.1; Akhmetov AA_et al_Cover letter; …

The article text must be formatted according to the **Template**, font - Times New Roman, size -11 pt; line spacing-single; alignment-in width, see https://phtj.buketov.edu.kz/index.php/EPTJ/about/submissions#authorGuidelines

An article should consist:

Title: includes a separate line on the left the **UDC** index, Title of the article, information about the authors- surname and initials, name of institution, city, country, e-mail of a corresponding author. The

author***** who submitted an article for publication will be considered as a corresponding author.

Abstract should consist of at least 5-6 sentences, not exceeding 200-250 words without formula, references, abbreviations. An abstract is a short and powerful summary that describes the focus and subject of a research paper. It could contain the information about why the research study was done, background, what the methodology was and something about the findings of the author(s).

Keywords: at least 3-10 basic terms or short phrases used in the article.

The text should be divided on structural parts: Introduction, Main part (Theoretical part, Methods and materials or Experimental technique), Results and Discussion, Conclusions.

Conclusions: formulating main results; a comparison of the results with the existing data on this topic; assessment of scientific novelty and practical value of the results.

Acknowledgments or Funding may be shown at the end of the article text, before References.

References: a bibliographic list is compiled according to the requirements: - Books, abstracts, patents: Surname and initials of the authors (it is enough to indicate the first three or one surnames, et al), ***Title of the book*** in italics, publish house or city, year and total number of pages. - Journals, collections of papers, conference proceedings - Surname and initials of the authors (the first three are enough), the title of the article, the ***Title of the journal*** in italics (you can use the abbreviated title), city and / or country, year, volume, issue number, pages of the "begining and end" (pp. … - … .). - Internet links also must to indicated the authors, the title and URL

The authors should represent References according to the requirements of international journals on physics, but should to consult preliminarily for standard abbrevi¬ations of journal's names. More information on references guidelines for journal publication you can see in Harvard reference system - http://www.emeraldgrouppublishing.com /authors/guides/write/harvard.htm?part=2/

All references must be numbered in the text (for example, [1], [2-4]) and listed in numerical order.

All abbreviations and acronyms, with the exception of obviously well-known, should be deciphered at first use in the text.

Equations in your paper have to be written using the Microsoft Equation Editor or the MathType.

Tables, numbered and titled, should be inserted into the text (Times New Roman, size - 10 pt) or have been presented as an appendix at the end of the article.

Figures should be prepared in a digital form suitable for direct reproduction. Figures shall be submitted on the separate sheets or can be included into the text.

The manuscript volume, including text, formulas, figures, bibliography, should not exceed 12 pages including tables, figures (no more than 8-10) and references (no more than 30-35) of text typed on a computer using Microsoft Word editor. The review article should not exceed 20 pages with no more than 15 figures.

List of required documents

The following files must be uploaded to the journal's website:

1. Text of the article, with pictures (*.doc);
2. Figure, Picture, Photo (fig1.jpg, fig2.pcx, …);
3. Figure captions (*.doc);
4. A Cover letter - from a university, research institute or an organization licensed to conduct research activities, must be issued on an official letterhead and / or certified by the organization seal. The management officially confirms by this letter that the article (the title of the article and the names of the authors are indicated in English) doesn't contain any information constituting state or commercial secrets, and the article can be published in the Open Press. Authors must upload a copy of the signed Cover Letter in PdF format to the Journal website.

It's necessary to upload by separately 2 files in English, and in Russian for authors from Russia, and in Kazakh for authors from Kazakhstan:

5. Article's data: Surname and initials of the authors, the article title, abstract, keywords.
6. Information about each co-author: full name, academic degree, academic title, place of work or study, title of organization, city, country, SCOPUS Author ID or ORCID iD; and contact details (e-mail, phone).
7. Receipt of payment. Authors should pay for the publication only after receiving notification about a positive decision of the reviewers.